# Master's Thesis

**Design of Mechanical Systems**

# Strength based optimization and test of fiber reinforced additively manufactured structures considering topology and fiber orientation

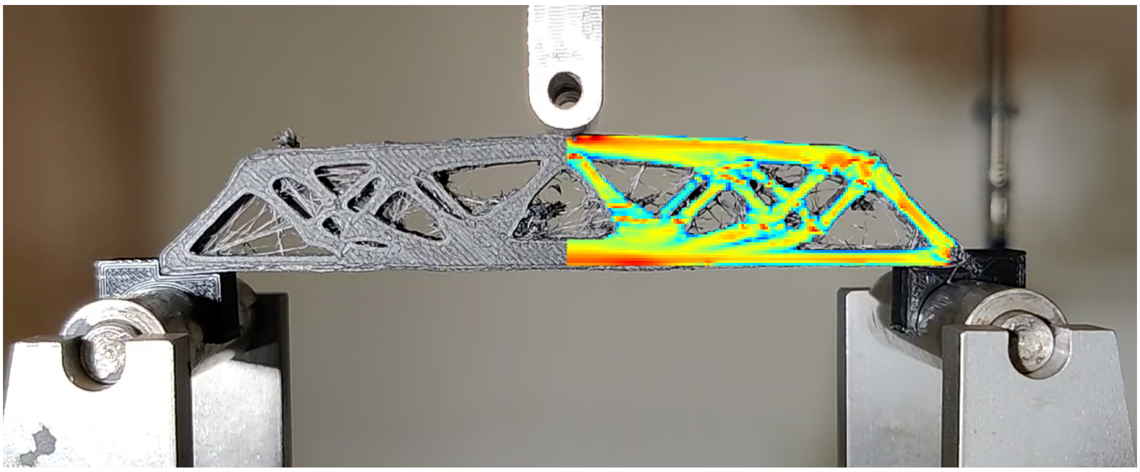

**DMS4 23B**

Frederik Juel Gadegaard
Jan Thuesen

AALBORG UNIVERSITET
STUDENTERRAPPORT

**Faculty of**
**Engineering and Science**
Materials and Production
Fibigerstræde 14
9220 Aalborg Øst
http://www.aau.dk

**Title:**

Strength based optimization and test of fiber reinforced additively manufactured structures considering topology and fiber orientation

**Project theme:**

Additive manufacturing and optimization

**Project extend:**

30 ECTS

**Project Period:**

1. February 2022 - 2. juni 2022

**Project Group:**

DMS4 23B

**Participants:**

Frederik Juel Gadegaard
Jan Thuesen

**Supervisors:**

Erik Lund
Sebastian Malte Hermansen

**Pages: 81**
**Appendix: 5**
**Date of Completion: 2/6-2022**

**Abstract:**

This masters thesis is about fiber reinforced FFF 3D-printing and how simultaneous topology and fiber angle optimization can be used to create structural parts with this material. Density based topology optimization is used together with the discrete material optimization. Since the original formulation penalizes intermediate densities excessively hard it is not possible to use it together with density filtering. Therefore two new formulations have been proposed and implemented to circumvent this problem. The first formulation reduces the penalization while the second method removes the filtering.
The problem that is solved is a minimization of the volume of 3D-printed structures, subjected to a strength constraint. The optimization is based on material parameters found from experimental tests of fiber reinforced 3D-printed material. Both continuous and short fiber reinforced materials are investigated. The optimization is validated against experimental tests. Both methods can therefore be viable but the method with the reduced penalization is recommended due to the introduction of a minimum length scale from the filter.

# Resume

Denne kandidatafhandling omhandler fiber forstærket FFF 3D-print og hvordan det kan kombineres med topologi- og fiberretningsoptimering, til at designe strukturelle dele.
To fiber forstærkede 3D-print materialer er testet for at bestemme materialeegenskaberne. Disse to materialer er en kortfiberforstærket Polyamid og en Polyamid der er forstærket med kontinuerte fibre. Disse materialeegenskaber bliver benyttet i optimeringen og gør det muligt at validerer optimeringsresultaterne med eksperimentelle test. Materialemodellen der benyttes, vil blive antaget værende lineær elastisk.
Til optimeringen anvendes finite element metoden til at bestemme svigtindeks. Det benyttede svigtindeks er Tsai-Wu, hvilket tilføjes som en bibetingelse til optimeringen, hvis formål er at minimere volumen. Topologioptimeringen tager udgangspunkt i den densitetsbaserede metode mens der til fiberretningsoptimeringen anvendes Discret Material Optimization (DMO). Udvælgelsen af DMO'en skyldes primært muligheden for at kunne fremstille de optimerede emner med minimal postprocessering af resultaterne. Implementeringen af DMO-metoden er uddybet og analytiske udtryk for sensitiviteterne er bestemt til implementeringen i den densitets baserede topologioptimering. Det er fundet ud af at den oprindelige formulering af DMO'en til optimering på baggrund af svigtindeks ikke kan anvendes i sammenhæng med densitetsbaseret topologioptimering når densitetsbaseret filtrering anvendes. Derfor er to løsningsforslag udarbejdet og testet. Første løsningsforslag er ikke at summere fejlkriterierne i de enkelte elementer, hvorved penaliseringen mindskes. Det andet løsningsforslag er at fjerne filtreringen. Dette resulterer dog i problemer med checkerboarding, hvorfor det er nødvendigt at introducere en kvadratisk elementformulering, der ikke kræver filtrering for at give fysiske resultater.
Disse løsningsforslag er testet i forskellige numeriske eksempler for at vurdere dem mod hinanden. Denne vurdering viser at den lineære elementformulering uden summering af svigtindeks, er mere favorabel end den kvadratiske, grundet den længdeskala der introduceres med filtreringen. De numeriske resultater er desuden valideret med eksperimentelle test for det kortfiberforstærkede materiale. Dette viser en underestimering af den strukturelle styrke, hvilket er forventeligt da der tilføjes materiale til den optimerede geometri under postprocesseringen, der tillader at emnerne kan 3D-printes. Optimeringen vurderes derfor at være tilnærmelsesvis sammenlignelig med de eksperimentelle resultater. Der er derfor opstillet to metoder til at kombinere topologi optimering med fiberretnings optimering af FFF 3D-printede geometrier. Begge metoder kan bruges, men metoden med filtre uden summering af svigtindeks er dog at foretrække grundet den tilføjede længdeskala.

# Preface

This master's thesis is submitted by two engineering students at Aalborg University as a part of their master's degree in, Design of Mechanical Systems. The work has been done over period of 4 months from February to June 2022. The work is carried out at the Department of Materials and Production at Aalborg University.

## Reading guide lines

The project is written using American English spelling and the Harvard method is used throughout the project as source referencing. The report will be divided in chapters numbered (x.y.z), where the first number marks the chapter, the second mark the section and third number mark the subsection.

Throughout the project vectors will be marked with curly brackets $\{x\}$ and matrices will be marked with square brackets $[x]$.

In order to define the stresses the Voigt notation is used.

The numerator layout is used in order to determine the gradients.

A nomenclature list can be found in the start of the project, which will give an overview of the notation.

At the end of the report a complete bibliography can be found together with the applied appendixes denoted A, B, C, D and E.

## Acknowledgements

We wish to acknowledge the funding provided by the Siemens Foundation and The Department of Materials and Production at Aalborg University, that made it possible to procure a continuous fiber 3D-printer for the university.

# Nomenclature

**Vector**

$\{\lambda\}$ Lagrange multipliers

$\{\sigma_e\}$ Stress components of element e

$\{F\}$ Global force vector

$\{U\}$ Global displacement vector

$\{u_e\}$ Nodal displacements for element e

$\{y\}$ Merit function vector

**Matrix**

$[\partial]$ Partial operator matrix

$[B]$ Strain-displacement matrix

$[C]$ Constitutive matrix

$[H]$ Linear weight matrix

$[K]$ Global stiffness matrix

$[k_e]$ Elemental stiffness matrix

$[N]$ Shape function

$[T]$ Transformation matrix

**Scalar**

$\bar{\bar{x}}_e$ Projected element densities

$\bar{x}_e$ Filtered element densities

$\beta$ Smoothing parameter for projection filters

$\Delta$ Move limits

$\eta$ Threshold value for threshold filter

$C$ Compliance

$c$ Adaptive constraint scaling factor

$d_{ext}$ Size of domain extension

$E$ Young's modulus

$FI_e$ Failure index in element

$FI_{PN}$ P-norm of failure indices

$FI_{rel,e}$ Relaxed failure index in element

$G$ Shear modulus

$J$ Determinant of Jacobian

$l_e$ Element length

$M_{cnd}$ Measure of candidate non-discreteness

$M_{dnd}$ Measure of density non-discreteness

$n_{elem}$ Number of elements

$n_{mat}$ Number of materials

$P$ P-norm aggregation factor

$p$ Stiffness penalization factor

$q$ Failure index relaxation factor

$R$ Filter radius

$S$ Shear strength

$s$ Tsai-Wu strength ratio

$t$ Thickness

$V$ Volume

$v$ Poisson's ratio

$w_G$ Weight of Gauss points

$w_k$ Stiffness weight function

$w_{FI}$ Failure index weight function

$X$ Strength in fiber direction

$x_e$ Element densities

$Y$ Strength perpendicular to fiber direction

# Table of contents

# 1 Introduction

Additive Manufacturing (AM) also known as 3D-printing has become widely used in many different applications. It has become a technology that many companies are currently implementing in their workflow for prototyping, but also for manufacturing of production equipment and end use products.
In Additive manufacturing material is added selectively in order to create a 3D structure. This is the opposite of traditional manufacturing like machining, where material is removed in order to create the part. The main benefit of additive manufacturing is the large design freedom and that it does not create a lot of excess material. The large design freedom is a result of the additive manufacturing process, being able to place the material where it is needed. This is also why there is not a lot of excess material used.
Additive manufacturing is normally used in cases of manufacturing low quantities, because the manufacturing time per part is typically higher than for traditional manufacturing. Depending on the additive manufacturing method used the manufacturing time can vary a lot.

The additive manufacturing method Stereolithography (SLA) is a very fast method for creating 3D structures. The SLA method uses light to cure a polymer resin layer by layer in order to create a 3D structure (Formlabs 2022). The light source could be a laser or a screen that cures the resin. The light source typically has a high resolution which results in good surface quality.
The SLA method does not result in strong mechanical properties, because it is limited by the materials that can be used in the process. SLA additive manufacturing is therefore useful for creating prototypes and for other use cases, where the part does not have to withstand high structural loading but surface quality is important.
The high surface quality and complex geometry that can be achieved by SLA can be used for 3D-printing injection molding forms. Hereby it is possible to injection mold complex geometries that would otherwise not be possible. A SLA printed mold and the molded part, can be seen in Figure 1.1. The SLA mold can be removed by a special solvent that does not damage the injection molded part. This will result in a highly complex injection molded part, by using a SLA manufactured form, that benefits from the large design freedom of additive manufacturing. (Addifab 2022)

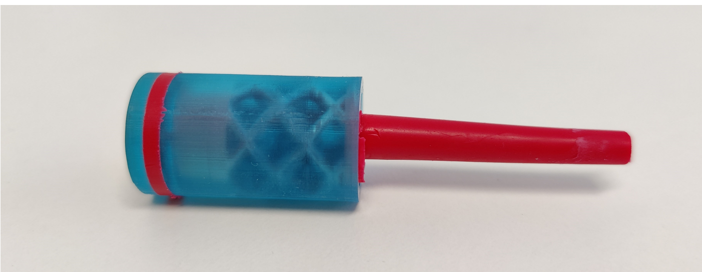

Figure 1.1: SLA manufactured mold (blue) and injection molded part (red).

The large design freedom of additive manufacturing can also be used for creating structural parts, that are not possible with SLA. Powder bed fusion is a method, which can be used to create these structural parts based on powder, which is fused together during the manufacturing process. The most popular method within powder bed fusion is Selective Laser Sintering (SLS), which uses a laser processing system to sinter thin layers of powder together. This results in almost isotropic material properties (Varotsis 2022).
The SLS method is also a relatively fast additive manufacturing method similar to the SLA method. The surface quality of the SLS manufactured parts is also high, but without processing it will have a grainy/powdered look, that the SLA manufactured parts do not have (Varotsis 2022).
Where the SLS has its benefits is in the selection of materials. It can use both polymer and metal powders, which opens up the method for different use cases. One of the downsides of the the SLS manufacturing method, is the amount of post processing it takes to clean the parts from excess powder. All this excess powder can though be reused with minimal processing. Furthermore the high initial cost of the SLS machines makes it a technology that mainly larger companies invest in.
Due to the large design freedom and the good material properties it is possible to combine multiple load bearing parts into a single piece. This has been utilized by General Electric to create a single piece SLS metal 3D-printed fuel nozzle for an aircraft engine, that otherwise had to be made from about 20 different components. In this process they were able to lower the weight of the fuel nozzle by 25% as well. (GE Aviation 2018)
Due to the high cost of the SLS 3D-printers this is not a method that is readily available for smaller companies, especially the SLS 3D-printers that can manufacture parts in metal are very costly.

Another additive manufacturing method that is very widely used is the Fused Filament Fabrication (FFF). This additive manufacturing method includes 3D-printers ranging from low cost hobby printers to large production printer for industrial use. The entry cost of this method can thus be lower and it is therefore a method that is more accessible.
This method uses a filament strand that is extruded through a nozzle to create the 3D structure. The surface quality of this manufacturing method will be highly dependent on the machine and manufacturing settings used. Because the 3D part is build from layers of thin print paths, this will be seen in the surface quality as shown in Figure 1.2. It is therefore difficult to reach the same surface quality as SLA and SLS manufacturing. It is furthermore seen that voids can be created between the print paths. Large voids should be avoided in order to obtain good mechanical properties.

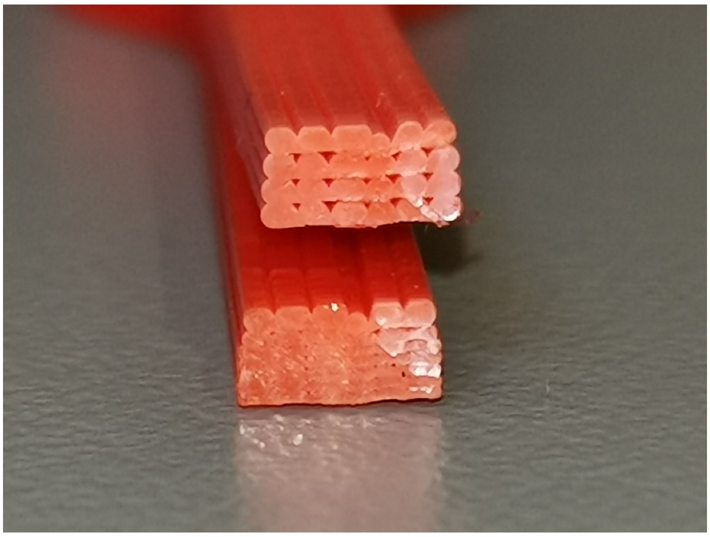

Figure 1.2: Surface finish of FFF 3D-print including voids. Picture from Steffensen et al. (2019).

The FFF method is slower than the SLA and SLS methods, because it has to move a larger mass while printing. This limits the speed and acceleration during the manufacturing process. The laser processing system that can be used in SLA and SLS is much faster, because it does not need to move a large mass. The FFF method will in general create parts, that are less isotropic than the parts produced by the other methods. This is because the mechanical properties depend on the direction of the print paths. The FFF printed material will be stronger in the direction of the print paths. (Bellini and Güçeri 2003)
This effect becomes especially evident when utilizing fiber reinforced filaments. Fiber reinforced FFF 3D-printing can be divided into two different classes, which are short fiber reinforced and continuous fiber reinforced printing. The short fiber reinforced filaments can be used on standard FFF 3D-printers, in order to increase the strength and stiffness along the print paths. For the continuous fiber reinforced materials specialized 3D-printers are needed, but the strength and stiffness can be improved with around an order of magnitude.
The technology of continuous fiber 3D-printing is more expensive than the hobby grade FFF 3D-printers, but different models are available. For example the Anisoprint continuous fiber 3D-printers exist in three sizes ranging from 113.000 DKK to 1.800.000 DKK (3D-Experten 2022).
Continuous fiber FFF 3D-printed parts can for example be used for equipment with high structural requirements. An example is the lifting tool by Wärtsilä (Markforged 2022). By using continuous fiber 3D-printing they created a lifting tool that can carry 960 kg. They estimate a saving of around 1.000 EUR per tool they 3D-print and a mass reduction of 75% compared to the original steel tool.

The FFF additive manufacturing using continuous fiber therefore has a great potential in manufacturing of strong structural parts. The problem with this method is the placement of the fibers in the 3D-geometry. In order to fully utilize the benefits of continuous fiber FFF 3D-printing, the fiber paths must be placed according to the load scenario. The 3D-printing programs used today, do not take the load case of the part into account, but instead simply place the fibers around the contour as seen in Figure 1.3. This improves the bending strength and stiffness, but in some cases it can be beneficial to place the fibers differently. If this was implemented the use of FFF continuous fiber 3D-printing could become more common for strong, light and complex structural parts.

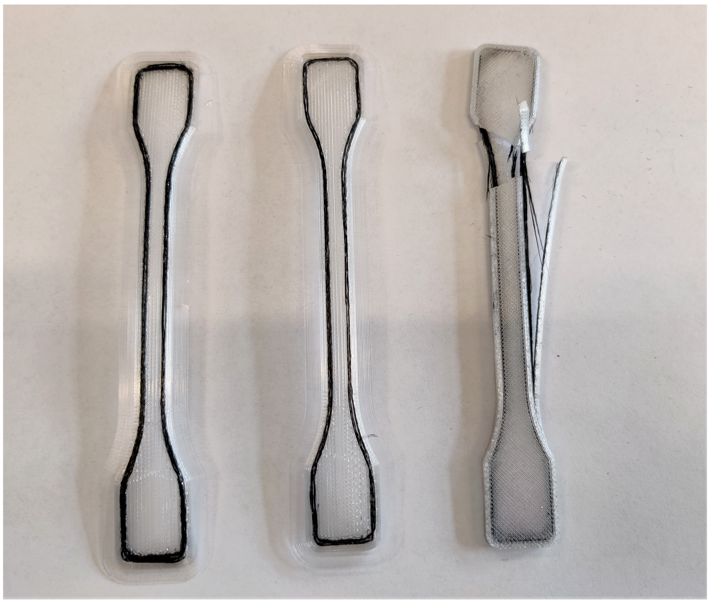

Figure 1.3: Carbon fiber (black) reinforced polymer (clear) using contour reinforcement.

A way to include the load case in the fiber placement, could be by using optimization. Structural optimization is widely used in a lot of different applications in order minimize weight, stresses or compliance of structural components. A widely used method for structural optimization is topology optimization, where material is removed from a design domain in order to strategically place holes in the structure.

Topology optimization was first introduced by Bendsøe and Kikuchi (1988), which introduced the large design space that defines topology optimization. This was expanded to density based topology optimization using a continuous variable by Bendsøe (1989), where the Solid Isotropic Material with Penalisation (SIMP) method is often used to penalize the stiffness. A common challenge for topology optimization is to reach a physical results and thus filter are typically applied in order to ensure a feasible solution. This could be the sensitivity filter as introduced by Sigmund (1994) or density filtering introduced by Bourdin (2001) and Bruns and Tortorelli (2001). Other filtering methods can be implemented in order to increase the discreteness of the optimization results.

In order to ensure that the optimized structure does not fail, strength based topology optimization has to be used. Strength based topology optimization results in a singularity problem. This was discovered by Sved and Ginos (1968) when solving truss optimization problems. In order to solve the problem Cheng and Guo (1997) introduced stress relaxation through the $\varepsilon$-approach which was further developed by Bruggi (2008).

When optimizing fiber reinforced 3D-printed parts the material properties are orthotropic. The optimization thus has to be able to determine both the best material distribution and fiber orientation. This has for example been done by Mirzendehdel, Rankouhi, and Suresh (2017) for maximization of the failure load using a single orientation variable.
The optimization problem has also been solved by Hoglund and Smith (2015) considering raster optimization of fiber reinforced FFF 3D-printed material, although only considering compliance optimization. The aim of this project will thus be to develop a method for simultaneous strength based topology and fiber orientation optimization of fiber reinforced FFF 3D-printed parts. This will include a material characterisation of the fiber reinforced material and an investigation of different methods for optimizing the fiber orientations.

# 2 Problem formulation

In order to fully utilize the additive manufacturing process with fiber reinforced materials, the combination with structural optimization is a vital part as discussed above. The problem formulation, which will frame this project is thus given as:

*"How do fiber reinforced FFF 3D-printed materials behave structurally and how can they be used to improve parts in combination with simultaneous strength constrained topology and fiber orientation optimization?"*

In order to fulfill this problem formulation the following points will be addressed throughout the project.

- Establish material data
- Perform optimization
- Validate optimization results

Material tests will be performed in order to establish material properties for FFF 3D-printed materials. Both short fiber and continuous fiber reinforced materials will be investigated. This is necessary in order to match the results from the optimization with the experimental validation.

The topology optimization will take offset in the density based method, while different methods for simultaneous fiber orientation optimization will be investigated. The optimization will be based on a minimization problem with the focus on minimizing the volume of FFF 3D-printed parts. The problem will include a strength constraint in order to ensure that the optimized parts can withstand the specified load. Only static stress based strength measures are considered and other factors such as fatigue and strain based failure criteria are not considered. Furthermore only plane stress problems will be considered.

The optimized part will be 3D-printed and tested in order to validate the performance.

# 3 Additive manufacturing

Throughout this chapter the fundamentals of FFF 3D-printing will be described, together with a more detailed description of fiber FFF 3D-printing. The 3D-printer that will be used for manufacturing test samples will be introduced, together with the print settings that have an influence on the structural integrity of the 3D-printed part. The importance of the print path orientation of fiber reinforced 3D-prints are examined, through test of both short and continuous fiber 3D-print materials. Tests of the fiber reinforced 3D-printed materials will establish the material properties, that will be used throughout the project. The material properties will be based on a linear elastic assumption for the two materials tested.

## 3.1 Fused Filament Fabrication

The manufacturing process of FFF is illustrated in Figure 3.1 and it starts with the filament strand. This material is inserted through an extruder that feeds the material through a heaterblock to the nozzle. The heater block heats the nozzle to the melting point of the filament and it is thus melted when extruded through the heater block and the nozzle. The material is extruded out through the nozzle and is placed on a build plate. By moving the print nozzle relative to the build plate it is possible to place the extruded material in strands next to each other and let them fuse together. This will create a solid layer that can be the foundation for the next layer and thus a 3D geometry is created.
Something that needs to be taken into account is overhang, which is the amount of material that is placed over the edge of the 3D-printed part as illustrated in Figure 3.1. If the overhang becomes more than 45°, support material is typically necessary in order to get good surface quality. Support material is extra material that is not a part of the original structure, but is placed where large overhangs are needed. The support structure is designed to be removed afterwards either mechanically or chemically.

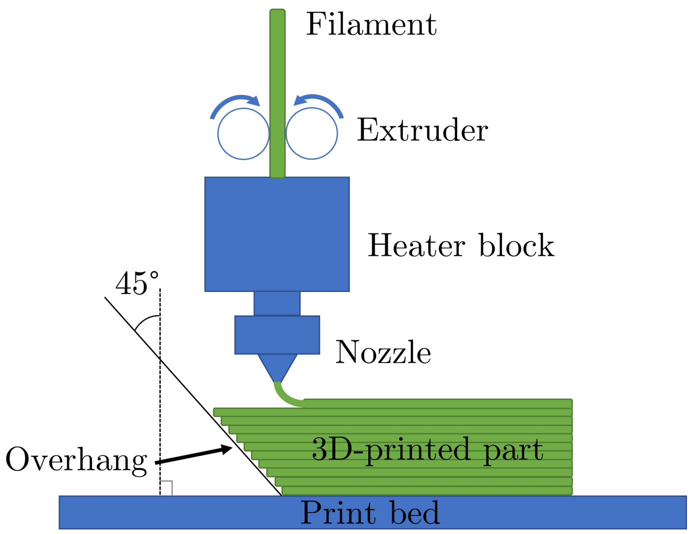


Figure 3.1: Definition of 3D-printing terminology.

The deposition pattern of the print paths can be varied depending on the specific requirements. A FFF 3D-printed structure is created from three structural components, that are walls, infill and solid top and bottom layers. The walls surround the infill and are placed along the contour of the geometry. The solid top and bottom layers are solid layers placed at the top and bottom of the structure in order to surround the infill. The infill is the material that is placed inside the structure surrounded by the walls and top and bottom layers. Infill is an internal structure and it can vary in density from 0% to 100%, where 0% is no internal material and 100% represents solid layers. These structural components can be seen in Figure 3.2, and they can be changed depending on the use case of the 3D-printed structure.

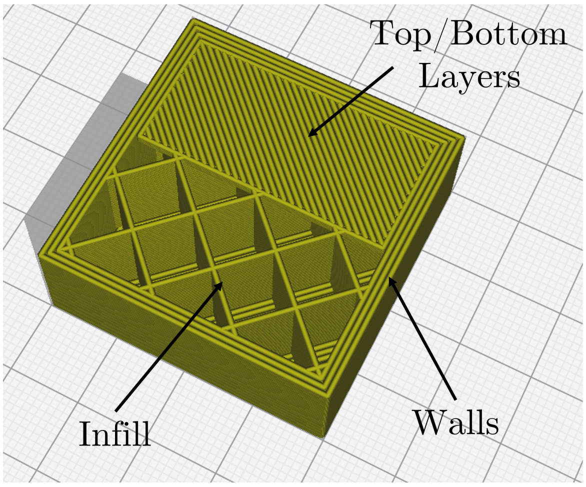


Figure 3.2: Structural parts of the geometry.

The same process can be used to manufacture fiber reinforced 3D structures. There are two types of fiber reinforced FFF additive manufacturing. The first is short fiber materials, where the filament strand includes short fibers.This type of short fiber material can be used in almost every type of FFF 3D-printer, because the filament material behaves like most 3D-printable polymer materials. One thing to be aware of is the additional wear of the nozzle caused by the fibers.

The other fiber reinforcement method is continuous fiber 3D-printing. There are two ways of doing continuous fiber FFF 3D-printing. Either the fiber and the plastic matrix are combined in a single filament strand or they are treated seperately. A method to treat them seperately is by the use of Continuous Fiber Co-extrusion (CFC), where the fiber and polymer are mixed in the nozzle (Adumitroaie et al. 2019). Both methods require special 3D-printers, that have the ability to cut the continuous fiber, when moving between print paths. The continuous fiber paths are placed like other material paths in FFF 3D printing. This can be combined with non-reinforced materials if the 3D-printer supports multi material printing.

### 3.1.1 Printer

The printer that has been chosen for manufacturing of the test specimens is the Anisoprint Composer A4, which is a FFF printer, that can print continuous fibers utilizing the CFC method (Anisoprint 2022b). This printer has been chosen since it is based on an open environment. It uses a standard G-code format, with minor changes in order to accommodate the added features of the fiber co-extrusion. The G-code is thus human readable and it can be adjusted using a simple text editor for small changes or automated by the use of scripting in for example MATLAB or Python for larger changes. This flexibility can be important in order to place the fibers in the wanted orientation.

Some of the most well known 3D-printers for continuous fiber printing are made by Markforged (Adumitroaie et al. 2019), with their Mark Two being priced similarly to the Anisoprint Composer A4. They are well known to be stable and reliable (DesignFusion 2022), but they can only be used together with their cloud-based slicer Eiger, which does not support standard G-code. Slicers will be described in more detail in Section 3.1.2. Due to the lack of flexibility of the Marforged printers the Anisoprint Composer A4 has been chosen instead.

The Anisoprint Composer A4 has a dual nozzle setup, where it can print generic 3D-printing polymers in one nozzle and continuous fibers in the other, using CFC. The continuous fiber and the co-extrusion material are mixed in the nozzle and are extruded as a material strand, like regular FFF 3D-prints. The CFC process is illustrated in Figure 3.3. The continuous fiber is pre-impregnated with an epoxy coating, in order to ensure good wetting of the fibers. This also stiffens the fiber bundle, which is necessary in order to feed it from the extruder through the nozzle. (Adumitroaie et al. 2019)

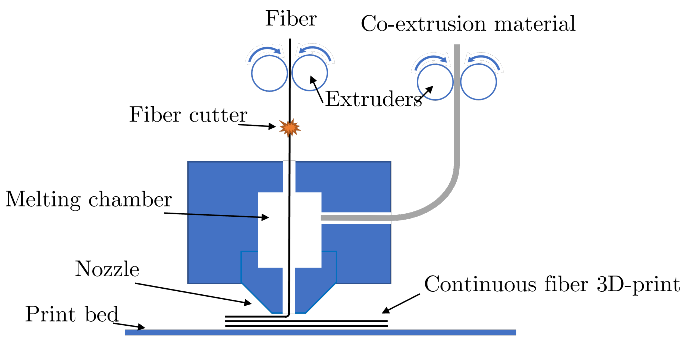


Figure 3.3: Continuous fiber co-extrusion process.

When printing with the continuous fiber it needs to be cut between the print paths. This is done by a rotating knife placed before the melting chamber. This results in some limitations on the length of the fiber paths, because the length from the knife to the exit of the nozzle determines the minimum fiber length. The minimum fiber length is 45 mm for the Anisoprint Composer A4. The fiber used for the CFC is a purpose made 1.5k epoxy impregnated carbon fiber and the co-extrusion material, can be a variety of generic 3D-printing materials.

### 3.1.2 Slicer

In order to 3D-print a geometry it needs to be converted to g-code, which is done by so-called slicers. Slicers take 3D-models which are typically in the form of Standard Tessellation Language (STL) files and divide the 3D-geometry into layers and create the print paths for each layer. These layers are typically planar. This is then converted into g-code, that the 3D-printer uses to print the geometry.
Anisoprint has their own slicer named Aura. It is made for Anisoprint's printers and outputs a special flavor of g-code designed for these printers. The Aura g-code flavor for example includes commands for, cutting the continuous fiber and preheating of nozzles when changing between the dual nozzle setup. The Aura slicer is therefore optimized to work with the Anisoprinter's. (Azarov 2021)
A comparison between the Aura slicer and the more common Cura slicer has been made. This is in order to establish the difference between the two slicers. The comparison is done by printing the same type of specimen on the Anisoprint Composer A4, with the same material and print settings, but by using g-code generated from the two different slicers. Five specimens are printed using each slicer and the material strength and Young's modulus of each specimen is tested in a tensile testing machine. The test follows the procedure given in Section 3.2. This makes it possible to see if the slicer has an impact. The results did not show a large difference in material properties as seen in Table 3.1. The same material properties can therefore be achieved by the two slicers.

| Slicer | Young's modulus | Standard deviation | Tensile strength | Standard deviation |
|---|---|---|---|---|
| Cura | 5266 MPa | 104 MPa | 72.6 MPa | 1.8 MPa |
| Aura | 5222 MPa | 223 MPa | 72.3 MPa | 0.61 MPa |

Table 3.1: Comparison of Aura and Cura slicer.

The Aura slicer will therefore be used to slice the 3D-files throughout the project, because it uses the flavor of g-code that is made for the Anisoprint composer A4. The Aura software also includes some pre-programmed material profiles, that are calibrated for the use of different materials with the Composer A4. This creates a good starting point for the selection of materials and the tuning of them, in order to get good print results. Furthermore the Aura slicer includes special features for printing with continuous fiber. One of these features is called Masks, which can be used to specify fiber directions in specific areas.
This can help to place the fibers in the directions, which are calculated by the optimization. There are although some limitations in the possible orientations. A limitation is that the fibers can only be placed in-plane since non-planar slicing is not available, but this is not a problem when considering 2D problems. Furthermore it is only possible to place fibers along contours and at a constant fiber angle.

### 3.1.3 Materials

Two different polymer materials will be utilized throughout the project. These materials are Smooth PA and CFC PA, which are polymers engineered by Polymaker for the anisoprinters. They are chosen since calibrated profiles for them are implemented in the Aura slicing software. The CFC PA will be used as the co-extrusion material for the continuous fiber reinforced material and will thus not be tested seperately.
In order to establish the material properties, testing of the material is necessary. Some of the material properties can be found in data sheets and other various sources, but because the structural properties are very dependent upon the print settings, both materials will be tested. This is done in order to validate the material properties, that can be achieved with the specific setup of slicer and 3D-printer.
Smooth PA is a fiber filled Polyamide PA12 with low moisture absorption and 10% volume fraction of short carbon fibers. The short fibers increase the mechanical properties and the printability of the material because it reduces warping, which is typically a problem when 3D-printing Polyamide (Anisoprint 2020b).
The CFC PA is PA12 as well and it is used as the co-extrusion material surrounding the continuous carbon fiber. This material is engineered to have a low viscosity in order to ensure good wetting of the fiber bundle. Furthermore it has a high solidification rate, which ensures good fiber placement (Anisoprint 2020a).
In addition to these polymeric materials a 1.5k continuous carbon fiber bundle will be used in the CFC process, together with the CFC PA. The material characteristics thus have to be determined for two materials, where one is the Smooth PA and the other is CFC PA combined with continuous carbon fibers, which will be named Continuous Carbon Fiber (CCF).

A minor test study is made in order to specify the print settings, for the two materials. Test specimens are printed with both materials and evaluated by checking the mass and through a visual inspection. Thereby the amount of extruded material is validated against the extrusion calculated in the Aura slicer. The important settings are tuned in order to get high quality parts. The settings used are described in Section 3.1.4 and 3.1.5.

### 3.1.4 Settings for Smooth PA

The most important prints settings for the structural integrity will be explained and determined for Smooth PA in Table 3.2. The layer height is an important setting for the surface quality, but also the structural strength of the part. The lower the layer height the finer the quality of the surface. The low layer height also prevents voids between the fiber paths, which can be seen in Figure 1.2. The smaller the voids the more surface area there is for the paths to fuse together. The line width defines the width of the print paths and defines minimum feature size, which is possible to manufacture.

| | |
|---|---|
| Layer height | 0.2 mm |
| Line width | 0.4 mm |
| Print temperature | 265 °C |
| Bed temperature | 60 °C |
| Flow rate | 100% |
| Print speed | 40 mm/sec |

Table 3.2: Smooth PA print settings.

Two fans are mounted on the printer, which have the function of cooling the 3D-printed part. Part cooling is not used for the Smooth PA. Polyamides like Smooth PA have the tendency of warping when 3D-printed. Warping is when the material begins lifting from the build plate and becomes lose. This is due to the material contracting on the topside when cooling. The risk of warping is therefore lowered when there is no part cooling. Another way to lower the risk of warping is by using a brim or a raft as the build plate adhesion. This setting enlarges the first layer around the structure. The larger first layer gives a better adhesion to the build plate due to the larger surface area. No significant changes are made compared to the standard profile in Aura, in order to get good results for the Smooth PA material.

The test specimen used to test the Smooth PA is based on DS/ISO 3167 and is shown in Figure 3.4. The material orientation is ensured by using 100% unidirectional infill in the direction of interest. Furthermore one outer wall is used in order to ensure smooth surfaces without stress concentrations.

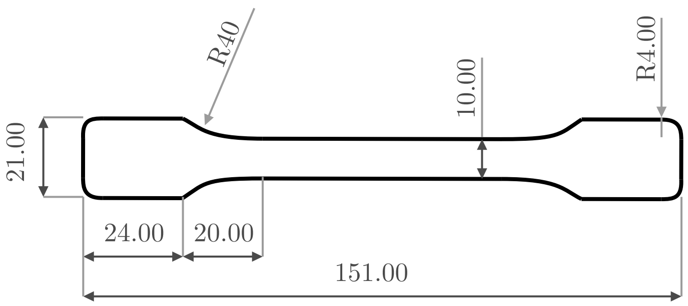


Figure 3.4: The dimensions of the tensile test specimen. $t = 3.7\,\mathrm{mm}$.

FFF 3D-printed parts are normally not considered to have anisotropic constitutive properties in the xy-plane (Mirzendehdel, Rankouhi, and Suresh 2017). The Smooth PA will exhibit orthotropic constitutive properties due to the short fibers in the material. These fibers are aligned during the manufacturing process and thus the stiffness and strength are increased in the printing direction. This alignment is seen in Figure 3.5. It is therefore necessary to test the material both in the longitudinal and transverse direction to the print paths, in order to specify the material properties.

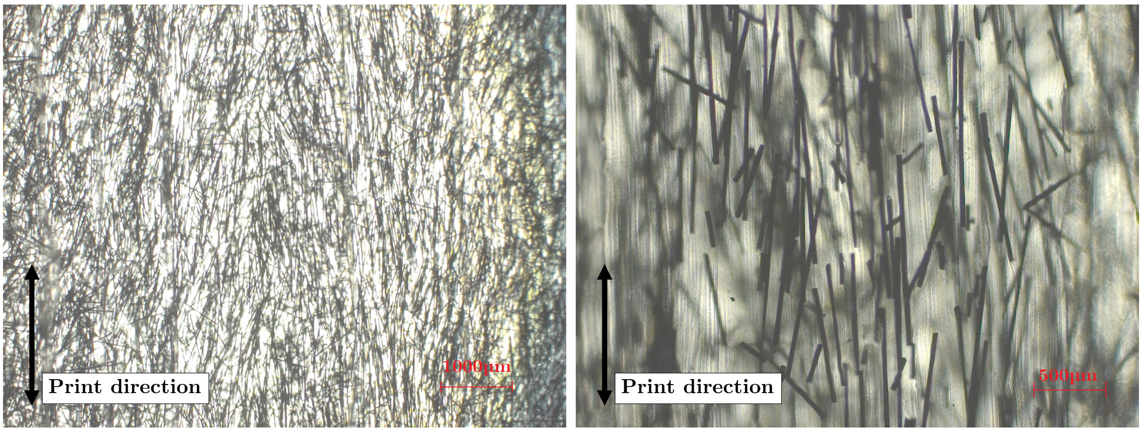


(a) 5x magnification. (b) 10x magnification.

Figure 3.5: Microscopy images of Smooth PA, showing the alignment of the short fibers.

### 3.1.5 CCF settings

The settings for the CCF material can be seen in Table 3.3. The layer height and the line width are larger for the CCF compared to the Smooth PA. This is due to the added continuous fiber, taking up more space.

| | |
|---|---|
| Layer height | 0.36 mm |
| Line width | 0.75 mm |
| Print temperature | 250 °C |
| Bed temperature | 60 °C |
| Flow rate polymer | 86% |
| Print speed | 10 mm/sec |

Table 3.3: Print settings for CCF with CFC PA as co-extrusion material.

Two limitations when doing continuous fiber 3D-printing is the minimum fiber length as mentioned in Section 3.1.1 and the bend radius. The minimum fiber length defines the shortest fiber path, that can be printed by the 3D-printer, while the bend radius is the radius of the fiber path when changing directions. This is illustrated in Figure 3.6. When the fiber bend radius becomes too small, the fiber placement will become uneven and the fiber bundle can be damaged.

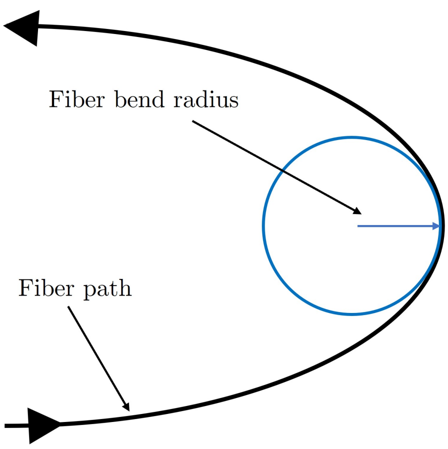


Figure 3.6: Fiber bend radius.

The problem with warping is not as significant when because the material is stiffer, due to the continuous fiber. Part cooling is therefore added to the CFC printed structures in order to solidify the material faster, which ensures that the fiber keeps the correct placement.

Typically the continuous fiber composite will be surrounded by a shell of a polymer material, in order to ensure a smooth surface and thus avoid stress concentrations. A CCF specimen was therefore printed with one outer wall and one top and one bottom layer made of Smooth PA. When tested in a tensile testing machine, this resulted in fiber pull out, in the transition between the CCF and the Smooth PA. The fiber pull out can be seen in Figure 3.7. In order to get the material data for the CCF, it thus needs to be printed without the Smooth PA shell to avoid the fiber pull out.

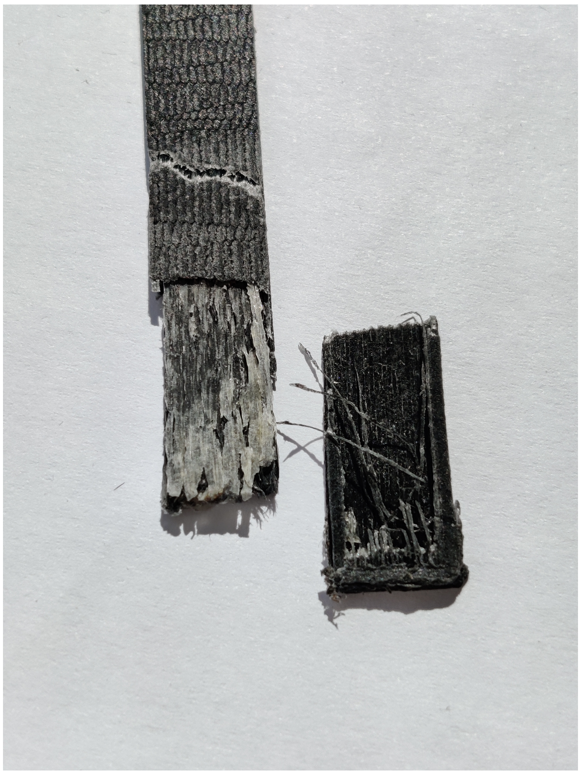

Figure 3.7: Fiber pull out at the end of the CCF specimen.

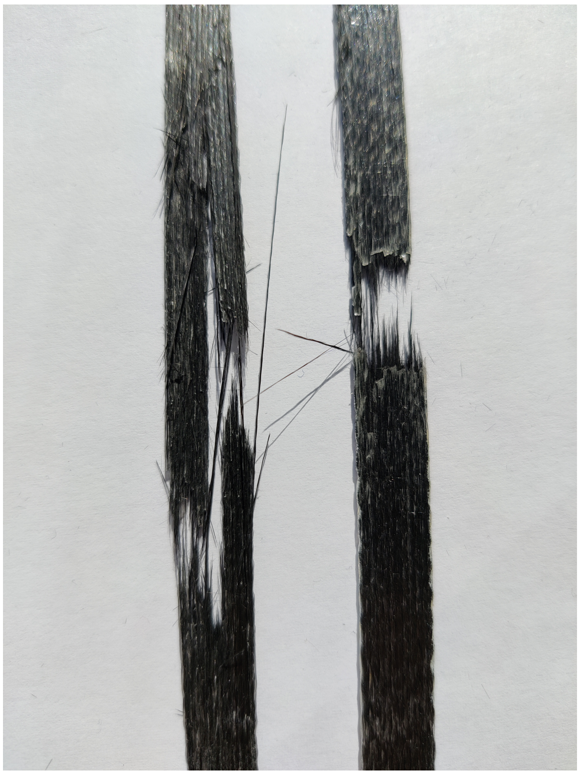

Figure 3.8: Fractures with the right being less brushlike than the left.

Furthermore low adhesion between the fibers is observed. This can be seen from the fracture, which is brushlike as seen in Figure 3.8. Minor signs of underextrusion are also observed, thus the flow rate of the CFC PA polymer has been increased, to improve the interface strength between the fiber and the polymer. This resulted in a less brushlike fracture, although still not perfect, as seen in Figure 3.8 and the settings given in Table 3.3, will thus be used for the CCF test specimens.

The test specimens for testing the continuous carbon fiber follows the geometry given in DS/EN ISO 527-5, but the dimensions are reduced from 250 mmX15 mmX1 mm to the values given in Figure 3.9. This reduction in size is in order to lower the production time and reduce the material cost, but still having a reasonable size in order to perform the tests.

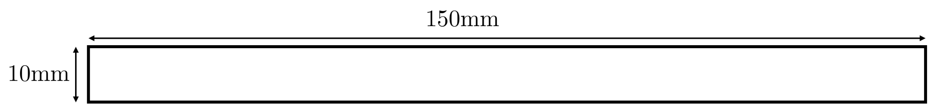


Figure 3.9: Dimensions of CCF specimen. $t = 0.75\,\mathrm{mm}$.

According to DS/EN ISO 527-5 tabs should be added at the ends of the specimen to prevent failure in the clamped area. It has been tried bonding these tabs to the specimen using both generic CA-glue and the 2-component epoxy Huntsman Araldite 2011, but both did not bond to the specimen and sheared off. Therefore 2 layers of sandpaper of grit 400 have been used instead, as suggested in DS/EN ISO 527-5 following the guidelines given in Annex B of the standard. This resolved the problem of failure in the clamping area.

## 3.2 Test setup

The orthotropic material properties are measured by performing tensile tests of the different print orientations of the material. Five specimens are tested in each orientation in order to get a significant sample size. Only the in-plane material properties will be characterized since this project is only considering 2D problems. Two different deposition patterns are investigated which are 0° and 90°, with respect to the tensile direction as shown in Figure 3.10.

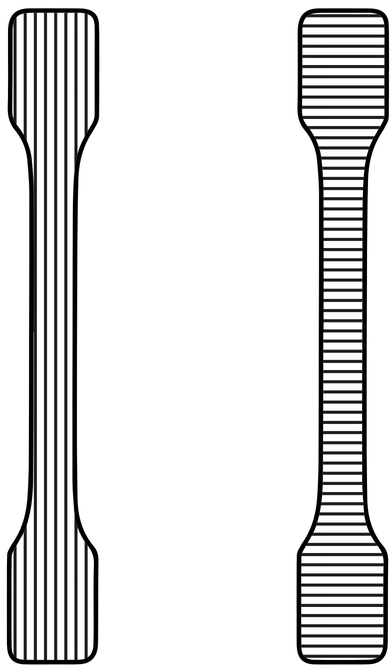

(a) 0° (b) 90°

Figure 3.10: Material orientations.

The tensile tests are performed on Instron tensile testing machines with different load cells corresponding to the possible max loads of the different materials. The Smooth PA will thus be tested using a 5 kN load cell. The CCF will be tested using a 50 kN load cell for the 0° direction and a 2 kN load cell for the 90° direction. This ensures high precision of the force measurements. The stress can thus be calculated from the measured force and the cross sectional area of the specimens. The dimensions are measured at 3 points with a precision of 0.01 mm and the measurements are averaged.
An extensometer will be used to measure the longitudinal strain of the test specimens. The strain will be used together with the stress to calculate the Young's modulus, which is done by doing a least squares linear fit in the region $0.0005 < \varepsilon < 0.0025$ as prescribed by DS/EN ISO 527-1.

Since the Poisson's ratio is also needed it is necessary to measure the transverse strains. The best option to do this would be to use a transverse extensometer, since it is precise and easy to use both during testing and for post processing of the data. No transverse extensometers are available though and thus a different method has to be used.
Therefore the optical displacement measurement technique Digital Image Correlation (DIC) will be used. DIC can be used to measure the displacements on the surface of the test specimens. These displacements are determined by taking pictures of the test specimen during the test. It is afterwards possible to compute the displacement of the individual pixels by correlating the pictures during the test. From the displacements it is possible to calculate the complete strain field and thus the Possion's ratio. The DIC test setup can be seen in Figure 3.11.

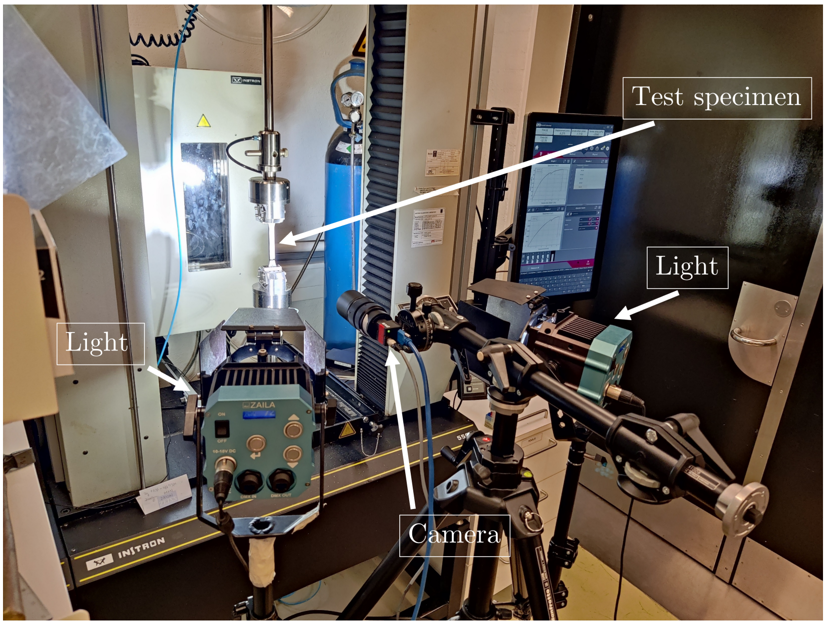


Figure 3.11: DIC tensile test setup.

In order to perform DIC, the test specimens have to be painted to have a stochastic pattern of black and white dots. Pictures of the test specimen are then taken throughout the tensile test. These pictures are analysed and the correlation between pixels, can be tracked throughout the test. By knowing the correlation, the displacement of pixels can be calculated on the surface of the test specimens. The strains can then be found from the displacements.(Blaber and Antoniou 2017)
This process is thus more complex and time consuming than using a transverse extensometer. Furthermore it is more prone to errors since it requires many user interaction for example, when painting the stochastic pattern and setting the parameters for the camera and for the image tracking algorithm. Furthermore it requires that the paint deforms with the specimens in order to avoid cracking of the paint.

### 3.3 Results for Smooth PA

The stress-strain curves from the tensile tests are shown in Figure 3.12 for both the 0°- and 90° direction of the Smooth PA. The 0° direction breaks at maximum tensile strength, where the 90° direction begins necking before breaking. Both results have a linear elastic material behavior at low strains, but it becomes more non-linear at higher strains. The linear assumption is thus not perfectly accurate at high strains. The small dips in the stress at 60 and 30 MPa for the 0° and 90° respectively are caused by the removal of the longitudinal extensometer. This pauses the test temporarily and thus allows for stress relaxation. Since the strain after these dips is calculated from the cross-head movement of the tensile testing machine it is less accurate.

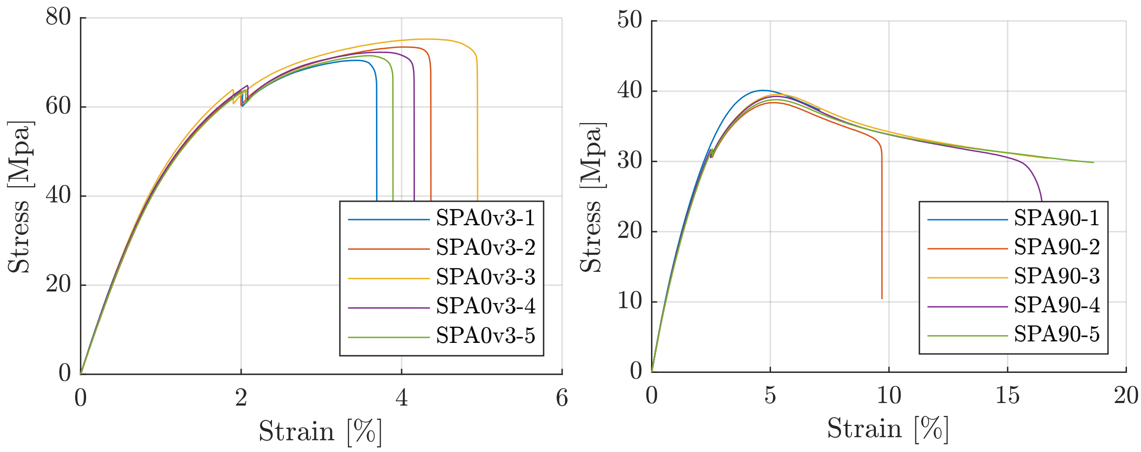


(a) 0° direction. (b) 90° direction.

Figure 3.12: Stress-strain diagrams for Smooth PA.

#### 3.3.1 Young's modulus and strength

The results given in Table 3.4 from the tensile tests of the Smooth PA show consistent material behavior for each material direction respectively. The 0° direction has a consistent tensile strength of around 73 MPa, with a Young's modulus of $E_1$ =5300 MPa. The 90° direction has a tensile strength of 39 MPa and Young's modulus of $E_2$ =1800 MPa. This clearly shows the difference between the material directions, which concludes that the material is orthotropic.

| Direction | Young's modulus | Standard deviation | Tensile strength | Standard deviation |
|---|---|---|---|---|
| 0° | 5300 MPa | 104 MPa | 72.6 MPa | 1.8 MPa |
| 90° | 1800 MPa | 32 MPa | 39 MPa | 0.67 MPa |

Table 3.4: Material properties of Smooth PA.

### 3.3.2 Poisson's ratio

Based on the strain measurements from the DIC analysis the major and minor Poisson's ratios are calculated. The parameters and resolution of the strains and displacements are given in Appendix A. Both the resolution and the correlation values are within the expected range. The correlation values for the 90° tests though are slightly higher than for the 0° tests. This is a result of the paint partially cracking in between the print paths.
To determine the Poisson's ratio the longitudinal strain $\varepsilon_1$ and transverse strain $\varepsilon_2$ is calculated in each pixel and afterwards the Poisson's ratio is calculated in each pixel using Equation 3.1. The Poisson's ratios for each pixel are averaged to get a single value for each picture. The Poisson's ratio is only calculated until the extensometer is removed. The averaged Poisson's ratio for each picture is given in Figure 3.13.

$$v_{12} = -\frac{\varepsilon_2}{\varepsilon_1} \tag{3.1}$$

Due to low signal-to-noise ratios in the first pictures of the DIC tests, the first 20 pictures will be excluded from the calculation of the Poisson's ratio. The Poisson's ratio will be calculated as a mean value of each test. The mean between the five test samples will be found and used as the Poisson's ratio for the given material and direction.

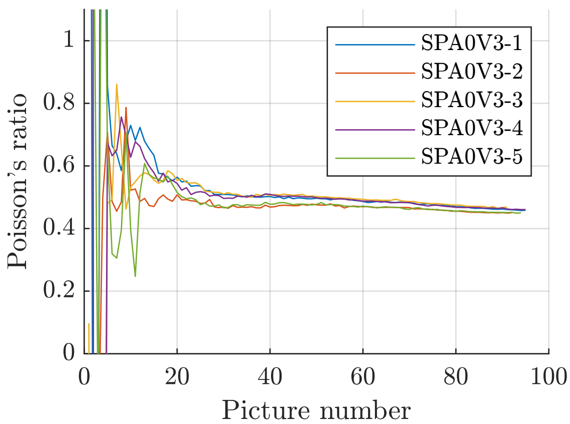


Figure 3.13: Development of Poisson's ratio for 0° Smooth PA.

The results for the Poisson's ratios can be seen in Table 3.5. The results for the Smooth PA are consistent across the five test specimens in each direction, this is seen by the low standard deviation.

| Direction | Poisson's ratio | Standard deviation |
|---|---|---|
| $v_{12}$ | 0.48 | 0.0133 |
| $v_{21}$ | 0.16 | 0.0151 |

Table 3.5: Poisson's ratio for Smooth PA.

### 3.3.3 Sanity check of constitutive properties

In order to check the results, the symmetry condition of the constitutive matrix has been utilized. This condition is given in Equation 3.2. The results are given in Table 3.6 and as is seen the difference is approximately 2 %. This is within a reasonable margin between the two tests.

$$\frac{-v_{12}}{E_1} = \frac{-v_{21}}{E_2} \tag{3.2}$$

| $\frac{-v_{12}}{E_1}$ | $\frac{-v_{21}}{E_2}$ | Deviation |
|---|---|---|
| $-91.04 \cdot 10^{-6}$ | $-89.17 \cdot 10^{-6}$ | 2.1 % |

Table 3.6: Evaluation of symmetry of constitutive matrix.

### 3.3.4 Conclusion for Smooth PA

The results obtained above match the results given in Anisoprint (2020b). It is thus assumed that the other material properties match as well and thus the shear and compression properties are taken from the datasheet. The material properties that will be used throughout the rest of the project for the Smooth PA are thus given in Table 3.7. Here $X$ refers to the strength along the fiber orientation and $Y$ refers to the strength perpendicular to the fiber orientation. Indices $t$ and $c$ refer to the properties in tension and compression respectively. S is the shear strength.

| Property | Value |
|---|---|
| $E_1$ | 5300 MPa |
| $E_2$ | 1800 MPa |
| $v_{12}$ | 0.48 |
| G | 411 MPa |
| $X_t$ | 72.6 MPa |
| $X_c$ | 81.4 MPa |
| $Y_t$ | 39 MPa |
| $Y_c$ | 50 MPa |
| $S$ | 16 MPa |

Table 3.7: Material parameters for Smooth PA.

## 3.4 Results for CCF

The stress-strain diagrams for the CCF specimens, are shown in Figure 3.14. The results from test CCF0-1 have been excluded from the test results, due to damaging the specimen during mounting in the tensile testing machine. This specimen was subjected to compressive loads during clamping, which resulted in buckling of the specimen, which might have broken some of the fibers. The specimen broke just after removing the extensometer at around 400 MPa. The test CCF0-1 is therefore not a part of the results.
From Figure 3.14a it is seen that the stiffness changes after removing the extensometer. This is not expected, but could be due to the less accurate displacement measurements from the cross-head, which are used to calculate the strains here. These measurements typically result in lower stiffness due to deformation of the tensile testing machine. It is thus expected that the non-linearity is a result of the testing methodology and not due to the material being non-linear.
For the 90° test specimens an extensometer has not been used due to the fragility of the specimens. The strain in the longitudinal direction was therefore measured by the displacement of the cross-head of the tensile testing machine. This is not expected to be a problem due to the low required force.

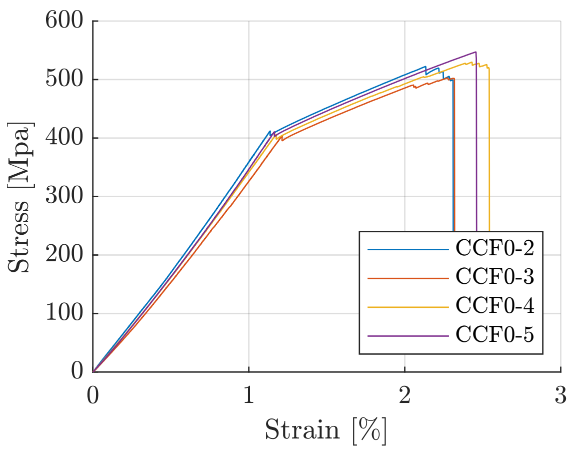


(a) 0° direction.

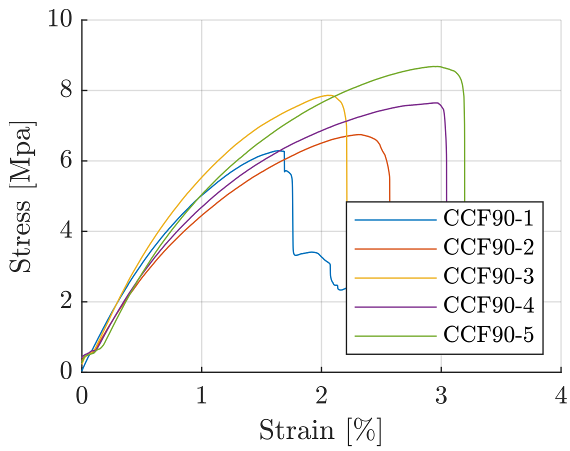


(b) 90° direction.

Figure 3.14: Stress-strain diagrams for CCF tests in given directions.

### 3.4.1 Young's modulus and strength

Averaging the four tests, results in a tensile strength of 525 MPa and a Young's modulus of 31 000 MPa for the 0° direction. The 90° direction is not as strong, with an average tensile strength of 7.4 MPa and Young's modulus of 623 MPa. Since the load transverse to the fiber direction is carried mainly by the matrix material, it was expected that the strength should be around 56.8 MPa, since this is the strength of the CFC PA (Anisoprint 2020a).
The low strength in the 90° direction might be the cause of the continuous fibers being placed too close. The fibers will end up touching each other and therefore there is no space for the CFC PA to bind them together. This can be seen in Figure 3.15, where it is also seen that

the plastic material has been pushed out the side instead of being in between the fibers. The geometry of the fiber test specimen is not optimal for continuous fiber 3D-printing. Better results could thus have been achieved if a wider geometry was used, where the fiber paths could be placed more evenly.

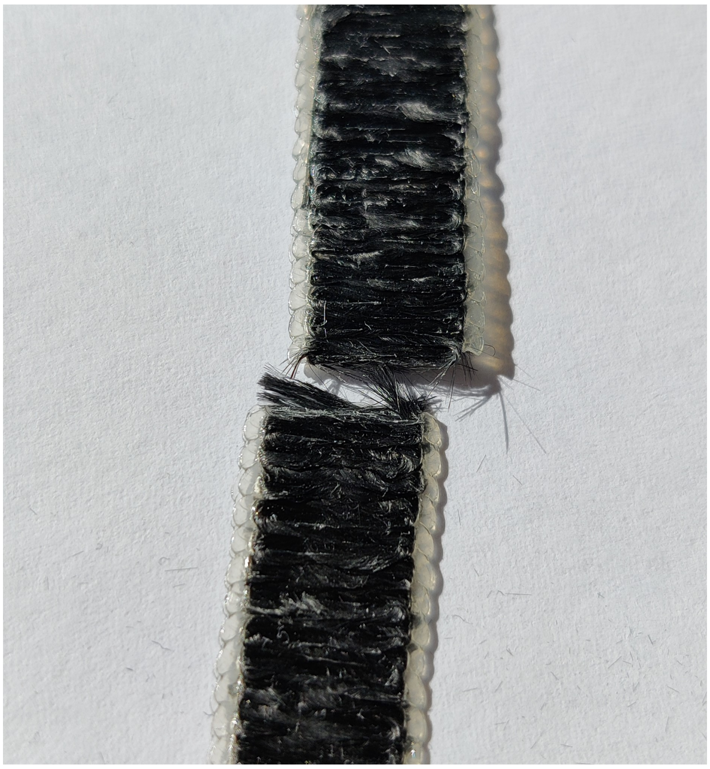

Figure 3.15: Low wetting of fiber bundles.

CCF offers a high strength and stiffness in the 0° direction, but a low strength and stiffness in the 90° direction. The material properties for the CCF, can be seen in Table 3.8.

| Direction | Young's modulus | Standard deviation | Tensile strength | Standard deviation |
|---|---|---|---|---|
| 0° | 31 000 MPa | 1967 MPa | 525 MPa | 18.5 MPa |
| 90° | 623 MPa | 57.5 MPa | 7.4 MPa | 0.94 MPa |

Table 3.8: Material properties for CCF.

### 3.4.2 Poisson's ratio

The DIC results for the CCF test specimens were not conclusive due to excessive noise in the results. During the testing of the CCF the stochastic paint pattern cracked, which resulted in noisy data. This was the same for all five CCF tests. It was therefore not possible to get a Poisson's ratio by doing DIC.

In order to get the Poisson's ratio a new specimen has been manufactured, where a strain gauge is glued to the surface of the specimen as seen in Figure 3.16. The strain gauge used is a Tokyo Sokki Kenkyujo Co. FCA-2-11-3L angle gauge, in order to get the strains in the two directions. The gauge length is 2 mm with a gauge factor of 2.1 on both gauges.

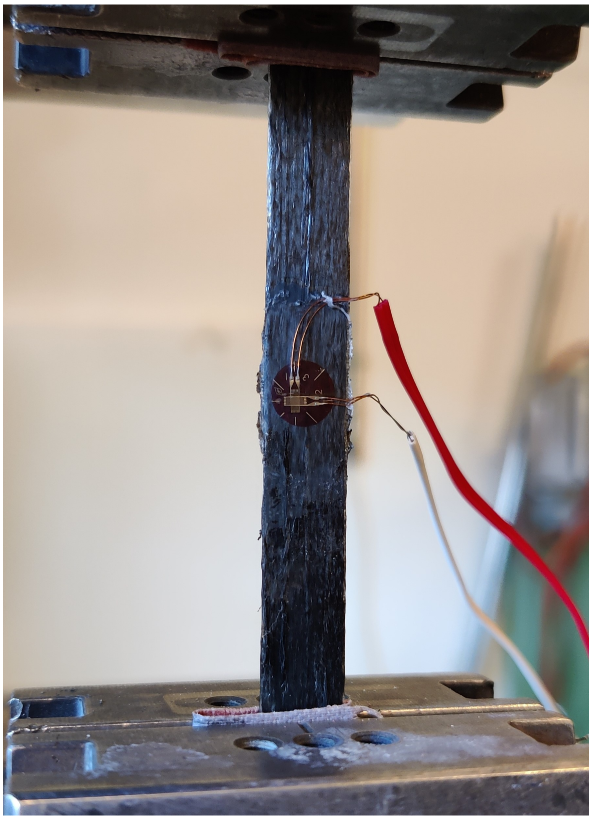

Figure 3.16: Strain gauge specimen mounted in tensile testing machine.

The test is performed like the DIC test, but logging the strain data from the strain gauge instead of taking pictures during the testing. The results from the strain gauge can be seen in Figure 3.17a.

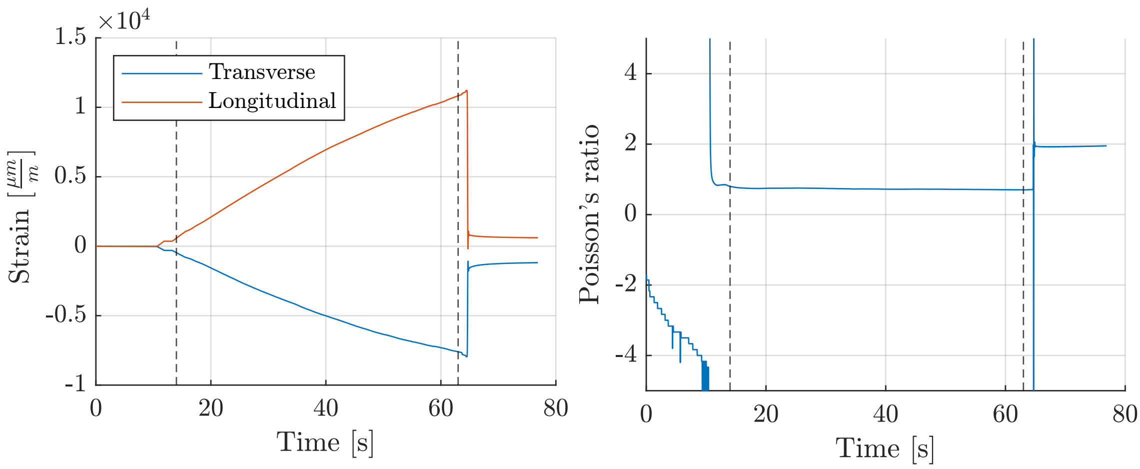


(a) Strains in the longitudinal and transverse directions.

(b) Development of Poisson's ratio.

Figure 3.17: Results for CCF specimen using strain gauge.

The test resulted in a Poisson's ratio of 0.73, which is calculated as a mean of the values within the time from 14 seconds to 63 seconds, as marked with the dashed lines in Figure 3.17. This is done in order to remove the noise at the start and the end of the test, which can be seen in Figure 3.17b. The mean Poisson's ration of 0.73 has a standard deviation of 0.0175.

### 3.4.3 Conclusion for CCF

In the same way as for the Smooth PA, not all properties have been tested. The remaining material properties although are not given explicitly in a datasheet as for the Smooth PA. The properties have thus been estimated based on different sources. It should although be noted that not all sources use the same matrix material, but they are assumed to be equivalent. The results are given in Table 3.9.

| Property | Value | Matrix material | Source |
|---|---|---|---|
| $E_1$ | 31 000 MPa | | |
| $E_2$ | 623 MPa | | |
| $v_{12}$ | 0.73 | | |
| G | 420 MPa | PLA | Azarov et al. (2019) |
| $X_t$ | 525 MPa | | |
| $X_c$ | 290 MPa | PETG | Anisoprint (2022a) |
| $Y_t$ | 7.4 MPa | | |
| $Y_c$ | 7.4 MPa | | |
| $S$ | 16 MPa | Smooth PA | Anisoprint (2020b) |

Table 3.9: Material properties for the CCF.

# 4 Topology and fiber orientation optimization

Throughout this chapter the process of doing simultaneous topology and fiber orientation optimization will be outlined. There are 3 fundamental parts of this optimization, which are the mathematical model of the system, the optimization problem and the solver. The solver will be introduced in the next chapter. The mathematical model is a model of the physical system, which is to be optimized. Here a finite element model using the bilinear element formulation will be used to discretize the system. This will be used to calculate the failure index in order to determine if the strength is sufficient.
The optimization problem describes the formulation of the optimization problem. This includes both how the material is distributed and how the fiber orientation is included in the optimization. Density based topology optimization will be described, how it is formulated to be a continuous optimization problem and how filtering techniques can be applied. Furthermore strength based optimization will be introduced together with the Tsai-Wu failure criteria which is used.
Different methods for fiber angle optimization will be introduced and discussed, and the discrete material optimization will be implemented. At the end of this chapter the design sensitivity analysis is presented including the expressions for the analytical sensitivities.

## 4.1 Mathematical model

In order to determine the response of the structure a mathematical model of the system is setup. The mathematical model is based on the finite element method, which discretizes the structure into small elements and calculates the displacements and deformations of these elements. This is done by minimizing the potential energy, which yields the equality condition given in Equation 4.1.

$$\{F\} = [K]\{U\} \tag{4.1}$$

$\{F\}$ represents the outer forces, while $\{U\}$ is the displacements and $[K]$ is the stiffness matrix. Everywhere in the structure, either the outer force or the displacement has to be given and thus the other can be calculated if the stiffness matrix is known.
The global stiffness matrix can be assembled from the element stiffness matrix, which is defined in Equation 4.2.

$$[k_e] = \int_{-a}^{a}\int_{-b}^{b}[B]^T[C_e][B]t dx dy \tag{4.2}$$

The value $t$ is the thickness, $[C_e]$ is the constitutive matrix of the material in the element and $[B]$ is the strain-displacement matrix. $a$ and $b$ define the element side lengths as seen in Figure 4.1. The formulation of the strain displacement matrix is given in Equation 4.3.

$$[B] = [\partial][N] \tag{4.3}$$

$[N]$ is the shape function used for interpolating the results between the nodal values and $[\partial]$ is the partial differential operator.
The elements are formulated using bilinear interpolation because they are simple and computationally efficient. The shape functions for this element formulation are given in Cook et al. (2002). Due to the bilinear interpolation only constant stress states can be represented within each element, without nodal extrapolation and averaging. Therefore smaller elements are needed to correctly represent stress gradients. This is not a problem since the element size determines the resolution of the topology optimization, as described in Section 4.2 and thus small elements are needed anyway.
Stress gradients are especially present at stress concentrations thus they will be underestimated. For doing stress constrained optimization, this can be a good thing since the load typically distributes more during experimental tests than the model predicts, due to the nonlinear material behavior.
The bilinear elements are only accurate when the element edges are parallel to the global axes. If the edges are not axis parallel the element does not follow the convergence criteria of $C^{m-1}$-continuity, which is the second convergence criteria by Cook et al. (2002). Since a structured mesh will be used this is not a problem either.

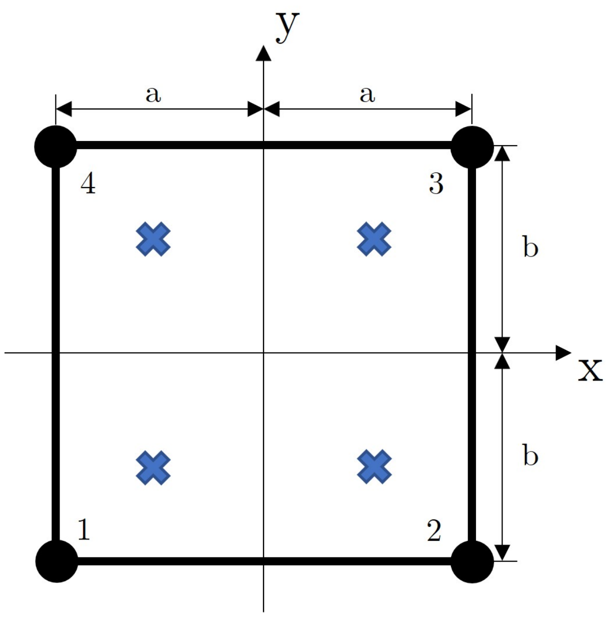


Figure 4.1: Definitions for bilinear element.

In order to calculate the stiffness matrix it is computationally inefficient to use the formulation given in Equation 4.2 due to the symbolic variables, thus it is necessary to reformulate the equation. Due to the simplicity of the bilinear elements an analytical expression for the stiffness matrix can be derived but in order to ensure generality this formulation has not been used. Instead Gauss integration has been used with full integration. Gauss integration utilizes the fact that the integral can be calculated as a weighted sum of the function value at given positions. These positions for the bilinear element are marked with blue crosses in Figure 4.1. The element stiffness matrix is thus calculated using Equation 4.4 where $x_{(i/j)}$

and $y_{(i/j)}$ are the coordinates of the Gauss points while $w_{G,ij}$ is the weight of the Gauss point.

$$[k_e] = \sum_{i=1}^{2}\sum_{j=1}^{2} w_{G,ij}[B(x_i,y_j)]^T[C_e][B(x_i,y_j)]t \tag{4.4}$$

By utilizing the stiffness matrix the displacements are calculated. Typically strength is determined based on the stress state, thus it is necessary to calculate the stresses. This is done by utilizing Equation 4.5. The strain-displacement matrix $[B_e]$ is calculated at the center of the element since this is the superconvergent point and thus the stresses will be the most accurate here.

$$\{\sigma_e\} = [C_e][B_e]\{u_e\} \tag{4.5}$$

The stresses calculated are in the global coordinate system since both the constitutive matrix $[C_e]$ and the displacements $\{u_e\}$ are given in the global coordinate system. In order to determine failure the stresses are needed in the material coordinate system since the strength parameters are determined in this coordinate system. Therefore the stresses are rotated to the material coordinate system using Equation 4.6. The global element stresses $\{\sigma_{glo,e}\}$ are calculated from Equation 4.5 and $\{\sigma_{mat,e}\}$ denotes the stresses in the material coordinate system. In the transformation matrix $[T]$ the angles are given from the global to the local coordinate system using the same notation as Jones (1999).

$$\{\sigma_{mat,e}\} = [T]\{\sigma_{glo,e}\} \tag{4.6}$$

## 4.2 Density based topology optimization

Because the finite element method is used to represent the physical system, the structure is divided into multiple elements. A simple way to optimize the geometry would thus be to let these elements either represent solid or void material. Hereby the geometry is built up of the solid elements and thus the resolution of the finite element mesh determines the resolution of the topology optimization.

The problem with this method is that it results in a discrete optimization problem, which is not very well suited for gradient based solvers. Therefore the density based method was introduced by Bendsøe and Kikuchi (1988), and the interpolation of the intermediate material stages using the continuous density variable was introduced by Bendsøe (1989). Hereby the optimization problem has been converted into a continuous optimization problem, which can be efficiently solved by gradient based optimization algorithms.

### 4.2.1 Stiffness

Since these intermediate densities are non-physical the final solution has to include only solid or void elements. In order to achieve this the intermediate densities are penalized. This is done by interpolating the stiffness using the Solid Isotropic Material with Penalization (SIMP) method, which is given in Equation 4.7. Here $[C_e]$ is the resulting element constitutive matrix, $[C_0]$ is the constitutive matrix of the material, $x_e$ is the element density and $p$ is a penalization factor.
The parameter $p \geq 3$ is recommended by Bendsøe and Sigmund (1999) due to physical consistency when $v_{12} = \frac{1}{3}$. Therefore typically $p = 3$, but in some cases a continuation approach on $p$ is necessary in order to ensure a strong local minimum (Aage et al. 2017).

$$[C_e] = x_e^p [C_0] \tag{4.7}$$

This method can also be extended to orthotropic materials by using the exact same power law as described above.

The stiffness is a common objective to maximize. This is a simple problem to solve since it can be formulated as a minimization of the compliance $C$, which is a global criterion as given in Equation 4.8.

$$C = \{U\}^T [K] \{U\} \tag{4.8}$$

Here $\{U\}$ is the nodal displacements and $[K]$ is the stiffness matrix, which can be calculated as described in Section 4.1 using the penalized constitutive matrix given in Equation 4.7.

### 4.2.2 Multimaterial topology optimization

By utilizing FFF 3D-printing it is possible to manufacture parts that include multiple materials. The topology optimization should thus be able to take into account the multiple materials available. This was introduced by Sigmund and Torquato (1997) for designing structures with extreme thermal expansion using two distinct materials and a void phase.
The constitutive matrix can be calculated using Equation 4.9, which is a direct expansion of Equation 4.7 as proposed by Gibiansky and Sigmund (2000). The parameter $x_{e1}$ determines if material is present where $x_{e1} = 1$ or not present $x_{e1} = 0$, while $x_{e2}$ determines which one of the two materials is present. The constitutive matrices for the distinct materials are given by $[C_1]$ and $[C_2]$ respectively.

$$[C_e] = x_{e1}^p \Big( (1 - x_{e2}^p)[C_1] + x_{e2}^p [C_2] \Big) \tag{4.9}$$

This can also be expanded to include more materials than only two, but it tends to get stuck in local minima, when more than 3 phases (2 materials and a void phase) are considered (Stegmann and Lund 2005).

## 4.3 Filters

If the density based topology optimization method is used directly as described above, the results will be nonphysical due to problems with checkerboarding and geometries that are impossible to manufacture. Checkerboarding can be seen in Figure 4.2 and is a result of the finite elements being artificially stiff when arranged in this checkerboard pattern. The problem can be reduced by using higher order elements (Sigmund 1994).

Figure 4.2: Density based optimization without filter resulting in checkerboarding.

### 4.3.1 Mesh-independent filtering

Multiple methods have been invented to alleviate the checkerboarding problem, but the most popular method is to use mesh-independent filtering, due to its efficiency and easy implementation (Sigmund 2007). These filters are the sensitivity filter (Sigmund 1994) and the density filter (Bourdin 2001) (Bruns and Tortorelli 2001). These filters are used for smoothing the sensitivities and the densities respectively. The sensitivity or density in an element is calculated based on the values given in the surrounding elements using a linear weighting function as shown in Figure 4.3. The weighting function is calculated using Equation 4.10, where $R$ is the filter radius and $|o_i - o_e|$ is the distance between the element centers of element $e$ and $i$.

$$H_{ei} = \max(0, R - |o_i - o_e|) \tag{4.10}$$

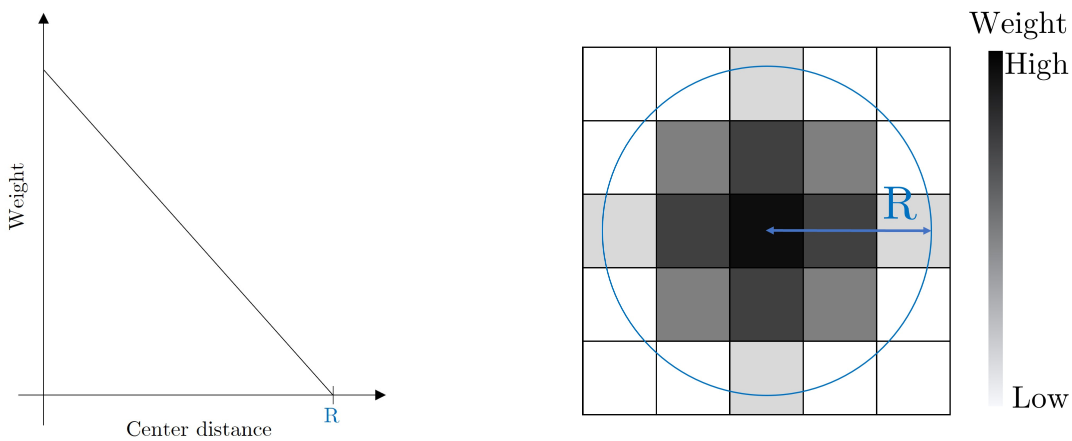


(a) Linear weight function.

(b) Weight of neighbouring elements. The blue circle indicates the filter, with radius $R$.

Figure 4.3: Definition of weight function.

The sensitivity filter only changes the sensitivities and not the design variables, thus they become inconsistent with respect to the design variables. It has shown in practice to work for compliance problems but it can be problematic with regards to stress constrained problems as introduced in Section 4.4 due to the higher degree of non-linearity (Le et al. 2010). The density filter on the other hand uses consistent sensitivities and the effects can be interpreted physically. Therefore the density filter will be utilized as given in Equation 4.11.

$$\bar{x}_e = \frac{\sum_{i=1}^{n_{elem}} H_{ei} \cdot V_i \cdot x_i}{\sum_{i=1}^{N_{elem}} H_{ei} \cdot V_i} \tag{4.11}$$

$n_{elem}$ is the number of elements and the volume of element $i$ is denoted $V_i$.

### 4.3.2 Projection filter

Since the density filter smooths the density distribution, intermediate densities will be added. In order to reduce the amount of intermediate densities a projection filter can be utilized, which projects the densities towards 0 or 1. Multiple projection filters exist including the heaviside projection filter (Guest, Prévost, and Belytschko 2004), modified heaviside projection filter (Sigmund 2007) and the generalized threshold projection filter (Xu, Cai, and Cheng 2010).

All these projection filters utilize a smoothed heaviside step function to do the projection, but due to its generality the threshold projection filter will be utilized throughout this project. The original formulation was simplified by Wang, Lazarov, and Sigmund (2011) and this simplified formulation, given in Equation 4.12 will be utilized.

$$\bar{\bar{x}}_e = \frac{\tanh(\beta\eta) + \tanh(\beta(\bar{x}_e - \eta))}{\tanh(\beta\eta) + \tanh(\beta(1 - \eta))} \tag{4.12}$$

The parameter $\beta$ is a smoothing parameter that determines the degree of sharpening, while $\eta$ determines the projection limit. If the density is below $\eta$ it will be projected towards 0 while it will be projected towards 1 if it is above $\eta$. The effect of varying these parameters is shown in Figure 4.4. In order to avoid a local minimum $\beta$ can be gradually raised using a continuation approach, as proposed for the original heaviside filter by Silva, Beck, and Sigmund (2019).

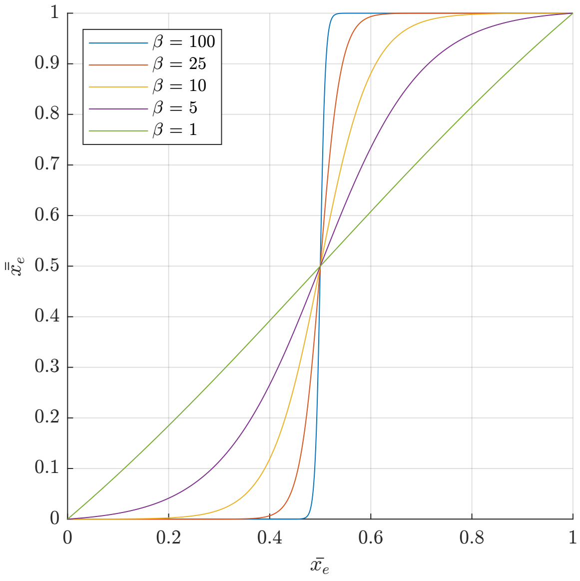


(a) Influence of $\beta$ when $\eta = 0.5$.

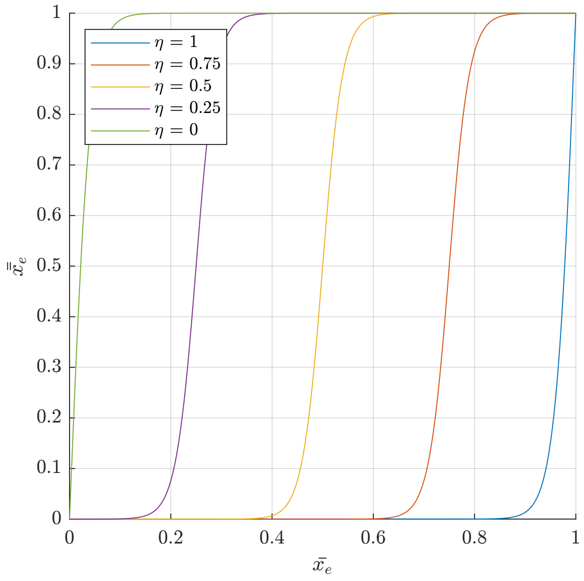


(b) Influence of $\eta$ when $\beta = 25$.

Figure 4.4: Influence of the parameters on the threshold projection filter.

When doing stress constrained topology optimization $\beta$ should not be increased to much, because this will result in a very discrete design, that can cause stress concentrations. If the design gets to a fully 0 or 1 density a boundary, which is not parallel to the elements will result in staircasing as shown in Figure 4.5 and stress concentrations will arise at the corners. Therefore $\beta$ should be limited by the value given in Equation 4.13 for stress constrained problems. (Silva, Beck, and Sigmund 2019)

$$\beta_{max} = \frac{R}{l_e} \tag{4.13}$$

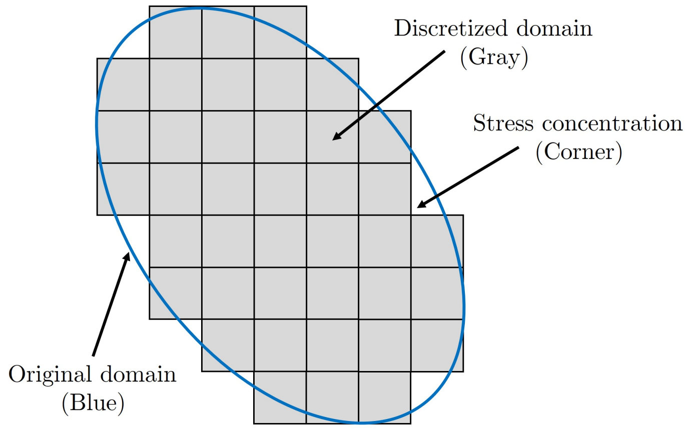


Figure 4.5: Difference between original and discretized domain, causing staircasing.

### 4.3.3 Minimum length scale

In addition to avoiding checkerboarding the filters described above introduce a minimum length scale on the design. This ensures that the geometry can be manufactured since small features are removed. By combining the density filter with the threshold projection filter a minimum length scale is applied both to the solid and void phase equal to the filter radius $R$.

This minimum length scale is not fulfilled at the edges of the domain, since the effective filter size is reduced here as shown in Figure 4.6a. This resembles a homogeneous Neumann boundary condition, which is only correct at symmetry conditions. Therefore the domain extension approach has been proposed by Clausen and Andreassen (2017) to circumvent this problem. This method proposes to extend the filter domain and the finite element domain with padding elements around the original domain as shown in Figure 4.6b. The padding elements are not applied around load introductions and supports, where a distance equal to the filter radius is recommended (Clausen and Andreassen 2017).

The density of these padding elements is updated due to filtering, which ensures that the minimum length scale is obeyed. In order to ensure that the final design does not extend into the padding elements an upper limit of 0.5 is applied to the density of these padding elements.

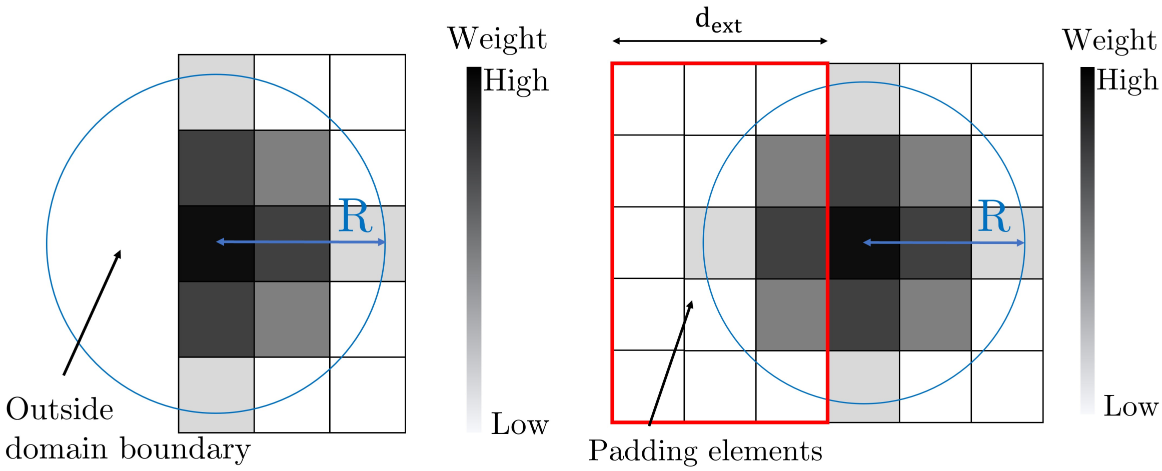


(a) The filter at the boundary of the design domain.

(b) Filter with padding elements placed along the boundary marked with red.

Figure 4.6: Effect of padding on filter size.

## 4.4 Strength based optimization

In many applications the governing property of the structure is not the stiffness but the strength. Therefore the topology optimization can be done with respect to a strength criteria given by the failure index. Failure is typically a local criteria, which is checked for every element. This can be formulated as in Equation 4.14, where $FI_e$ is the failure index in element $e$ and $n_{elem}$ is the number of elements where the failure criteria is evaluated.

$$FI_e - 1 \leq 0, \text{ for } e = 1,2,...,n_{elem} \tag{4.14}$$

In order to calculate the failure index it is necessary to determine a suitable failure criteria. These failure criteria could for example be based on the stress, strain or the strain energy density. If the failure criteria is based on the strain energy density, it will yield the same solution as the stiffness based optimization, since this is also based on the strain energy density (Pedersen 1998). The stiffness based optimization can thus give a good starting point for strength based topology optimization. Throughout this project only stress based failure criteria will be considered.

### 4.4.1 Failure criteria

In many cases the material is assumed to be isotropic and the von Mises failure criteria is used. As described in Section 3 both the Smooth PA and the continuous fiber reinforced material are orthotropic both in strength and stiffness. This failure criterion is thus not suitable.

Therefore another failure criterion has to be used instead. Multiple failure criteria exist for composite materials such as Tsai-Hill, max stress and Tsai-Wu. Furthermore specific failure criteria have been proposed for 3D-printed parts by for example Yao et al. (2020).

Tsai-Wu will be used as the failure criterion throughout this project. This failure criterion is well known and often used in conjunction with optimization. It has furthermore been proven to yield good results for build orientation optimization of FFF 3D-printed parts (Mirzendehdel, Rankouhi, and Suresh 2017). Tsai-Wu is differentiable which makes it possible to implement in gradient based topology optimization. The standard formulation of the Tsai-Wu failure criterion is expressed in Equation 4.15. The element index will be omitted here due to clarity.

$$F_i \sigma_i + F_{ij} \sigma_i \sigma_j \leq 1 \tag{4.15}$$

The stresses can be calculated using Equation 4.5 where the constitutive matrix $[C_e]$ is calculated using Equation 4.7. The definitions of $F_i$ and $F_{ij}$ are given in Equation 4.16 where $X$ and $Y$ are the strength values along the fiber orientation and perpendicular to the fiber orientation respectively. The indices $t$ and $c$ represent tension and compression. $S$ is the shear strength.

$$\begin{aligned} F_1 &= \frac{1}{X_t} - \frac{1}{X_c} & F_{11} &= \frac{1}{X_t X_c} \\ F_2 &= \frac{1}{Y_t} - \frac{1}{Y_c} & F_{22} &= \frac{1}{Y_t Y_c} \\ F_6 &= 0 & F_{66} &= \frac{1}{S^2} \end{aligned} \tag{4.16}$$

The formulation of the Tsai-Wu failure criterion given in Equation 4.15 does not depend linearly on the stress, thus it does not double if the stress is doubled. This can lead to non-optimal designs and thus the strength ratio, $s$, should be used instead (Groenwold and Haftka 2006). The strength ratio is given in Equation 4.17 where $\{\sigma\}$ is the current stress and $\{\sigma^*\}$ is the stress at failure (Kim et al. 1994).

$$\{\sigma^*\} = s\{\sigma\} \tag{4.17}$$

When this relation is inserted in the Tsai-Wu criterion Equation 4.18 is obtained.

$$s^2 F_{ij}\sigma_i\sigma_j + sF_i\sigma_i = 1 \tag{4.18a}$$

$$s^2(F_{11}\sigma_1^2 + F_{22}\sigma_2^2 + F_{66}\sigma_6^2 + 2F_{12}\sigma_1\sigma_2) + s(F_1\sigma_1 + F_2\sigma_2 + F_6\sigma_6) = 1 \tag{4.18b}$$

The resulting equation is a second order polynomial, which can be solved using Equation 4.19a. The parameters $a$, $b$ and $d$ are defined in Equation 4.19b, 4.19c and 4.19d. It yields the Tsai-Wu strength ratio, which is equal to the factor of safety and depends linearly on the load.

$$s = \frac{-b + \sqrt{d}}{2a} \tag{4.19a}$$

$$a = F_{11}\sigma_1^2 + F_{22}\sigma_2^2 + F_{33}\sigma_3^2 + 2F_{12}\sigma_1\sigma_2 \tag{4.19b}$$

$$b = F_1\sigma_1 + F_2\sigma_2 \tag{4.19c}$$

$$d = b^2 + 4a \tag{4.19d}$$

Since $s$ represents the factor of safety the failure index can be calculated using Equation 4.20.

$$FI = \frac{1}{s} \tag{4.20}$$

The Tsai-Wu failure index is calculated in each element. When doing strength based optimization, this will result in a constraint for each element, which makes it very inefficient to solve the problem.

### 4.4.2 Relaxation of failure index

The above method for calculating failure indices does not take into account that some elements have intermediate densities, due to the formulation of the topology optimization problem. In order to determine the failure indices at the intermediate densities, the results should be interpolated. Typically this interpolation is done on the stresses as seen in for example Duysinx and Bendsøe (1998) and Bruggi (2008) using isotropic von Mises failure criteria. This approach has been applied to relax failure indices instead as done by for example Lund (2018). In order to retain generality, the methods will be explained based on failure indices. It will yield the same result no matter if the failure indices or the stresses are relaxed, when the failure index depends linearly on the stresses as it does for the Tsai-Wu criteria.

There are some requirements for the interpolation functions, which are that the failure index should be 0 when the density is 0 and it should be equal to the failure index in the solid material, when the density is 1. Furthermore the intermediate densities should be penalized in order to avoid them in the final solution.
This can be done by utilizing the formulation given in Equation 4.21, where $FI_{rel,e}$ is the relaxed failure index, $FI_e$ is the unrelaxed failure index and $x_e$ is the element density, which is relaxed by the factor $q$. This factor should be equal to the stiffness penalization factor $p$ for physical consistency (Duysinx and Bendsøe 1998).

$$FI_{rel,e} = \frac{FI_e}{x_e^q} \leq 1 \tag{4.21}$$

This formulation has the problem that it is not defined at $x_e = 0$, where it should be 0. It can thus be reformulated into Equation 4.22 when $q = p$.

$$x_e(FI_{rel,e} - 1) = x_e(FI_e - x_e^p) \leq 0 \tag{4.22}$$

The problem although still contains a singularity at $x_e = 0$ and thus to circumvent this problem Cheng and Guo (1997) proposed to relax the problem as given in Equation 4.23. Here the variable $\varepsilon$ is decreased using a continuation approach, thus when $\varepsilon \to 0$ the relaxed design space approaches the original design space. This approach is named the $\varepsilon$-approach.

$$x_e(FI_e - x_e^p) \leq \varepsilon \tag{4.23}$$

A more recent approach has been proposed by Bruggi (2008). When utilizing this approach $q < p$. Equation 4.21 can thus be rewritten as shown in Equation 4.24.

$$FI_e - x_e^q \leq 0 \tag{4.24a}$$

$$FI_e - x_e^q - x_e^p \leq -x_e^p \tag{4.24b}$$

$$FI_e - x_e^p \leq x_e^q - x_e^p \tag{4.24c}$$

$$x_e(FI_e - x_e^p) \leq x_e(x_e^q - x_e^p) \tag{4.24d}$$

It is seen that the left hand side of Equation 4.24d is the same as the left hand side in the $\varepsilon$-approach given in Equation 4.23. The qp-approach is thus a special case of the $\varepsilon$-approach where $\varepsilon$ is given in Equation 4.25.

$$\varepsilon = x_e(x_e^q - x_e^p) \tag{4.25}$$

When $x_e = 0$ or $x_e = 1$ the qp-approach gives the same result as the $\varepsilon$-approach with $\varepsilon = 0$. When utilizing the qp-approach the relaxation is thus higher at the intermediate densities while the relaxation decreases when approaching the extreme densities. The solution will typically approach the extreme densities when converging and thus the relaxation will be decreased when converging towards the final solution. The qp-approach will thus be used to relax the failure indices throughout this project.

The relaxed failure index has been rewritten slightly in order to simplify the calculations. The relaxed failure indices depend on the densities both directly and through the stresses. Since the failure indices depend linearly on the stresses the penalized densities can be multiplied on the failure indices instead of the stresses. The failure index is thus given as Equation 4.26.

$$FI_{rel,e} = \frac{x_e^p}{x_e^q} FI_{e0} = x_e^{p-q} FI_{e0} \tag{4.26}$$

Here $FI_{e0}$ is the failure index in the solid material calculated based on the stresses in the solid material given by Equation 4.27. $[C_0]$ is the constitutive matrix of the solid material.

$$\{\sigma_e\} = [C_0][B]\{u_{elem}\} \tag{4.27}$$

### 4.4.3 Aggregate function

When the failure is evaluated in every element a constraint is added for each element, which makes the optimization problem inherently difficult to solve. A way to overcome the problem with a large number of constraints on the failure indices is by introducing an aggregate function. This type of function allows to combine the local constraints into a single global constraint. This could be accomplished by using the maximum failure index, but this will be non differentiable, and in order to implement it in gradient based optimization, the constraint has to be differentiable. This problem can be circumvented by using the P-norm aggregate function to estimate the maximum value. The P-norm function is given in Equation 4.28.

$$FI_{PN} = \left( \sum_{e=1}^{n_{elem}} FI_{rel,e}^P \right)^{1/P} \tag{4.28}$$

The P-norm function penalizes the values with the factor $P$ to weigh the larger constraint values higher. It can thus be used to estimate the maximum value of the failure indices. The

penalization value $P$ can be changed to penalize more or less. The higher the value of $P$ the closer the result is to the maximum value, but this will also make the function more nonlinear and thereby the optimization problem becomes more difficult to solve.
This formulation will typically overestimate the maximum value. In order to improve the accuracy a regional aggregate function can be used. The idea is to divide the structure into multiple regions, in which the maximum failure index is approximated by the P-norm formulation. This increases the number of constraints, but it gives more accurate results as well. (Le et al. 2010)

### 4.4.4 Adaptive constraint scaling

Another way to improve the accuracy of the approximation of the maximum failure index, is by using the adaptive constraint scaling method. This method was proposed by Le et al. (2010), in order to scale the global stress measure to better match the maximum value, as seen in Equation 4.29.

$$FI_{max} \approx cFI_{PN} \tag{4.29}$$

The idea behind this formulation is to multiply the P-norm with a constant $c$ in order to obtain the maximum failure index $FI_{max}$. $c$ is calculated using Equation 4.30, where $I$ indicates the iteration number. The constraint scaling factor can thus be calculated based on historical information from the last iterations.

$$c^I = \alpha^I \frac{FI_{max}^{I-1}}{FI_{PN}^{I-1}} + (1-\alpha^I)c^{I-1} \tag{4.30}$$

$\alpha$ is introduced in order to avoid oscillation between solutions. In order to determine if oscillation has occurred Equation 4.31 is used. For the first two iterations $\alpha = 1$ is used.

$$osc = \frac{\sigma_{PN}^{I-2} - \sigma_{PN}^{I-1}}{\sigma_{PN}^{I-1} - \sigma_{PN}^{I}} \tag{4.31}$$

$\alpha$ is calculated usingEquation 4.32 as proposed by Oest and Lund (2017).

$$\alpha^I = \begin{cases} \min(1,\alpha^{I-1} \cdot 1.2), & \text{if } osc \leq 0 \\ \max(0.5,\alpha^{I-1} \cdot 0.8), & \text{if } osc > 0 \end{cases} \tag{4.32}$$

## 4.5 Fiber angle optimization

As stated in the problem formulation the goal of the project is to combine topology optimization with fiber orientation optimization, in order to get the optimal dispersion of the materials to reach high strength 3D-printed parts. There are many methods that can be used for fiber angle optimization. Some of these methods will be described throughout this section, where pros and cons will be discussed. The methods will be rated based on multiple criteria including how good the solutions are and the level of post processing needed to get a result, which can be manufactured. Post processing is defined as the amount of change that needs to be applied to the results of the optimization, in order to get a result that can be manufactured. The best method will be selected and implemented.

### 4.5.1 Contour fiber placement

When slicing a geometry the placement of the fibers will typically follow the contour of the geometry as shown in Figure 4.7. The Contour Fiber Placement (CFP) methods mimic this behavior in order to generate the fiber paths. It is thus easy to manufacture the optimized geometry since no post processing is needed.

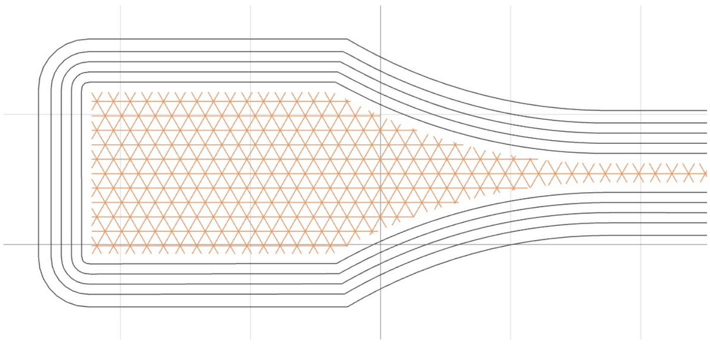

Figure 4.7: Fiber placement. The black lines illustrate the fiber path along the contour, and the orange grid is the infill.

Methods for doing these kinds of fiber paths could be the offset method, equally spaced method, see Papapetrou, Patel, and Tamijani (2020) or Hybrid deposition path pattern, see Xu, Huang, et al. (2020). These methods all place the fibers along the contour of the geometry, but have different formulations.
By placing the fibers along the contour no optimization is carried out on the fiber orientation, thus other better solutions might exist. Another downside is that these methods do not have a good way to accommodate acute angles (Papapetrou, Patel, and Tamijani 2020). These sharp corners cannot be printed due to the minimum possible radius of the fiber.
The benefit is that no post processing is needed, because the design generated can be put directly into the slicer. Placing the fibers on the outer contour, will give a high bending stiffness and strength, which is a common load scenario. The method can therefore yield good results for common use cases.

### 4.5.2 Continuous fiber angle optimization

Continuous Fiber Angle Optimization (CFAO) can be combined with gradient based topology optimization, to combine material directions with density based optimization. This method has for example been used by Hoglund (2016), Jiang, Hoglund, and Smith (2019), Fedulov et al. (2021) and Nomura et al. (2014) for solving stiffness based problems. The CFAO method requires a fiber angle variable applied to each element, which indicates the orientation of the material. Each finite element will therefore have two design variables, one density variable, that controls the amount of material in the element and one for the material angle as shown in Figure 4.8.

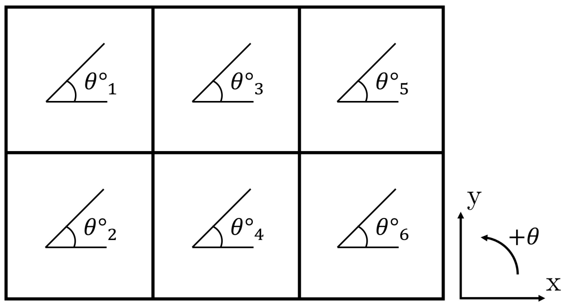


Figure 4.8: CFAO with fiber angle illustrated on each element.

The angle will be added as a rotation of the constitutive matrix as in Equation 4.33, where $[T]$ is the transformation matrix. The rotation is defined from the global to the local coordinate system.

$$[C(\theta_e)] = [T(\theta_e)]^{-1}[C_0][T(\theta_e)]^{-T} \tag{4.33}$$

The downside to this method is that it tends to get stuck in a weak local minimum and it can thus be difficult to reach a strong local minimum Hoglund (2016). Another downside to this method is the need for post processing. The fiber angles are computed for each element and are therefore not continuous. Filters can be applied in order to improve the continuity but post processing is still necessary to define the exact fiber paths. This post processing is manual and requires engineering judgment in order to determine how the results should be interpreted, due to manufacturing restrictions (Fedulov et al. 2021). These restrictions are the minimum fiber length, minimum fiber bending radius and the width of the reinforced filament strand. These post processing steps result in a non-optimal fiber angle distribution. In many occasions the fiber orientation will follow the contour and thus it can be implemented relatively easy, but this cannot always be guaranteed.

### 4.5.3 Free material optimization

The Free Material Optimization (FMO) introduced by Ringertz (1993) and Bendsøe, Guedes, et al. (1994), can also be used to optimize with respect to the material orientation. This method uses the entrances in the elastic stiffness tensor as the design variables for the optimization. The constraints for this method are based on the stiffness tensor being physical and attainable. The constraints are therefore for the stiffness tensor to be symmetric and positive semidefinite (Weldeyesus and Stolpe 2016).
FMO problems are in general computationally demanding problems due to the large number of design variables (Weldeyesus 2014). Furthermore it involves a lot of post processing since the resulting stiffness tensor has to be translated into one or multiple stacked layers of different fiber orientations in order to obtain the correct properties. The benefit of this method is that is has a large feasible design space and thus it can yield better results.

### 4.5.4 Discrete material optimization

The Discrete Material Optimization (DMO) method, can also be used to optimize with respect to the fiber orientations. This method was first introduced in Stegmann and Lund (2005), and is based on the method of multi material topology optimization from Sigmund and Torquato (1997).
This method takes offset in multi material optimization as described in Section 4.2.2. A pool of possible candidate fiber angles are defined on beforehand and these are treated as different materials in multi material topology optimization. Due to this formulation multiple materials can be implemented easily as well.
The constitutive matrix of the material in a given element is calculated as a weighted sum of the candidate materials, as given in Equation 4.34a. The number of materials is $n_{mat}$. The weight function for a given element $e$ and material $c$ is denoted $w_{k,ec}$ and the material constitutive matrix is $[C_c]$ for material $c$. The element constitutive matrix is denoted $[C_e]$.
The weights must be between 0 and 1 as given in Equation 4.34b in order to be physically meaningful and the sum of the weights must comply with the constraint given in Equation 4.34c. In the original formulation by Stegmann and Lund (2005) the weights must sum to unity since it was developed for fiber angle optimization and not for topology optimization. The original equality constraint was changed to an inequality constraint by Hvejsel and Lund (2011), in order to apply simultaneous topology and fiber angle optimization.

$$[C_e] = \sum_{c=1}^{n_{mat}} w_{k,ec}[C_c] = w_{k,e1}[C_1] + w_{k,e2}[C_2] + .... + w_{k,en_{mat}}[C_{n_{mat}}] \tag{4.34a}$$

$$\sum_{c=1}^{n_{mat}} w_{k,ec} \leq 1 \tag{4.34b}$$

$$0 \leq w_{k,ec} \leq 1 \tag{4.34c}$$

### 4.5.5 Choice of optimization method

An overview of the pros and cons of the different methods can be found in Table 4.1.

| Methods | Pros | Cons |
|---|---|---|
| CFP | No post processing<br>Easy implementation | No optimum<br>Acute angles |
| CFAO | Few design variables<br>No angle restrictions | Risk of local minimum<br>Post processing |
| FMO | Large design space | High post processing<br>Many design variables |
| DMO | Reduced risk of local minima<br>No post processing | Angle restrictions<br>Many design variables<br>Many constraints |

Table 4.1: Pros and cons of different schemes.

The DMO optimization will be used as the method for combining topology optimization and fiber orientation optimization throughout this project. The main reason for choosing this method is the amount of post processing of the results which is necessary. The results from the optimization can be input directly to the slicer by using masks, which can define the orientation of the infill. The amount of post processing needed in order to 3D-print the structure is therefore minimal, making the DMO favorable.
Compared to the CFAO the DMO requires less post processing, but the CFAO can give better results since the design space is larger. This is due to the limited number of candidate angles available in the DMO. This will only be an advantage of the CFAO if a strong local minimum is reached, but this can not be guaranteed. An advantage of the CFAO is that the orientations are more continuous after post processing, since the results from the DMO will be discontinuous between the different fiber orientations. Since the topic of this project is the combination of 3D-printing and optimization the post processing is weighted higher. The CFP methods would be even better at minimizing post processing, but it reduces the design space and the solution obtained by the DMO can thus be better.

### 4.5.6 Implementation of DMO

In order for the DMO to be effective a proper weight function must be chosen, which satisfies the constraints given in Equation 4.34b and 4.34c. Furthermore it should penalize the intermediate densities in order to obtain a 0-1 design. The weight function for the stiffness interpolation, which will be used is the SIMP formulation which is given in Equation 4.35. In this equation the index $e$ denotes the element number while $c$ denotes the material.

$$w_{k,ec} = x_{ec}^{p} \tag{4.35}$$

Instead of applying this weight factor to the constitutive matrix it is multiplied by the element stiffness matrix as given in Equation 4.36. Here $[k_c]$ is the element stiffness matrix, when material $c$ is used.

$$[k_e] = \sum_{c=1}^{n_{mat}} w_{k,ec}[k_c] \tag{4.36}$$

Another way to formulate the weight function is by using the RAMP formulation introduced by Stolpe and Svanberg (2001). The advantage of the RAMP formulation is that the gradient always has a finite value. This is only the case if $p \geq 1$ for the SIMP formulation. If $p < 1$ the gradient will go towards infinity, when the density approaches 0. Since the stiffness penalization is typically larger than 1 this is not a problem.

In addition to the interpolation of the stiffness the failure index has to be interpolated at the intermediate densities. This can be done by interpolating the failure indices as described in Section 4.4.2. The relaxed failure index is given in Equation 4.37a, with the weight function given in Equation 4.37b. In order to penalize the intermediate densities $p-q < 1$ and thus the gradient will go towards infinity when the density approaches 0. Therefore a lower boundary of $10^{-3}$ has been set.

$$FI_{rel,e} = \sum_{c=1}^{n_{mat}} w_{FI,ec} FI_{ec} \tag{4.37a}$$

$$w_{FI,ec} = x_{ec}^{p-q} \tag{4.37b}$$

The failure index is denoted as $FI_{ec}$, where it is a weighted sum over the number of materials $n_{mat}$. The element densities of material $c$ are denoted as $x_{ec}$, where the stiffness penalization is $p$ and the failure index relaxation is $q$.

Due to these formulations of the weight functions the constraints on the weight functions given in Equation 4.34b and 4.34c are fulfilled, when the constraints in Equation 4.38 are fulfilled. The original formulation of the constraints is nonlinear with respect to the design variable, while the new formulation is linear with respect to the design variables.

$$\sum_{c=1}^{n_{mat}} x_{ec} \leq 1 \tag{4.38a}$$

$$0 \leq x_{ec} \leq 1 \tag{4.38b}$$

In order to establish a minimum length scale, filters can be applied as in traditional topology optimization as described in Section 4.3. These filters are applied for each material separately. When applying the filters the constraints given in Equation 4.38 are applied to the filtered densities instead of the design variables. This is problematic since it is more difficult to solve when the threshold projection filter is applied, due to the non-linearity of the constraint (Sørensen and Lund 2015).
Due to the linearity of the density filter it makes no difference if the constraints are applied to the design variables or the filtered densities for the density filter and thus this is an effective way to to apply the constraints. The threshold projection filter on the other hand is nonlinear and thus if the constraints are given based on the design variables it could lead to $\sum_{c=1}^{n_{mat}} x_{ec} > 1$. Thereby the original constraint on the sum of the weights given in Equation 4.34b is not satisfied and a nonphysical superior material is created. To circumvent this problem a normalization filter was proposed by Sørensen and Lund (2015), but this normalization only works for pure fiber angle optimization problems and not when it is combined with topology optimization. The threshold filter has thus only been used with $\eta = 0.5$ in order to circumvent the problem.

To sum up all the above the P-norm approximation of the maximum failure index will be calculated as specified in Figure 4.9. This gives an overview of the calculation of the strength constraint. It takes the filtered densities as input and the output is the P-norm approximation of the maximum failure index.

| Pseudo code | Reference |
|---|---|
| Stiffness weight function | See Equation 4.35 |
| Element stiffness matrix | See Equation 4.36 |
| Assemble global stiffness matrix | See Section 4.1 |
| Calculate displacements | See Equation 4.1 |
| Calculate stresses | See Equation 4.27 |
| Rotate stresses | See Equation 4.6 |
| Calculate failure indices | See Section 4.4.1 |
| Failure index weight function | See Equation 4.37b |
| Relaxed failure indices | See Equation 4.37a |
| P-norm approximation of max failure index | See Equation 4.28 |
| Adaptive constraint scaling | See Section 4.4.4 |

Figure 4.9: Pseudo code for calculation of P-norm approximation of the maximum failure index.

## 4.6 Design sensitivity analysis

In order to perform gradient based optimization the sensitivities are needed. This can be done either analytically or by using finite difference. The finite difference formulation is computationally inefficient thus the analytical formulation will be used and is described. It has though been validated against finite difference.
In order to calculate the analytical expressions the adjoint method will be used since it is an effective way to calculate the sensitivities, when considering problems with many design variables and few constraints. The sensitivities could also be calculated using direct differentiation, but this will be computationally inefficient as will be clear from the below description of the adjoint method. The sensitivities will be derived for both the compliance and the strength based problem.
The sensitivities derived in this section are derived for the case were no filters are applied. In order to take the effects of the filters into account the obtained sensitivities must be multiplied by the sensitivity of the filter as described at the end of Section 4.6.4.

### 4.6.1 Adjoint method

The stress and compliance functions can be written as a function of the density both directly and indirectly through the nodal displacements as $f\left(\{x\},\{U(\{x\})\}\right)$. The original function $f$ can be augmented using the Lagrange multiplier method to get the augmented function $\tilde{f}$ as given in Equation 4.39. The Lagrange multipliers $\{\lambda\}$ can be chosen arbitrarily since $[K]\{U\}-\{F\}=\{0\}$ due to the equilibrium condition. $[K]$ is the global stiffness matrix, $\{U\}$ is the displacement vector and $\{F\}$ is the force vector.

$$\tilde{f} = f - \{\lambda\}^T\left([K]\{U\}-\{F\}\right) \tag{4.39}$$

The gradient can be determined using the chain rule as given in Equation 4.40. The force and Lagrange multipliers are assumed to be independent of the design variables $x_{ec}$ for a given element $e$ and material $c$.

$$\begin{aligned}\frac{d\tilde{f}}{dx_{ec}} =& \frac{\partial f}{\partial x_{ec}} + \frac{\partial f}{\partial\{U\}}\frac{\partial\{U\}}{\partial x_{ec}} - \{\lambda\}^T\left(\frac{\partial[K]}{\partial x_{ec}}\{U\}+[K]\frac{\partial\{U\}}{\partial x_{ec}}\right) && \text{(4.40a)}\\ =& \frac{\partial f}{\partial x_{ec}} - \{\lambda\}^T\frac{\partial[K]}{\partial x_{ec}}\{U\} + \left(\frac{\partial f}{\partial\{U\}} - \{\lambda\}^T[K]\right)\frac{\partial\{U\}}{\partial x_{ec}} && \text{(4.40b)}\end{aligned}$$

Since the Lagrange multipliers can be chosen arbitrarily they are chosen such that Equation 4.41a is satisfied. This is a set of linear equations, which can be rewritten into Equation 4.41b due to symmetry of the stiffness matrix. This equation can be efficiently solved for $\{\lambda\}$ especially if the factored stiffness matrix $[K]$ is reused between iterations.

$$\frac{\partial f}{\partial \{U\}} - \{\lambda\}^T [K] = \{0\}^T \tag{4.41a}$$

$$\left( \frac{\partial f}{\partial \{U\}} \right)^T = [K]\{\lambda\} \tag{4.41b}$$

Hereby the total derivative reduces to Equation 4.42. It can be seen that the derivative of the displacements cancels out. This is important since it is computationally expensive to compute when many design variables exist. Instead the linear system of equations given in Equation 4.41b has to be solved once instead for each constraint function. Therefore this formulation is only efficient for few constraints. If direct differentiation had been used instead the derivative of the displacements with respect to the densities should be calculated, but then it would not be necessary to solve Equation 4.41b. Therefore that method is good if many constraints exists but only a few design variables.

$$\frac{d\tilde{f}}{dx_{ec}} = \frac{df}{dx_{ec}} = \frac{\partial f}{\partial x_{ec}} - \{\lambda\}^T \frac{\partial [K]}{\partial x_{ec}} \{U\} \tag{4.42}$$

### 4.6.2 Sensitivity of compliance

The derivative of the compliance $C$, is obtained by using the adjoint method as described above. First the Lagrangian multipliers are determined by solving the system of linear equations given in Equation 4.43a. The function $f$ in Equation 4.41b is here the compliance $C$ as given in Equation 4.8. When this is differentiated Equation 4.43b is obtained. The step from Equation 4.43b to 4.43c is possible due to the symmetry of the stiffness matrix.

$$\frac{\partial C}{\partial \{U\}} = \{\lambda\}^T [K] \tag{4.43a}$$

$$([K]\{U\})^T + \{U\}^T [K] = \{\lambda\}^T [K] \tag{4.43b}$$

$$2\{U\}^T [K] = \{\lambda\}^T [K] \tag{4.43c}$$

$$2\{U\}^T = \{\lambda\}^T \tag{4.43d}$$

The results from Equation 4.43d can be inserted into the expression for the total derivative given in Equation 4.42. This yields the expression given in Equation 4.44.

$$\frac{dC}{dx_{ec}} = \{U\}^T \frac{\partial [K]}{\partial x_{ec}} \{U\} - 2\{U\}^T \frac{\partial [K]}{\partial x_{ec}} \{U\} \tag{4.44a}$$

$$\frac{dC}{dx_{ec}} = -\{U\}^T \frac{\partial [K]}{\partial x_{ec}} \{U\} \tag{4.44b}$$

### 4.6.3 Sensitivity of strength function

The sensitivity of the strength function is also calculated using the adjoint method. First the Lagrange multipliers are calculated using Equation 4.41b where the partial derivative is given in Equation 4.45 utilizing the chain rule. The function $f$ to which the gradient is calculated is the aggregate approximation of the maximum failure index with the constraint scaling applied given as $FI_{PN}$. The P-norm of the failure index is denoted $FI_{PN}$. The relaxed failure index for element $e$ is denoted $FI_{rel,e}$ and the element failure index for candidate material $c$ is denoted $FI_{ec}$. The stresses in the global and material coordinate systems are denoted as $\{\sigma_{glo}\}$ and $\{\sigma_{mat}\}$ respectively.

$$\frac{\partial f}{\partial \{U\}} = c \sum_{e=1}^{n_{elem}} \frac{\partial FI_{PN}}{\partial FI_{rel,e}} \sum_{c=1}^{n_{mat}} \frac{\partial FI_{rel,e}}{\partial FI_{ec}} \frac{\partial FI_{ec}}{\partial \{\sigma_{mat,ec}\}} \frac{\partial \{\sigma_{mat,ec}\}}{\partial \{\sigma_{glo,ec}\}} \frac{\partial \{\sigma_{glo,ec}\}}{\partial \{U\}} \tag{4.45}$$

These partial derivatives will be explained and determined in Section 4.6.4. Furthermore the partial derivative of the P-norm aggregate function with respect to the design variables must be determined using Equation 4.46. The weight function for the failure index of element $e$ and material $c$ is denoted $w_{FI,ec}$.

$$\frac{\partial f}{\partial x_{ec}} = \frac{\partial FI_{PN}}{\partial FI_{rel,e}} \frac{\partial FI_{rel,e}}{\partial w_{FI,ec}} \frac{\partial w_{FI,ec}}{\partial x_{ec}} \tag{4.46}$$

The results are inserted in Equation 4.42, which yields the total derivative of the aggregate function with respect to the design variables.

### 4.6.4 Explicit definitions of individual terms

In the following the individual partial derivatives are given explicitly. It should be noted that the sensitivities are given for a single element, material or both. It is computationally inefficient to implement this directly into MATLAB, but due to clarity these expressions are given here while the vectorized version is implemented.

**Derivative of P-norm of failure indices with respect to relaxed failure indices**

The P-norm aggregate function of the failure indices is given in Equation 4.28. The derivative of the P-norm with respect to the relaxed failure indices is given in Equation 4.47. The value of $i$ represents a running index over the elements.

$$\frac{\partial FI_{PN}}{\partial FI_{rel,e}} = \left( \sum_{i=1}^{n_{elem}} FI_{rel,i} \right)^{\frac{1}{P}-1} FI_{rel,e}^{P-1} \tag{4.47}$$

**Derivative of relaxed failure indices with respect to failure index weight function**

The relaxed failure index is given in Equation 4.37a. The derivative of the relaxed failure index with respect to the weight function is given in Equation 4.48.

$$\frac{\partial FI_{rel,e}}{\partial w_{FI,ec}} = FI_{ec} \tag{4.48}$$

**Derivative of failure index weight function with respect to filtered density**

The failure index weight function is given in Equation 4.37b. The derivative of the weight function for the failure index with respect to the density is given in Equation 4.49.

$$\frac{\partial w_{FI,ec}}{\partial x_{ec}} = (p-q)x_{ec}^{p-q-1} \tag{4.49}$$

**Derivative of relaxed failure indices with respect to elemental failure indices**

The relaxed failure index is given in Equation 4.37a. The derivative of the relaxed failure index with respect to the failure index for a given element and material is given in Equation 4.50.

$$\frac{\partial FI_{rel,e}}{\partial FI_{ec}} = w_{FI,ec} \tag{4.50}$$

**Derivative of elemental failure indices with respect to stresses in the material coordinate system**

The elemental failure index is given in Equation 4.20. The failure indices are calculated based on the Tsai-Wu strength ratio as described in Section 4.4.1. The chain rule is used to calculate the gradient as given in Equation 4.51. The parameters $a$, $b$, $d$ and $s$ are given in Equation 4.19b, 4.19c, 4.19d and 4.19a respectively. All the indices $e$ and $c$ are removed for clarity.

$$\frac{\partial FI}{\partial \{\sigma_{mat}\}} = \frac{\partial FI}{\partial s}\left(\frac{\partial s}{\partial a}\frac{\partial a}{\partial \{\sigma_{mat}\}} + \frac{\partial s}{\partial b}\frac{\partial b}{\partial \{\sigma_{mat}\}} + \frac{\partial s}{\partial d}\left(\frac{\partial d}{\partial a}\frac{\partial a}{\partial \{\sigma_{mat}\}} + \frac{\partial d}{\partial b}\frac{\partial b}{\partial \{\sigma_{mat}\}}\right)\right) \tag{4.51}$$

The individual terms are given in Equation 4.52, where the coefficients $F$ are the strength parameters from the Tsai-Wu criteria given in Equation 4.16.

$$\frac{\partial FI}{\partial s} = -\ s^{-2} \tag{4.52a}$$

$$\frac{\partial s}{\partial a} = \frac{-b+\sqrt{d}}{-2a^2} \tag{4.52b}$$

$$\frac{\partial s}{\partial b} = \frac{-1}{2a} \tag{4.52c}$$

$$\frac{\partial s}{\partial d} = \frac{1}{4a\sqrt{d}} \tag{4.52d}$$

$$\frac{\partial d}{\partial a} = 4 \tag{4.52e}$$

$$\frac{\partial d}{\partial b} = 2b \tag{4.52f}$$

$$\frac{\partial a}{\partial \{\sigma_{mat}\}} = [2F_{12}\sigma_2 + 2F_{11}\sigma_1, 2F_{12}\sigma_1 + 2F_{22}\sigma_2, 2F_{66}\sigma_6] \tag{4.52g}$$

$$\frac{\partial b}{\partial \{\sigma_{mat}\}} = [F_1, F_2, 0] \tag{4.52h}$$

**Derivative of stresses in the material coordinate system with respect to the stresses in the global coordinate system**

The stresses in the material coordinate system are given in Equation 4.6. The derivative of the global stresses with respect to the stresses in the local material coordinate system are given in Equation 4.53 as the transformation matrix $[T]$ for candidate material $c$.

$$\frac{\partial \{\sigma_{mat,ec}\}}{\partial \{\sigma_{glo,ec}\}} = [T_c] \tag{4.53}$$

**Derivative of stresses in the global coordinate system with respect to nodal displacements**

The stresses in the global coordinate system are given in Equation 4.5. The derivative of the global stresses with respect to the element displacements is given in Equation 4.54. The strain-displacement matrix is calculated in the element center since this is the position where the stresses are calculated as described in Section 4.1.

$$\frac{\partial \{\sigma_{glo,ec}\}}{\partial \{u_e\}} = [C_c][B_e] \tag{4.54}$$

**Derivative of the element stiffness matrix with respect to the density**

The stiffness matrix in given in Equation 4.4. The sensitivity of the stiffness matrix is calculated using Equation 4.55. The strain displacement matrix is dependent upon the position of the Gauss points ($x_i$,$y_j$) as described in Section 4.1. The weight factor for the Gauss integration $w_{G,ij}$ is 1 for all the 2x2 Gauss points for the bilinear element formulation.

$$\frac{\partial [k_e]}{\partial x_{ec}} = p x_{ec}^{p-1} \sum_{i=1}^{2} \sum_{j=1}^{2} w_{G,ij} [B(x_i,y_j)]^T [C_c][B(x_i,y_j)] t = p x_{ec}^{p-1} [k_c] \tag{4.55}$$

**Derivative of the filters**

The filters are given in Equation 4.11 and 4.12. The sensitivities of the threshold filter can be calculated using the chain rule given in Equation 4.56.

$$\frac{d\bar{\bar{x}}_{ec}}{dx_{ec}} = \sum_{i=1}^{n_{elem}} \frac{\partial \bar{\bar{x}}_{ec}}{\partial \bar{x}_i} \frac{\partial \bar{x}_i}{\partial x_{ec}} \tag{4.56}$$

The individual terms are given in Equation 4.57. $\bar{x}_i$ is the filtered density from the density filter.

$$\frac{d\bar{\bar{x}}_{ec}}{d\bar{x}_i} = \frac{\beta \cdot \text{sech}^2(\beta(\bar{x}_i - \eta))}{\tanh(\beta\eta) + \tanh(\beta(1-\eta))} \tag{4.57a}$$

$$\frac{d\bar{x}_i}{dx_{ec}} = \frac{H_{ei}}{\sum_{j=1}^{n_{elem}} H_{ej}} \tag{4.57b}$$

If the density filter is applied without the threshold projection the sensitivity is given by Equation 4.57b.

# 5 Numerical investigation of optimization problem

During this chapter the definition of the optimization problem will be investigated. This is necessary since issues are encountered using the implementation from Section 4 of the optimization problem. These issues prevent the optimizer from reaching a discrete solution, which satisfies the constraint on the failure index. Different solutions will be examined and discussed in order to circumvent this problem and get a physical and discrete solution.

## 5.1 Optimization problem

The optimization problem that will be solved is a minimization problem of the total volume of the design domain. The objective function is thus a sum of all element volumes $V_e$, which depends upon the element densities $x_{ec}$ for a given candidate material $c$.
The objective function is subjected to a constraint on the maximum failure index, which is approximated using the P-norm aggregate function with adaptive constraint scaling. The P-norm is calculated as described in Figure 4.9. In order to achieve a physical result, the total element density cannot be larger than one as given in Equation 5.1c. Furthermore a non-zero lower bound is set since a density of 0 would result in infinite gradients and possibly a singular stiffness matrix.

$$\underset{\{x\}}{\text{minimize}} \quad f(\{x\}) = \sum_{c=1}^{n_{mat}} \sum_{e=1}^{n_{elem}} V_e x_{ec} \tag{5.1a}$$

$$\text{subject to} \quad g_0(\{x\}) = c \cdot FI_{PN} - 1 \leq 0 \tag{5.1b}$$

$$g_e(\{x\}) = \sum_{c=1}^{n_{mat}} x_{ec} \leq 1, \text{ for } e = 1, 2, ..., n_{elem} \tag{5.1c}$$

$$10^{-3} \leq x_{ec} \leq 1, \text{ for } e = 1, 2, ..., n_{elem} \text{ and } c = 1, 2, ..., n_{mat} \tag{5.1d}$$

The MBB-beam as shown in Figure 5.1 will be used as the benchmark problem, where the blue elements are the active domain and the black elements have a density of 1 for the material in the 0° direction. The settings are given in Table 5.1.

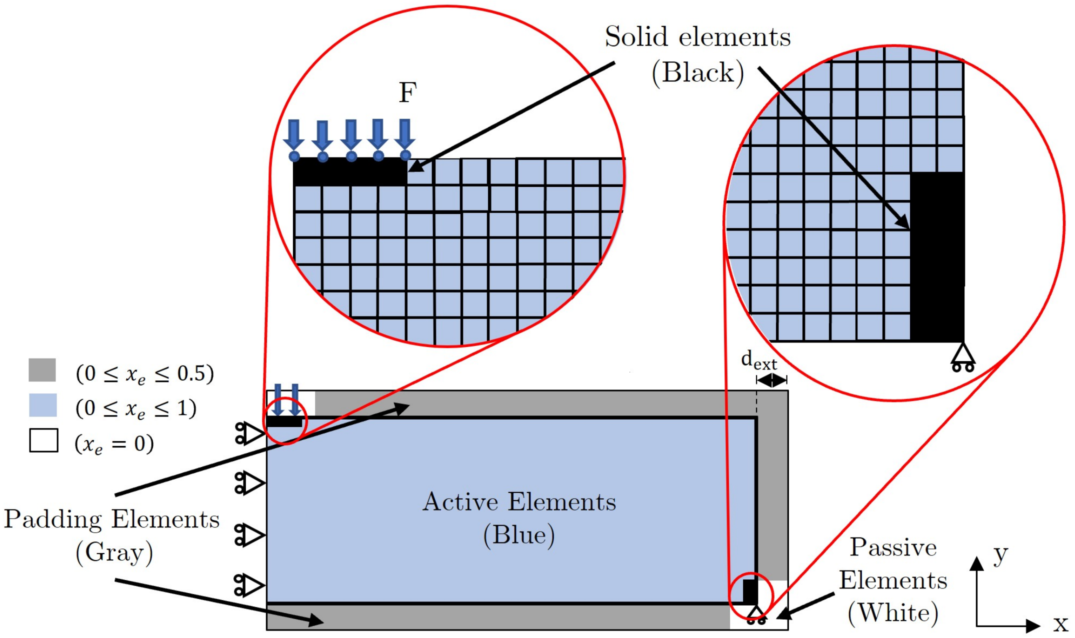


Figure 5.1: Setup of the MBB-beam used for testing the optimization algorithms.

| | | |
|---|---|---|
| Domain size | | 150x50 bilinear elements |
| Domain extension | $d_{ext}$ | 6 elements |
| Material | | Smooth PA |
| Possible directions | | [0°; 90°; 45°; −45°] |
| Filter | | Density |
| Force | $F$ | 500 N |
| P-norm aggregation factor | $P$ | 8 |
| Stiffness penalization factor | $p$ | 3 |
| Failure index relaxation factor | $q$ | 2.5 |
| Constant move limits | $\Delta_{con,ec}$ | 0.025 |
| Filter radius | $R$ | 1.2 mm (3 elements) |
| Iterations | | 1500 |

Table 5.1: Settings for the test problem.

### 5.1.1 Solver

An optimization problem can be solved by using different algorithms. The correct choice of algorithm is important both for speed considerations but also in order to ensure that a strong local minimum is reached for non convex problems. A description of different types of algorithms can be found in Appendix B, where the above problem is solved for compliance minimization in order to determine a suitable algorithm and formulation of the density con-

straints given in Equation 5.1c.
The two algorithms that are compared are the method of moving asymptotes (MMA) and sequential linear programming (SLP). The MMA algorithm is commonly used in topology optimization because it is very good at handling many design variables, but it has limitations, when it comes to the number of constraints it can handle without decreasing the speed significantly. The SLP algorithm is able to handle more constraints, but problems can arise if the initial design does not satisfy the constraints. The result from this investigation seen in Appendix B is to use the SLP algorithm due to its superior handling of many constraints.

The implementation of the SLP problem is based on the MATLAB function linprog, which solves linear programming problems. Since the starting point in most cases does not satisfy the constraints the linear subproblem might not have a feasible solution. In order to circumvent this problem the interior-point-legacy algorithm from the MATLAB linprog function, can be used since it can handle infeasible solutions. For the problem considered here the interior-point-legacy algorithm cannot always converge to a feasible solution thus it is not suitable.
Another approach is to introduce a merit function as in the MMA (Svanberg 1987). The implementation used here is given in Equation 5.2 where $y_i$ denotes the merit function variable for constraint $i$. Since it is penalized hard in the objective function it will typically be 0 at the optimal solution if possible. This idea of using a merit function to relax the problem for SLP has also been implemented by Sørensen, Sørensen, and Lund (2014).

$$\bar{f}(\{x\},\{y\}) = f(\{x\}) + \sum_{i=0}^{n_{elem}} 10^5 y_i \tag{5.2a}$$

$$\bar{g}_i(\{x\},y_i) = g_i(\{x\}) - y_i \leq 1, \text{ for } i = 0,1,...,n_{elem} \tag{5.2b}$$

The linear approximation is only valid around the linearization point, thus constant move limits are applied to ensure sufficient accuracy of the approximation. Furthermore adaptive move limits are applied since the solution tends to oscillate between solutions. The adaptive move limits that have been applied are detailed in Algorithm 1. $\Delta^{(n)}_{adap,ec}$ denotes the allowable change of the density of element $e$ for a given candidate material $c$ at iteration $n$.

**Algorithm 1** Pseudo code for determining adaptive move limits.

$O_{sc} = (x_{ec}^{(n-1)} - x_{ec}^{(n-2)}) \cdot (x_{ec}^{(n-2)} - x_{ec}^{(n-3)})$
**if** $O_{sc} < 0$ **then**
  $\Delta^{(n)}_{adap,ec} = \Delta^{(n-1)}_{adap,ec} \cdot 0.7$
**else if** $O_{sc} > 0$ **then**
  $\Delta^{(n)}_{apap,ec} = \Delta^{(n-1)}_{adap,ec} \cdot 1.2$
**else if** $O_{sc} = 0$ **then**
  $\Delta^{(n)}_{adap,ec} = \Delta^{(n-1)}_{adap,ec}$
**end if**

### 5.1.2 Evaluation criteria

In order to compare the results both the distribution of the material and failure indices will be compared. Furthermore the measures of non-discreteness will be used to determine the discreteness of the solution. Two measures of non-discreteness are introduced. They define the total density discreteness and the candidate material discreteness and are based on the formulas by Sørensen, Sørensen, and Lund (2014). These formulas are intended for the discrete material and thickness optimization, which includes a thickness variable in the DMO. When the thickness variable is set to 1 the material non-discreteness can be determined using Equation 5.3a. In order to determine the density non-discreteness the thickness variable is replaced by a summation of the material densities within the element as given in Equation 5.3b.
These two measures can thus be used to determine the non-discreteness of the structure, where 100 % means that the structure is fully non-discrete and 0 % means that the structure is fully discrete. It should be noted that these formulas yield non-physical results if Equation 5.1c is not satisfied.

$$M_{cnd} = \frac{\sum_{e=1}^{n_{elem}} V_e \prod_{c=1}^{n_{mat}} \left( \frac{1 - x_{ec}}{1 - (1 + n_{mat})^{-1}} \right)^2 \left( \sum_{c=1}^{n_{mat}} x_{ec} \right)^2}{\sum_{e=1}^{n_{elem}} V_e} \cdot 100\% \tag{5.3a}$$

$$M_{dnd} = \frac{4 \sum_{e=1}^{n_{elem}} V_e \sum_{c=1}^{n_{mat}} x_{ec} (1 - \sum_{c=1}^{n_{mat}} x_{ec})}{\sum_{e=1}^{n_{elem}} V_e} \cdot 100\% \tag{5.3b}$$

### 5.1.3 Baseline results for benchmark problem

The result for the benchmark problem with the settings from Table 5.1 and the SLP algorithm as the solver can be seen in Figure 5.2.

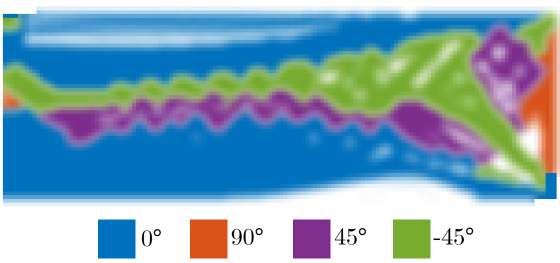


(a) Material distribution of the four fiber angles.

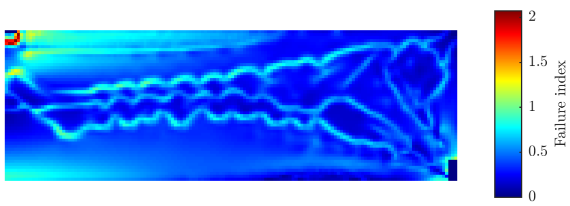


(b) Failure index for the geometry.

Figure 5.2: Baseline results for the benchmark problem.

The non-discreteness of this result is $M_{dnd} = 21.25\%$ and $M_{cnd} = 18.05\%$. After 1500 iterations the solution converges to the design seen in Figure 5.2a, with a volume fraction of 97.2%. It should though be noted that the constraint on the failure criteria is not fulfilled since it is above 1. This is not a good solution due to the high volume fraction, which is not

expected for this load case.
This result could be due to a poor local minimum, thus different continuation approaches have been implemented to get a better result. These are explained in Appendix C. The continuation approaches did not result in a better solution and it is thus not expected that the problem is a poor minimum. Therefore other methods have to be examined.

## 5.2 Stress concentrations at interfaces

When the results for the original benchmark problem given in Figure 5.2 are examined, it is seen that the highest failure indices are located at the interfaces between two different materials. A simpler problem is thus set up to investigate these interface effects. This problem resembles a tensile rod with uniformly distributed load and two materials as shown in Figure 5.3. The density of these two materials is 1 in their respective areas and the failure index is calculated in each element. The optimization will thus not be run and only the results from the finite element analysis are investigated.
First the tensile rod will be simulated without filters and afterwards it will be simulated with a density filter with filter radius 8 mm. The stiffness penalization factor $p = 3$ and the failure index relaxation factor $q = 2.5$ will be used to interpolate the intermediate densities. The force $F$ =500 N.

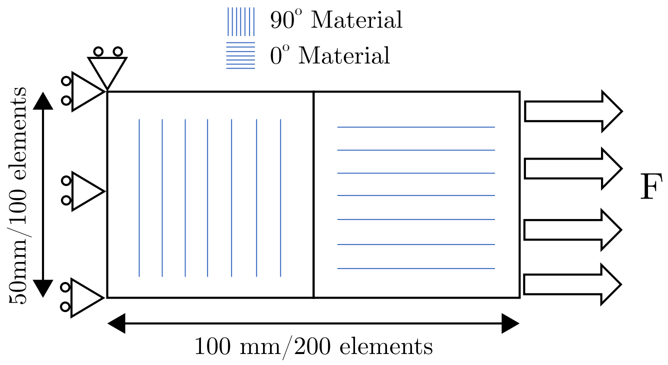


Figure 5.3: Boundary conditions and material orientation for tensile rod.

The results are shown in Figure 5.4 and as it is seen the failure index has a sharp transition between the two materials when no filter is applied, thus the failure index does not rise at the interface. The results with the density filter show an increase in the failure index at the interface between the two materials.

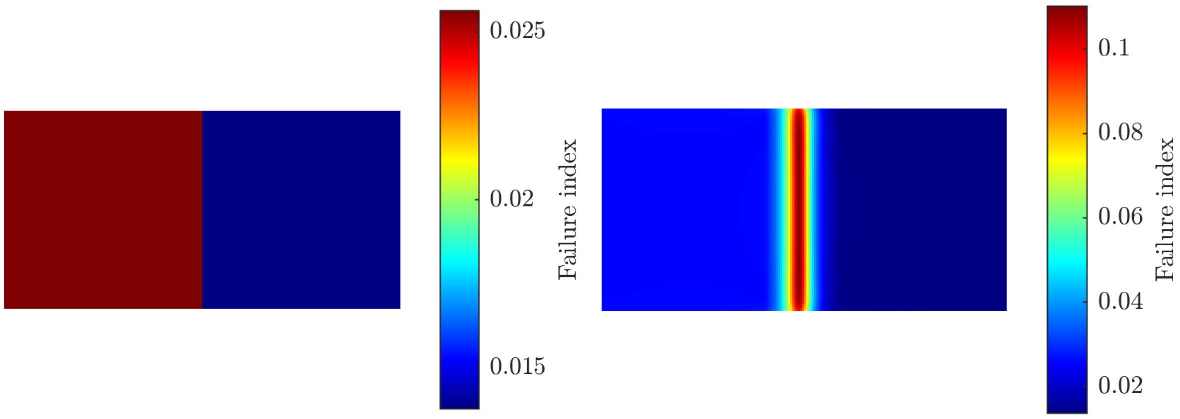


(a) Without filter.

(b) With density filter.

Figure 5.4: Failure indices of tension rod.

The high failure indices from utilizing the density filter are a result of the penalization of the intermediate densities. The stiffness is penalized by decreasing it compared to linear interpolation. Due to this low stiffness the strains will be high in the transition area. When calculating the stresses the constitutive matrix is relaxed using an above linear interpolation, which yields a stiffer material. Therefore the stresses and thus the failure indices will increase because a low stiffness is used to calculate the strains, while a high stiffness is used to calculate the stresses.
This is what penalizes the intermediate densities, which is not a problem when considering single material topology optimization (Le et al. 2010). The problem arises when using the DMO to include fiber angles, since the failure indices are summed for all the materials within each element. When multiple materials exist in a single element it is thus penalized further.

In order to solve the problem different approaches can be taken which includes the following:

- Remove penalization by setting $q = 0$
- Remove summation of the failure indices within each element
- Remove filters

If the penalization is removed by setting $q = 0$ the stress concentration will be removed and the transition between materials will yield a smooth transition between the failure indices. This is shown in Figure 5.5. The problem with this solution is that it might create an all void design, thus it is not a suitable solution. This phenomena is also observed in single material stress constrained topology optimization as reported by Duysinx and Bendsøe (1998).

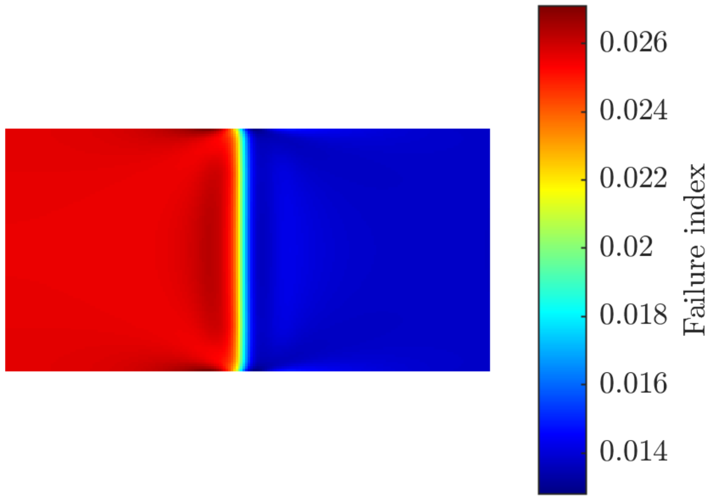


Figure 5.5: Failure index when $q = 0$.

In the original formulation the failure index in each element is calculated using Equation 4.37a. This equation will be replaced by Equation 5.4.

$$FI_{rel,ec} = w_{FI,ec} FI_{ec} \tag{5.4}$$

Since an above linear weight function is used to penalize the failure indices, the sum of the weights will not necessarily be 1. Therefore a summation will create an artificially weak material at intermediate densities thus penalizing them. By treating each material separately a relaxed failure index is obtained for each material for each element thus removing this penalization. All these failure indices are then input to the P-norm aggregate function in order to approximate the maximum failure index. This reformulation only affects intermediate densities and thus when the densities are at 0 or 1 the results will be the same.
In order to investigate the effect of this change it is tested utilizing a threshold filter in order to get a more discrete solution. The beta parameter is raised using a continuation approach, where it is doubled every 50 iterations until it has reached the maximum value, which is equal to the filter radius as recommended by Silva, Beck, and Sigmund (2019) for stress constrained problems. The results are seen in Section 5.2.1.

The last method to resolve the problem is to remove the filters. If the filters are removed checkerboarding is observed as described in Section 4.3. It is thus necessary to switch the element formulation to use quadratic elements, in order to minimize these non-physical effects. Removing the filters will also remove the minimum length scale, which the filters introduce. Therefore care has to be taken when post processing the results in order to ensure manufacturability.
The element which is implemented is the nine node Lagrangian element using the isoparametric formulation. The shape functions and the strain displacement matrix are given in Appendix D. They are given in the natural element coordinate system and thus the integral given in Equation 4.2 is transformed to integrate over the natural coordinates. The resulting integrals are given in Equation 5.5, where $J$ is the determinant of the Jacobian.

Gauss quadrature is used to calculate the stiffness matrix using full integration, which for a quadratic element utilizes 3x3 Gauss points.

$$[k_e] = \int_{-1}^{1}\int_{-1}^{1}[B(\xi,\eta)]^T[C_e][B(\xi,\eta)]Jtd\xi d\eta = \sum_{i=1}^{3}\sum_{j=1}^{3} w_{ij}[B(\xi_i,\eta_j)]^T[C_e][B(\xi_i,\eta_j)]Jt \quad (5.5)$$

When changing to quadratic elements the stresses should be calculated in the 2x2 Gauss points, since the stresses are the most accurate here. These stresses can either be averaged or interpolated to the center point, in order to get a single stress vector for each element. This has not been done and the stresses are evaluated directly in the center instead.
Furthermore the loads have to be distributed work equivalently. For a quadratic element a constant distributed load should be distributed with $\frac{1}{6}$ of the force on the corner nodes, while $\frac{2}{3}$ should be placed at the midside node (Cook et al. 2002).

### 5.2.1 Results from numerical tests

The two approaches described above have been implemented and tested. In the following when referring to these two approaches only the element formulation will be noted. Thus the bilinear formulation refers to the problem with the bilinear elements with threshold filter but without summation of the failure indices. The same is applicable to the quadratic formulation. The problem considered is the MBB beam as described in Section 5.1, but with the changes as described above.
The results are seen in Figure 5.6. The location of the different materials are similar for the two different element types, with the material in the 0° direction being at the outside, while the material in ±45° is located in the middle.
When using the bilinear elements the minimum feature size is larger. This is due to the added minimum length scale from the threshold filter. In the test with the quadratic elements, the individual branches of the geometry are thinner and as seen in Figure 5.6b, some branches are only a single element wide. This is especially a problem for the branches in ±45° since the elements are only connected at a single node. This is not possible to manufacture on a FFF 3d-printer since features smaller than the line width as described in Section 3.1.4 are not feasible. The results must thus be post processed in order to ensure manufacturability.

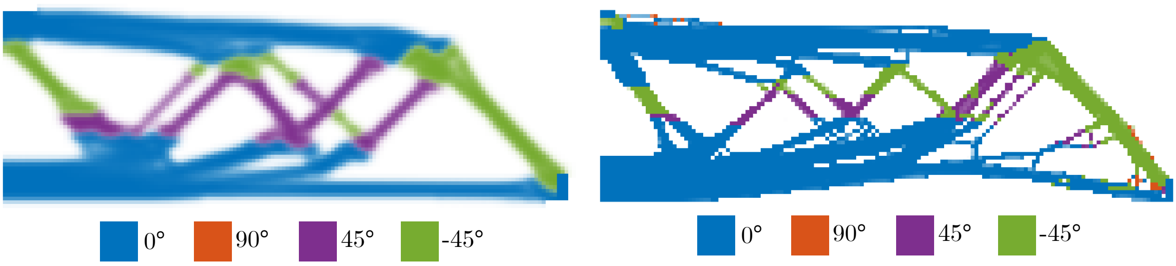


(a) Linear elements.

(b) Quadratic elements.

Figure 5.6: Material distribution after 1500 iterations.

The quadratic element formulation yields a more discrete result. This is due to the lack of filtering and the harder penalization of intermediate densities through summing the failure indices.
The quadratic element formulation also result in a lower volume fraction, which can be a result of the solution being more discrete. The volume fraction and the measures of non-discreteness for the two tests can be seen in Table 5.2.

| | $M_{dnd}$ | $M_{cnd}$ | $max(FI)$ | Volume percentage |
|---|---|---|---|---|
| Linear elements | 29.1% | 13.1% | 1 | 47.23% |
| Quadratic elements | 2.19% | 0.51% | 1.0047 | 44.83% |

Table 5.2: Final results for the different element formulations.

The quadratic elements result in a failure index above 1, thus the constraint is not satisfied. The constraint is only violated slightly, which might not matter for practical problems, but it might though increase with the penalization. The reason is that the solution gets to discrete, which creates staircasing as discussed in Section 4.3. This is also seen in the convergence history given in Figure 5.7.
After around 100 iterations the merit function variable $y$ from Equation 5.2 falls to 0, but as the geometry keeps getting more discrete a point is reached, where the optimization cannot keep the value at 0. This can be seen in Figure 5.7 as a sudden increase in the merit function variable at around iteration number 500.
A convergence criteria is applied to the measure of density non-discreteness of 10% in order to ensure that the solution does not get too discrete. Thereby staircasing is avoided. The objective function does not change significantly after the density non-discreteness reaches 10%, thus the solution does not get better. The reduced discreteness can also ease the post processing, when the final geometry is created. This will be further discussed in Section 7.1.

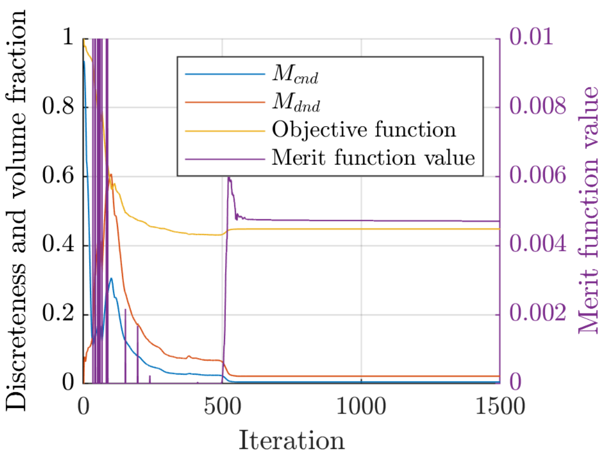


Figure 5.7: Convergence history when using quadratic elements.

The convergence criteria of $M_{dnd} \leq 10\%$ is applied to the optimization with the quadratic elements. This resulted in the optimization converging after 122 iterations. The material distribution can be seen in Figure 5.8.

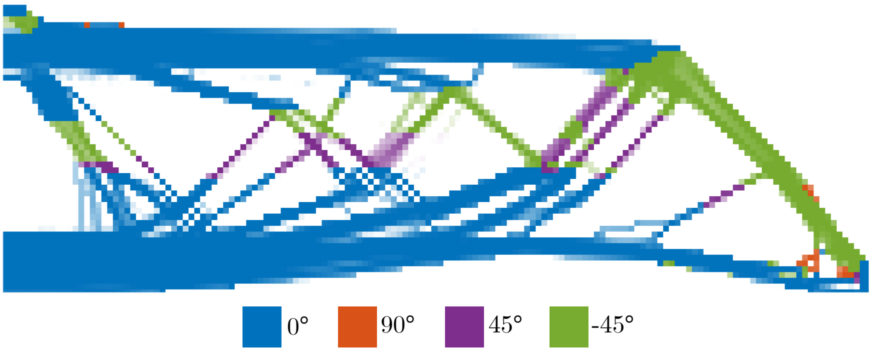


Figure 5.8: Material distribution for quadratic elements when applying convergence criteria.

The failure index for the bilinear element formulation and the quadratic element formulation are both satisfied and the distribution can be seen in Figure 5.9. Since multiple failure indices exist for each element when using the bilinear formulation the maximum failure index in each element is plottet. The failure indices for the individual materials are given in Appendix E. It is seen that the material is utilized better using the quadratic elements. This is due to the minimum feature size introduced by the filtering of the bilinear elements.

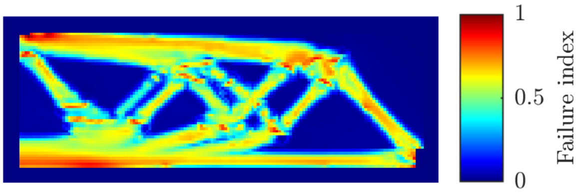


(a) Maximum failure index in each element of bilinear elements.

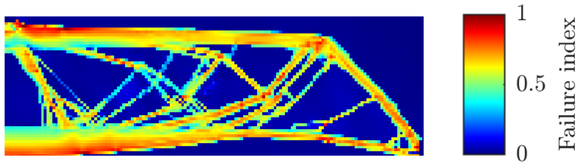


(b) Quadratic elements.

Figure 5.9: Failure index distribution.

## 5.3 Conclusion of numerical testing of optimization problem

In simultaneous topology and fiber angle optimization using DMO on a strength constrained problem, it has been observed that failure indices can get excessively high between candidate materials. This problem arises due to the filtering, which is necessary in order to avoid checkerboarding and to introduce a minimum length scale, when using the bilinear element formulation. A way to circumvent the checkerboarding problem is to introduce a quadratic element formulation, that does not need filtering. This although removes the constraint on the minimum length scale, which is introduced by the filtering, thus it can result in problems with manufacturability.
Another solution to the excessive failure indices, is to remove the summation the failure indices. This reduces the failure index for elements containing intermediate densities of multiple materials, but will result in the same failure index for the solid and void elements. Both methods can be viable but the quadratic element formulation requires more post processing.

# 6 Numerical studies of L-bracket

Throughout this chapter the simultaneous topology and fiber orientation optimization, with a strength constraint will be applied to the L-bracket geometry, which can be seen in Figure 6.1. This benchmark has been chosen since it includes a geometric stress constraint, that the optimization has to alleviate through the iterations. Optimization for the two different materials tested in Section 3 will be evaluated, for the two element formulations described in Section 5.2.1. The element formulations will be compared in order to evaluate the use cases. The implementation of the two materials will show how the optimization handles varying degrees of orthotropy. The strength based optimization results will be compared to compliance based optimization of the same problem in order to evaluate the difference between the two types of optimization.

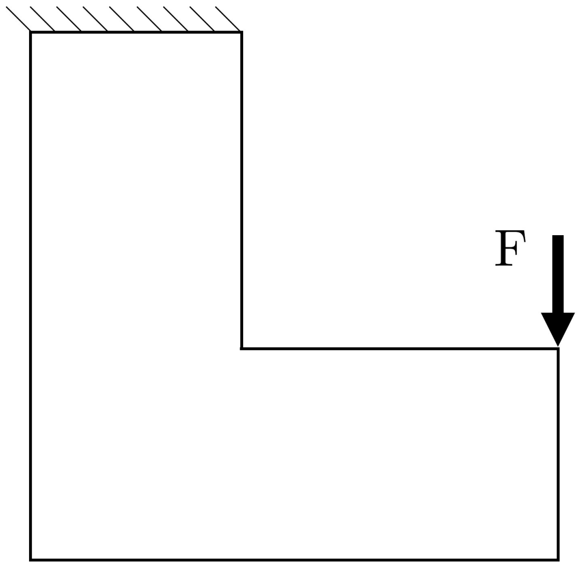


Figure 6.1: L-bracket benchmark.

## 6.1 Description of optimization problem

The L-bracket benchmark differentiates from the MBB-beam benchmark by introducing a geometric stress concentration. This stress concentration should be alleviated by the strength constraint optimization. The problem is defined as seen in Figure 6.2. The force is applied work-equivalent over 7 elements at the tip of the L-bracket. The adjacent 3x15 elements all have a density of 1 and are excluded from the optimization. This is in order to avoid a stress concentration from the application of the force. Padding elements are added around the design space in order to accommodate the edge effects from the filters, as described in Section 4.3.3. The padding is not necessary when using the quadratic element formulation, because the filters are not used.

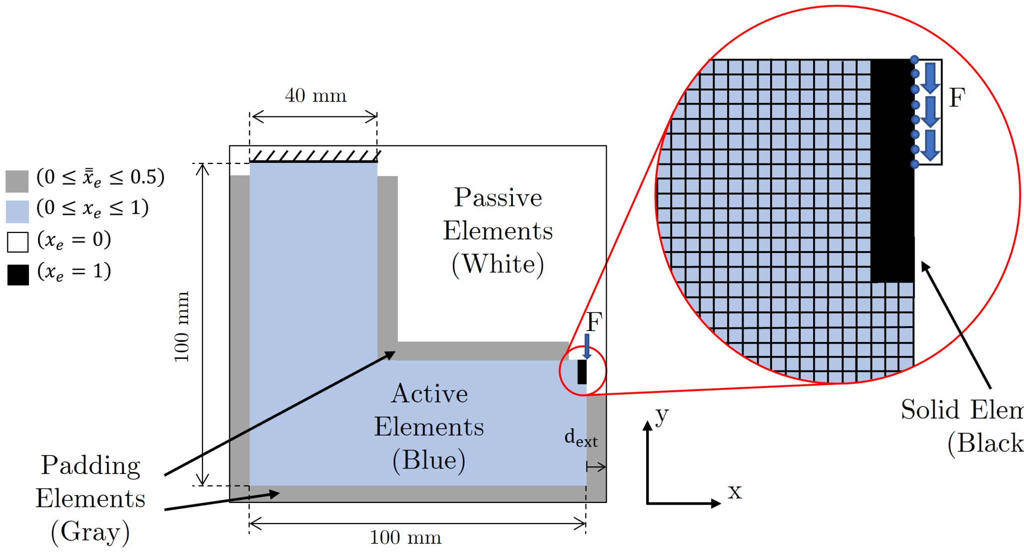


Figure 6.2: Definition of L-bracket benchmark.

The settings that will be used for the L-bracket benchmark are seen in Table 6.1.

| | | |
|---|---|---|
| Domain size | | 250x250 elements |
| Domain extension | $d_{ext}$ | 6 elements |
| Material | | Smooth PA or CCF |
| Possible directions | | [0°; 90°; 45°; −45°] |
| Filter | | Threshold |
| Objective | | Strength |
| Force | $F$ | 500 N |
| P-norm aggregation factor | $P$ | 8 |
| Stiffness penalization factor | $p$ | 3 |
| Failure index relaxation factor | $q$ | 2.5 |
| Constant move limits | $\Delta_{con,ec}$ | 0.025 |
| Filter radius | $R$ | 1.2 mm (3 elements) |
| Max iterations | | 1500 |
| Convergence criteria | $M_{dnd}$ | $\leq 10$ |

Table 6.1: Settings for the L-bracket problem.

## 6.2 Results for Smooth PA

The material distribution for the L-bracket using the quadratic elements is given in Figure 6.3a, while the corresponding distribution of failure indices is given in Figure 6.3b. The optimization is stopped after 400 iterations since the convergence criteria on the measure of density non-discreteness was fulfilled. The final volume percentage is 21.00% while $M_{dnd} = 9.68\%$ and $M_{cnd} = 3.91\%$.

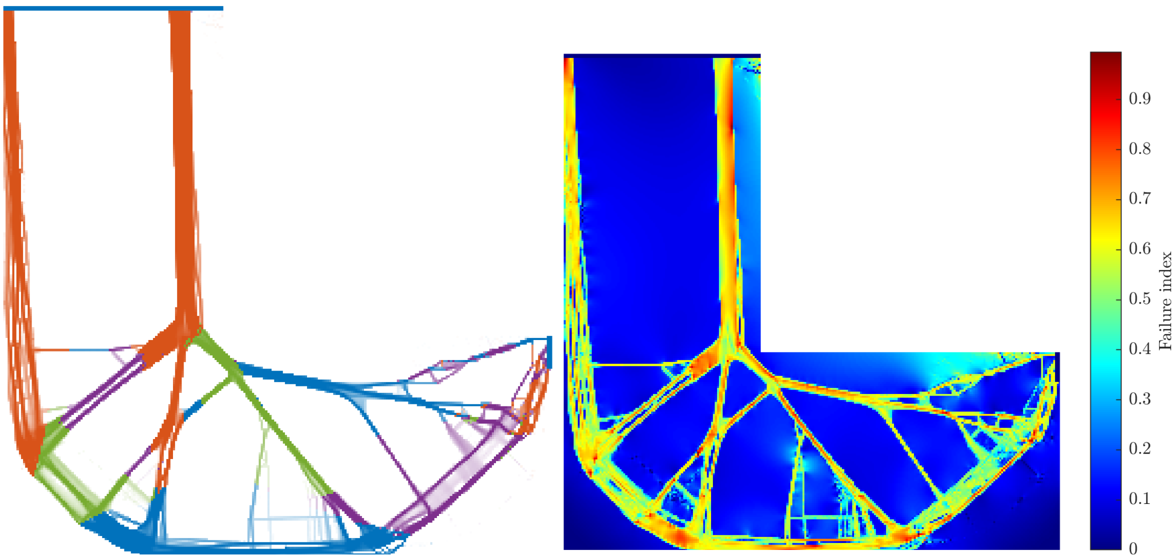


(a) Material distribution. (b) Distribution of failure indices.

Figure 6.3: Results for L-bracket using nine node quadratic element.

Because of the convergence after 400 iterations the results still have intermediate densities as seen in Figure 6.3a. This is necessary in order to avoid local stress concentrations that arise when the result becomes too discrete. Some of the branches in the structure seen in Figure 6.3a are only one element thick. This is not possible to manufacture as described in Section 5.2.1 for the MBB-beam and post processing is thus necessary. This will be explained in Section 7.1.

The optimization of the Smooth PA L-bracket using the bilinear elements resulted in a volume percent of 19.08% and measures of non-discreteness of $M_{dnd} = 14.29\%$ and $M_{cnd} = 6.09\%$. The optimization did therefore not reach the convergence criteria of an $M_{dnd} \leq 10\%$, which means the optimization ended after 1500 iterations. The results can be seen in Figure 6.4

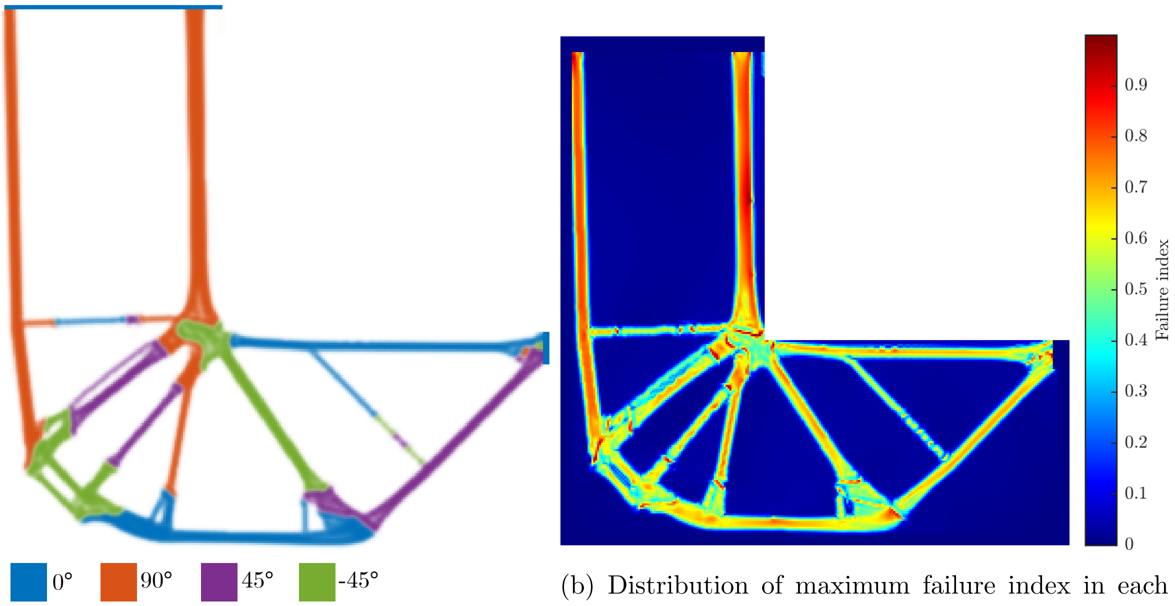


(a) Material distribution.

(b) Distribution of maximum failure index in each element.

Figure 6.4: Results for L-bracket using four node linear element using Smooth PA.

The failure indices for each material for the bilinear element formulation can be seen in Appendix E.

When comparing the results of the bilinear elements and the quadratic elements, it can be seen that they give mostly the same result. In both cases the failure constraint is satisfied and they reach around the same volume fraction. The measures of non-discreteness and the minimum length are the largest differences between the two results. In order to manufacture the result from the quadratic elements the geometry has to be post processed, by adding some filtering to the geometry. This is not the case for the result of the bilinear elements. The convergence of the two results can be seen in Figure 6.5. The values for the bilinear elements converge to a steady result after around 100 iterations and with slight changes at 200 and 400 iterations, where the $\beta$ value from the threshold filter is increased. The results from 500 to 1500 iterations are not included because the values do not change in this range.

The quadratic elements do not converge as fast as the bilinear elements since they reach an almost steady solution after around 100 iterations. The quadratic elements though need only 400 iterations to converge to a solution, which satisfies the convergence criteria. The quadratic elements also reach a more discrete solution at the end.

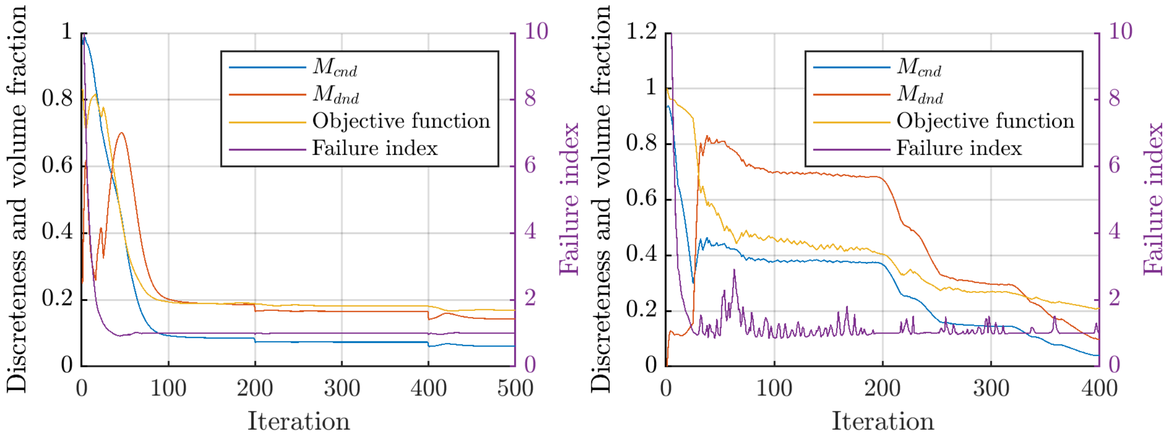


(a) Bilinear elements.

(b) Quadratic elements.

Figure 6.5: Convergence history for L-bracket using Smooth PA.

## 6.3 Results for CCF

The L-bracket benchmark is also optimized with CCF. This shows how the optimization deals with more orthotropic material properties. The continuous fiber L-bracket benchmark will be optimized using both the bilinear and the quadratic elements. The L-bracket benchmark with CCF uses the same settings as described in Table 6.1. The number of solid elements adjacent to the added force is raised from 3x15 to 5x15 elements. This is in order to avoid a stress concentration, where the force is applied.

The material distribution for the quadratic elements can be seen in Figure 6.6a together with a plot of the failure index in Figure 6.6b. The CCF L-bracket benchmark with quadratic elements results in a volume fraction of 10.99% and measures of non-discreteness of $M_{dnd} = 12.01\%$ and $M_{cnd} = 5.93\%$. The solution did not reach the convergence criteria and was therefore stopped after 1500 iterations.
The measures of non-discreteness are higher than for Smooth PA. This is due to the high strength of the CCF and thus it is not necessary to use solid elements even though the intermediate densities are penalized.

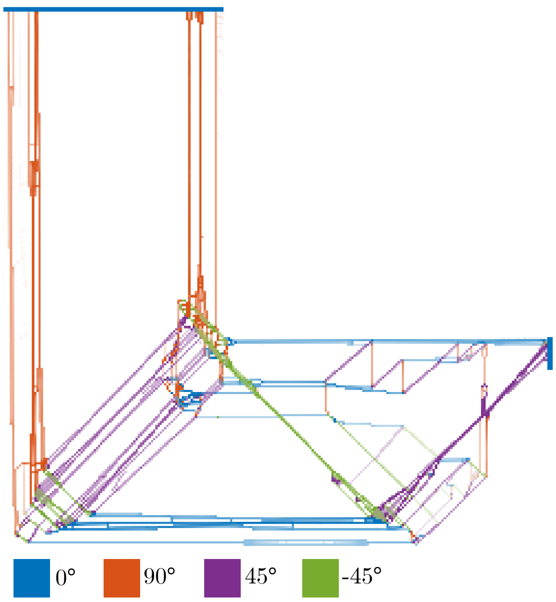


(a) Material distribution.

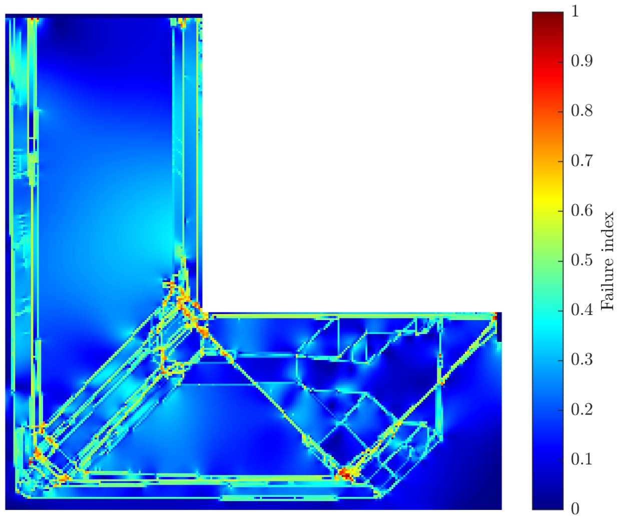


(b) Distribution of failure indices.

Figure 6.6: Results for L-bracket using nine node quadratic elements with continuous fibers.

The continuous fiber L-bracket benchmark for the quadratic elements result in a structure consisting of very thin branches due to the high strength in the fiber direction. This result in the same manufacturing issues as for the other solutions obtained using the quadratic elements. Furthermore the structure is prone to buckling, because the length to width ratio of the branches is high. This is not accounted for during the optimization.
The force applied in the optimization could be increased in order to enforce a thicker structure. This would although not be a viable option since it alters the aim of the optimization. Furthermore the force cannot be increased significantly since the loading transverse to the

fiber orientation would also increase and thus result in failure.

The results of the optimization of the L-bracket benchmark with bilinear elements is seen in Figure 6.7. The optimization resulted in a volume fraction of 21.2% and measures of non-discreteness of $M_{dnd} = 20.85\%$ and $M_{cnd} = 10.69\%$. This optimization did not reach the convergence criteria either and therefore performed all 1500 iterations.

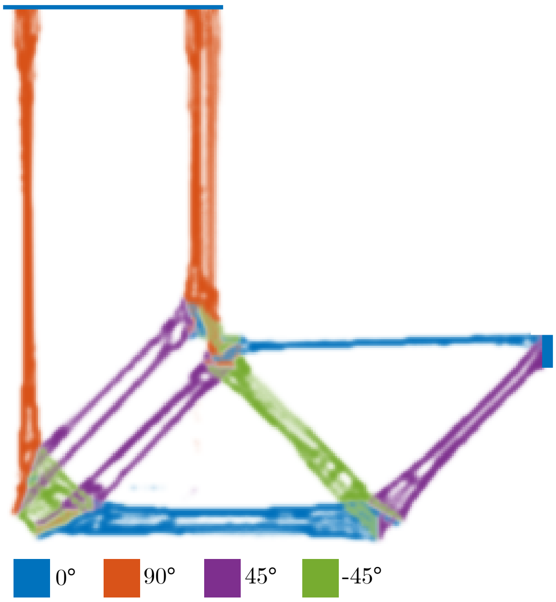


(a) Material distribution.

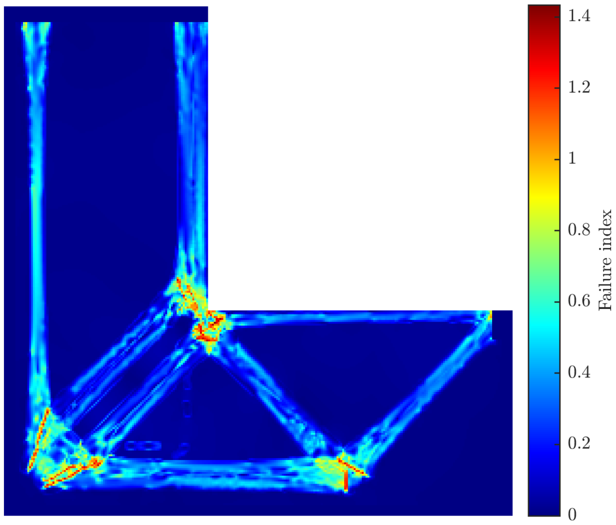


(b) Distribution of maximum failure index in each element.

Figure 6.7: Results for L-bracket using four node linear element using CCF.

The failure indices for each material for the bilinear element formulation can be seen in Appendix E. The result for the bilinear elements of the CCF L-bracket benchmark does not fulfill the failure criteria as seen in Figure 6.7b. The material distribution in the areas with large failure index is a mix of more than one material. This is due to the loading in multiple directions, which necessitates multiple fiber orientations. When the discreteness is increased due to the threshold filter, only one material can be left. This can also be seen from the convergence plot of the bilinear element in Figure 6.8a. The failure index increases, when the $\beta$ value changes after 200 and 400 iterations.

The convergence plot for the quadratic elements can be seen in Figure 6.8b. From iteration 500 to 1500 the values stabilise and become constant.

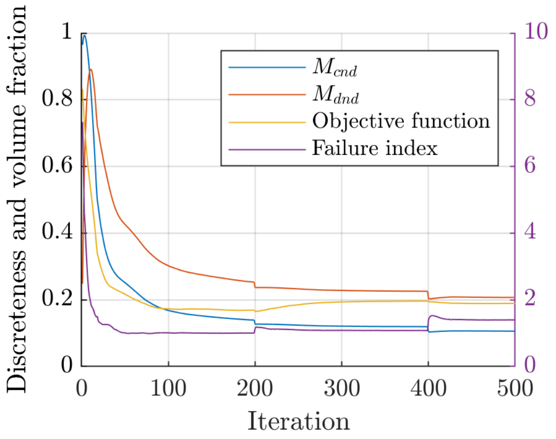


(a) Bilinear element.

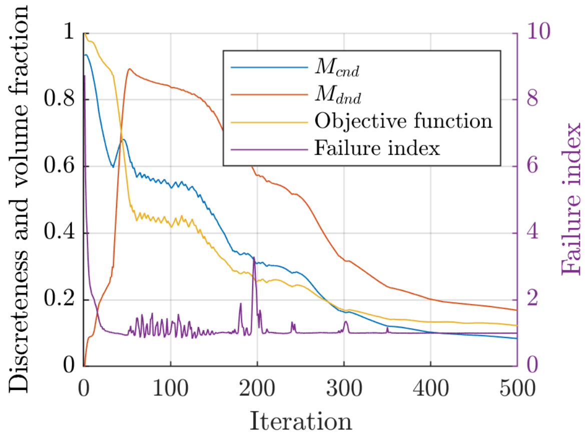


(b) Quadratic element.

Figure 6.8: Convergence history for L-bracket using CCF.

The results obtained using CCF are all less manufacturable than the results obtained for Smooth PA. This is due to the highly orthotropic material properties of the CCF material. The results obtained from the quadratic elements are not possible to 3D-print. The results obtained from the bilinear elements require less post processing but the failure index is not satisfied. The optimization can therefore not converge to a satisfactory result, when using very orthotropic material properties.

## 6.4 Comparison of results including compliance

This section will include a comparison between the strength based results for the Smooth PA material and a compliance based optimization. Both element formulations will be compared.

A compliance based optimization is performed for the same L-bracket problem specified in Section 6.1. The problem is a minimisation of the compliance with a volume constraint. The volume constraint is specified based on the result from the strength based optimization in Section 6.2. The compliance benchmark with quadratic elements has a volume constraint of 21%, where the bilinear compliance benchmark has a volume constraint of 19%. Furthermore the convergence criteria on the density non-discreteness is not applied.

The material distribution from the compliance benchmark of the L-bracket with Smooth PA can be seen in Figure 6.9. The results from the bilinear and quadratic element formulation are both very similar, with almost the same material distribution. The difference is the same as for the strength based optimization, where the missing filtering on the quadratic elements causes a non-manufacturable result. The measures of non-discreteness for the bilinear elements are $M_{dnd} = 10.04\%$ and $M_{cnd} = 4.04\%$, where they for the quadratic elements are $M_{dnd} = 1.68\%$ and $M_{cnd} = 0.17\%$.

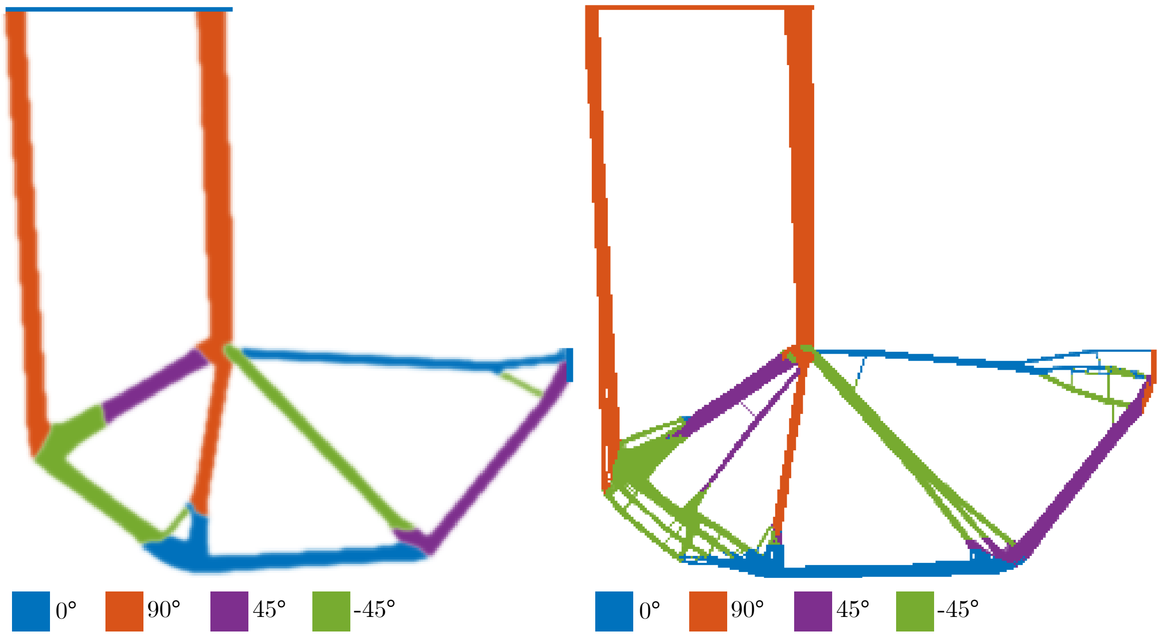


(a) Bilinear element.

(b) Quadratic element.

Figure 6.9: Material distribution for compliance optimized L-bracket.

A comparison of all the Smooth PA L-bracket benchmarks can be seen in Table 6.2. All the material distributions of the benchmark results are almost identical, although the discreteness varies. In general the bilinear element formulation has a higher level of non-discreetness due to the added filtering. For both the compliance and the strength optimization the results obtained by the quadratic elements need further post processing in order to make the results manufacturable.

| | Strength | | Compliance | |
|---|---|---|---|---|
| | Bilinear | Quadratic | Bilinear | Quadratic |
| Volume fraction | 19.08 | 21.00 | 19.08 | 21.00 |
| $M_{dnd}$ | 14.29 | 9.68 | 10.04 | 1.68 |
| $M_{cnd}$ | 6.09 | 3.91 | 4.04 | 0.17 |
| Post processing | Low | High | Low | High |

Table 6.2: Comparison of strength and compliance results for Smooth PA.

Comparing the compliance against the strength based results around the geometric stress concentration, they show different results. This is due to the two different optimization schemes. The compliance optimization does not alleviate the geometric stress constraint introduced by the L-bracket geometry. This will result in a high local stress concentration, thus the strength based failure index will not be fulfilled. The failure index is calculated for the quadratic element formulation, optimized for the compliance and can be seen in Figure 6.10.

In order to ensure that the geometry does not fail thus the strength based optimization must be used.

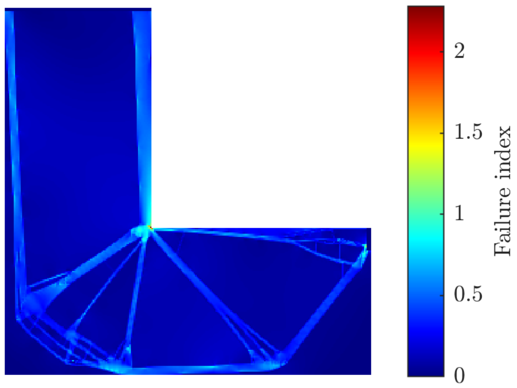


Figure 6.10: Distribution of failure indices of compliance optimized L-bracket with quadratic elements.

# 7 Experimental validation

Throughout this chapter the post processing needed in order to manufacture the optimized geometries will be described. This includes the needed filtering in order to introduce a minimum length scale on the results obtained by the quadratic elements. The results from the Smooth PA MBB benchmark given in Section 5.2.1 will be manufactured and tested in order to validate the optimization against real world implementation.

## 7.1 Post processing

In order to print the results the 3D-printer needs a g-code file, which is created using the Aura slicer as described in Section 3.1.2. The geometry is input to the slicer through a stl-file. Furthermore stl-files are needed to describe the locations, where a given fiber orientation is used. They act as masks in which the infill direction can be specified. The task of post processing is thus to create a stl-file containing the geometry and a stl-file for each material direction, that can be used for specifying the infill orientation.

The stl-files are created using TOPSlicer by Zegard and Paulino (2016). This is a MATLAB program that is intended to bridge the gap between topology optimization and additive manufacturing. It takes in a matrix with the element densities and interpolates these linearly. Afterwards the isosurface is calculated using a threshold value, which is typically set to 0.5. This makes it beneficial to have some amount of intermediate densities at the edges in order to get a smooth geometry. This is therefore beneficial for the solution obtained using the linear elements, with filtering due to their higher non-discreteness. Furthermore the solution obtained from the linear elements have a minimum length scale defined through the filter radius and thus no post processing is necessary and the stl-file can be created directly from the results of the topology optimization.

If the same is tried for the results obtained using the quadratic elements all the thin branches in the 45° and −45° directions will be discontinuous, because they are only connected at a single node. This is seen in Figure 7.1. Furthermore it is seen that the geometry is pixelated, which is caused by the high discreteness of the solution.

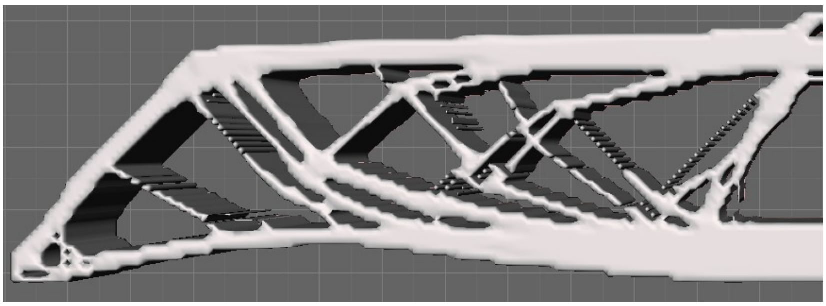

Figure 7.1: Stl-file for quadratic elements if no filtering is used.

These problems can be solved by using filtering. A simple solution would be to use the linear density filter, which is also applied in the topology optimization for the linear element. This

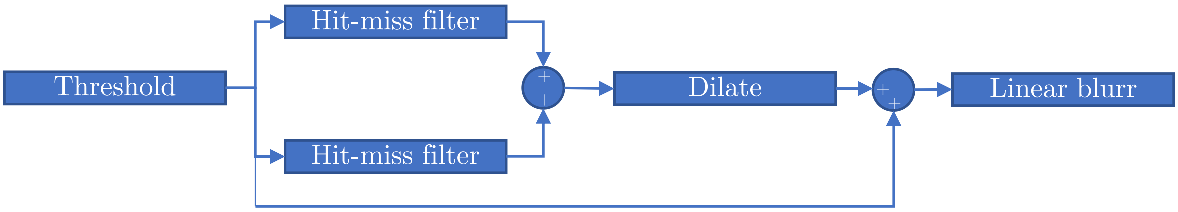


Figure 7.2: Structure of the implemented post processing filtering.

although would decrease the density of the thin branches in the ±45° directions and thereby remove these. It is thus necessary to increase the thickness of these branches in order for them not to be removed.

Different traditional image filtering techniques have thus been investigated in order to determine a suitable method. The method should increase the non-discreteness while not removing the thin branches in the ±45° directions.

The basic idea of the implemented filtering is thus to detect these thin branches and increase the size of them. Afterwards the results are blurred using a linear weighted moving average in the same way, as the density filter used in topology optimization. The filtering process is described in Figure 7.2 and the results of each step are seen in Figure 7.3.

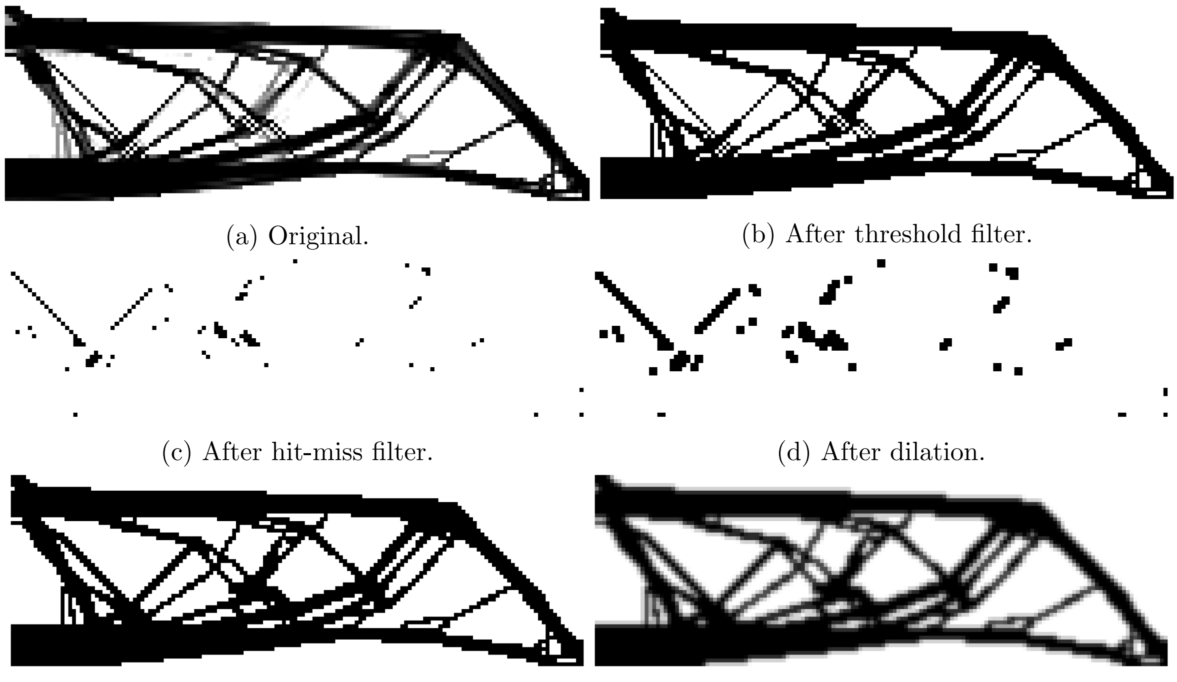

(a) Original.

(b) After threshold filter.

(c) After hit-miss filter.

(d) After dilation.

(e) After summation of thresholded and dilated.

(f) Blurred.

Figure 7.3: History of density distribution throughout the filtering process.

First the density distribution is thresholded in order to create a binary distribution. In this way information is lost but since the original density distribution has a low non-discreteness the amount of lost information is low. The threshold filter is used in order to apply the hit-miss filter, which is a binary morphological image processing technique. The method searches for the structural elements $SE_{HM+45}$ and $SE_{HM-45}$ from Equation 7.1 and returns

1 if it is found and 0 if not. These structural elements search for the thin branches in the 45° and −45° directions. The result of this search is seen in Figure 7.3c.

$$SE_{HM+45} = \begin{bmatrix} 0 & 1 \\ 1 & 0 \end{bmatrix} \qquad SE_{HM-45} = \begin{bmatrix} 1 & 0 \\ 0 & 1 \end{bmatrix} \qquad SE_D = \begin{bmatrix} 1 & 1 \\ 1 & 1 \end{bmatrix} \tag{7.1}$$

The results from the hit-miss filters are dilated using the structural element $SE_D$. This is also a binary operation, which searches for ones in the original image and replaces it and the neighboring pixels, defined by the structural element with the structural element. The branches thus get thicker as seen in Figure 7.3d.
The dilated results are summed with the original thresholded density distribution and thus the thickness of the thin branches in the ±45° directions have been increased. At the end, the results are blurred using the standard linear weighted density filter from topology optimization in order to get a smoother geometry, when creating the stl-file. The filter radius of this blurring filter is 1.5 elements.

In order to evaluate the effect of the filter the volumes are compared. The volume after filtering and creation of the stl-file is given in Table 7.1. It is seen that the filtering reduces the volume even though a dilation process is used which increases the volume. This is due to the initial thresholding, which removes the intermediate densities and for this case removes material. When the stl-file is created the volume is increased because the threshold value is set to 0.3. This is necessary in order to increase the minimum feature size to make it possible to manufacture the part.

| Geometry | Volume [$cm^3$] |
|---|---|
| Original | 10.7 |
| Filtered | 10.3 |
| Stl | 12.1 |

Table 7.1: Volume of part after different post processing steps.

## 7.2 Test setup

The g-code for the 3D-printer will be generated using the Aura slicer version 2.4.8, where the fiber directions will be added as masks in order to define the specified fiber direction in an area as described in Section 3.1.2. The 3D-printed benchmarks are generated with one wall to surround the infill in order to improve print quality and avoid stress concentrations. They are also generated with one top and bottom-layer in order to ensure good adhesion of the first layer.
The print settings used are the same as for the Smooth PA material tests as seen in Table 3.2. Both test geometries are manufactured on the Anisoprint Composer A4 using the Polymaker Smooth PA material. The manufactured test specimens will be tested in a 3 point bending rig mounted in a Zwick 100 kN testing machine. The test setup can be seen in Figure 7.4.

The 3 point bending rig has 120 mm between the two lower supports and tests are performed with a displacement rate of 2 $\frac{mm}{sec}$. Five test specimens will be tested for each of the two geometries in order to compare the results.
In order to better align the test specimens in the 3 point bending rig alignment blocks are made, which can be seen in Figure 7.5. They are designed to be 3D-printed and clip to the 3 point bending rig, in order to give a surface that the MBB test specimen can be aligned against. This makes the placement of the test specimens easier and more consistent, though the force might be distributed over a larger area at the two lower supports.

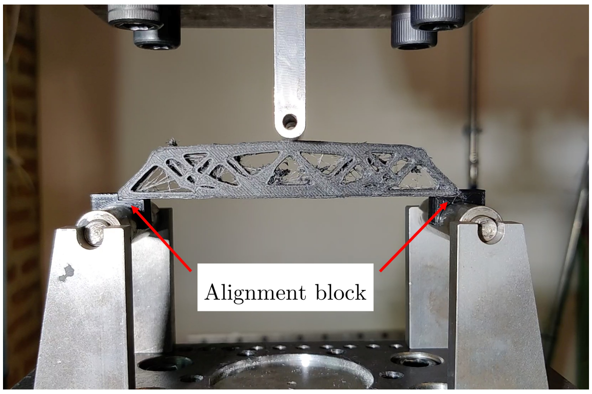


Figure 7.4: The 3 point bending setup

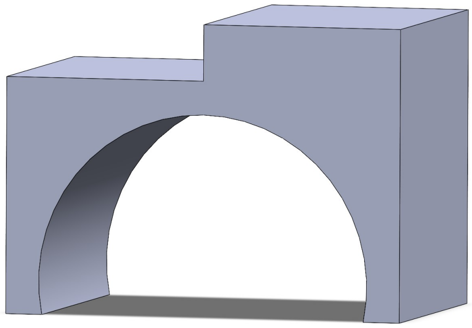

Figure 7.5: The alignment block.

### 7.3 Experimental validation of the results obtained from the quadratic elements

The geometry and the print paths for the quadratic MBB benchmark after slicing in the Aura slicer, can be seen in Figure 7.6. The print paths are not perfectly symmetrical, which can be seen by comparing the areas inside the two red circles marked in Figure 7.6. This is due to unsymmetrical generation of the stl-file. This problem is difficult to circumvent without changing the process of the stl-file generation. The unsymmetrical areas are small and is therefore estimated to not have a large impact on the structural strength of the 3D-printed MBB benchmark and will therefore not be changed.

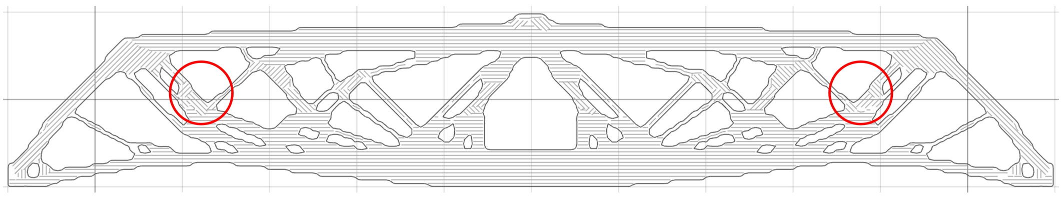

Figure 7.6: Print paths for the quadratic element formulation of the MBB-beam.

The 3D-printed quadratic MBB benchmark is seen in Figure 7.7. The 3D-printed geometry has a lot of stringing, which is seen as the thin material strands crossing the holes of the geometry. Stringing appears when the printer travels across the geometry, while moving from one print path to another. The Smooth PA will have a tendency of stringing due to the short fibers in the material and the Polyamide material in general have a tendency of stringing. The stringing can result in print defects along the geometry edge, which can introduce stress concentrations. An inspection of the fracture points of the tested specimens show, that they did not brake in areas with print defects. It is thus assumed that the stringing did not have an impact on the strength of the 3D-printed geometry.

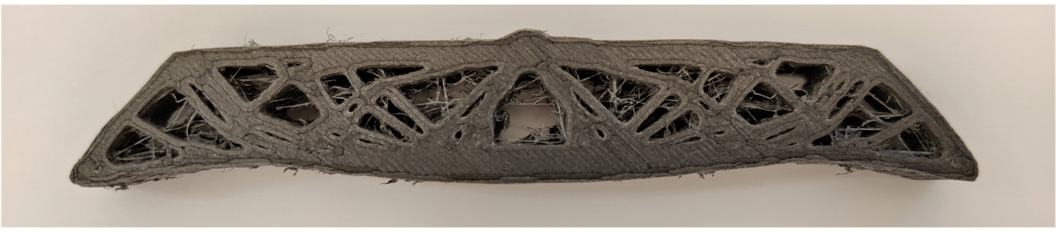

Figure 7.7: The 3D-printed quadratic MBB benchmark problem using Smooth PA.

The results from the five tests can be seen in Figure 7.8. The results are consistent for all five test samples. The mean of the maximum force of the five test is 1410 N, with a standard deviation of 11.8 N. This is more than the expected 1000 N, that was applied in the optimization. It is expected that the load bearing capacity is higher for the experimental test due to the post processing since it ads more material to the whole geometry.

As seen in Figure 7.8 there is a linear relation between the force and the displacement in the beginning of the test. There is though a kink at around 320 N, which is a result of the testing machine giving away. The point were it starts to behave non-linear is at around 1000 N, which is the failure load that was predicted. The procedure for determining this value is similar to the procedure for determining the 0.2% proof stress and is described below.
First a linear regression analysis is made. The linear fit is made between 400 and 600 N in order to avoid the kink. The linear curve is then moved 2.5% and 5% of the displacement at max load, along the displacement axis. The intersection between the linear fit and the data points is then calculated.
This led to the following results: 920 N for the 2.5% displacement and 1036 N for the 5% displacement.

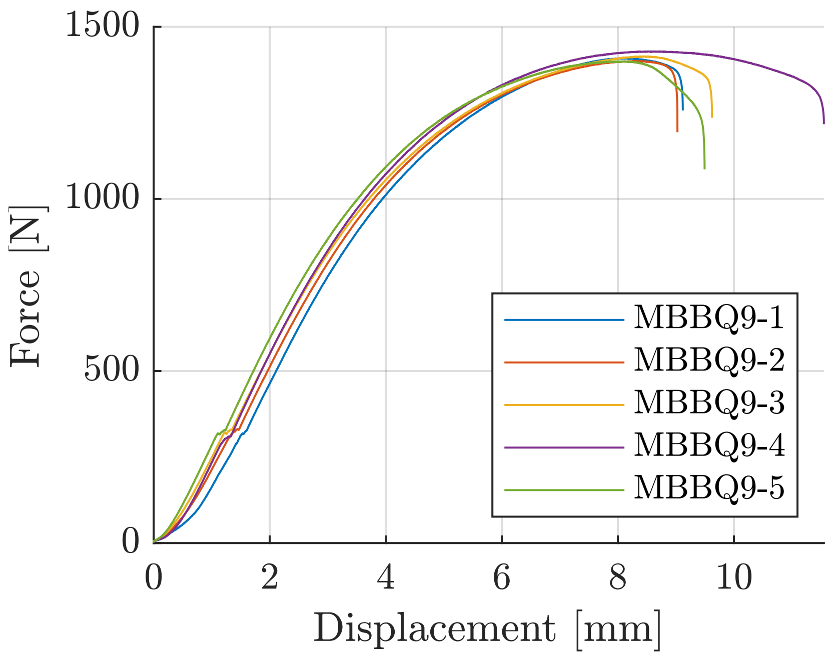


Figure 7.8: Results for the quadratic MBB benchmark tests.

## 7.4 Experimental validation of results obtained from the bilinear elements

The results of the MBB benchmark with the bilinear elements resulted in the following print paths seen in Figure 7.9, after being sliced with the Aura software. This sliced geometry also has areas with non-symmetric print paths, but the areas are smaller than for the geometry using the quadratic elements seen in Figure 7.6.

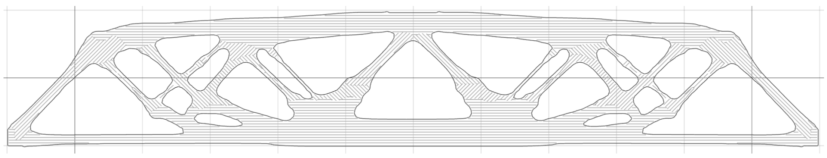

Figure 7.9: Print paths for the bilinear element formulation of the MBB-beam.

The printed geometry can be seen in Figure 7.10. This geometry also has stringing between the print paths. This is not assumed to have an affect on the structural strength, because none of the five tested specimens fail in the areas with stringing.

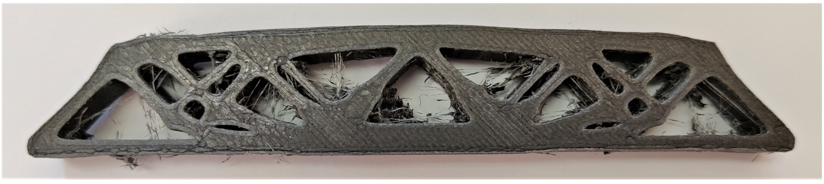

Figure 7.10: The 3D-printed bilinear MBB benchmark problem using Smooth PA.

The results from the five test specimens are seen in Figure 7.11. The mean of the maximum force for the five specimens is 1348 N, with a standard deviation of 17.5 N. The max load bearing capacity was therefore similar for all five tests, even though the failure mode is not consistent across the specimens.

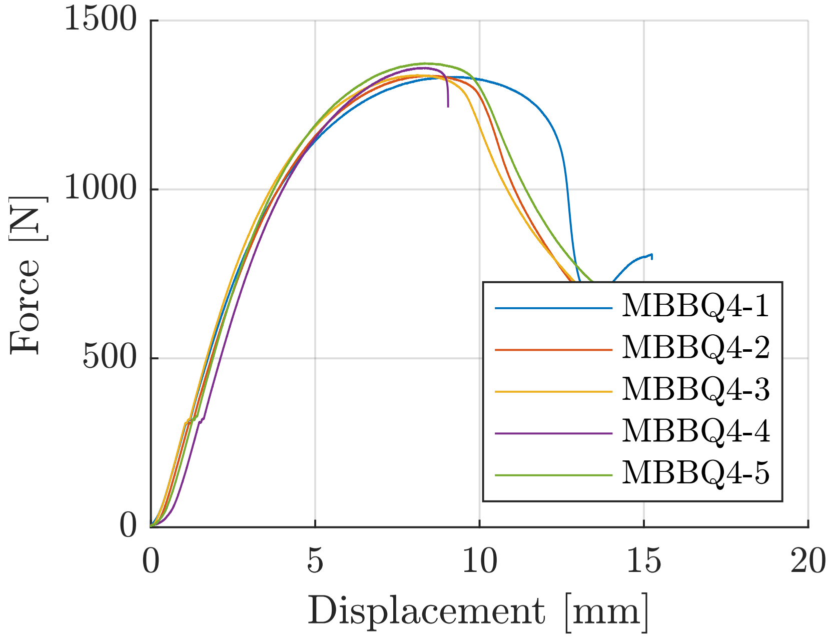


Figure 7.11: Results for the bilinear MBB benchmark tests.

Four of the specimens failed due to buckling as seen in Figure 7.12, where the middle two supporting branches are giving in, resulting in the whole specimen shifting to the side. This was not the wanted result, but it managed to withstand the force applied in the optimization. The strength of the test geometry was therefore also underestimated here. The specimen MBBQ4-4 did not buckle and failed, as the ones for the MBB benchmark with quadratic elements. This indicates that the buckling load and the fracture load are almost the same.

Figure 7.12: Buckling of the bilinear MBB benchmark test.

The point where the force displacement curves get non-linear are calculated as described in Section 7.3. The results are 878 N for the 2.5% displacement and 985 N for the 5% displacement. This is slightly lover than for the quadratic elements.

# 8 Discussion

The material properties used throughout the project are based on the experimental testing described in Section 3. It was not possible to test all the material properties for both the Smooth PA and CCF material. The missing properties are thus based on data sheets and articles, where the materials are described.
A lot of different 3D-print settings have an impact on the material properties. To get precise properties it is thus necessary to test all the material properties with the specific print settings. The properties used during the optimization can therefore vary from the manufactured parts.
The material properties for the Smooth PA are expected to be accurate since both the Young's moduli and tensile strength values obtained by the test, match the results given in the data sheet. The error from not testing the shear and compression properties is thus expected to be low.
The specimens used for testing the CCF follow the geometry given in DS/EN ISO 527-5. This specimen is designed for laminated fiber composites manufactured using traditional composite manufacturing techniques, such as filament winding or pultrusion. They are therefore not optimal for testing continuous fiber 3D-printed specimens.
These problems arise due to two important factors for 3D-printed parts, which are the minimum fiber length and minimum fiber bend radius as described in Section 3.1.5. When manufacturing the CCF test specimens in the 90° direction it is not possible to fulfill both of the two factors. The specimen is therefore printed with a continuous fiber path running across the layer in a S-shape. The fiber bend radius is thus small which yields manufacturing difficulties resulting in uneven fiber placement.
Furthermore results from Azarov et al. (2019) show that the max strength and Young's modulus are increased with the number of fiber layers. A more thorough material testing of the CCF material is thus recommended, in order to fully specify the material properties. This should include a study of all the material properties including compression and shear. The properties used here for shear and compression in the fiber direction, are obtained from tests in literature, which use other matrix materials. The properties in the fiber direction mostly depend upon the fiber and thus they are comparable.

The DMO makes it possible to easily implement the fiber orientations in the Aura slicing software by the use of masks. Even though there are a lot of benefits by using the DMO, it is not possible to utilize the full design freedom of the FFF 3D-printing process, due to the limitations of the predefined candidate materials. The best design which is possible to manufacture using the fiber reinforced FFF 3D-printing process, will thus almost never be included in the feasible solutions for the DMO.

The DMO with strength constraints as introduced by Lund (2018) penalizes the intermediate densities hard. This is a problem when density filters are introduced because they will result in intermediate densities. Due to the excessive penalization of intermediate densities it cannot converge to a feasible solution in many cases. It is thus not a suitable method for this application.

Two different solutions have thus been proposed, which either is to remove the filters or to remove some of the penalization of the intermediate densities. Both methods have proven to yield comparable results, but when the filters are removed the minimum length scale is define by the element size. This is problematic due to manufacturability and thus it requires post processing.
Especially for the continuous fiber reinforced material the generated results need severe post processing in order to make the results possible to manufacture. This post processing adds additional material to the geometry and thus it is altered.
It would be better to include all the manufacturing constraints in the optimization in order to alleviate this post processing step, but it can be difficult to achieve. The amount of post processing can although be reduced by introducing filtering as done for the bilinear element as discussed above.
This makes the bilinear element formulation favorable, because it generates manufacturable results. The bilinear element formulation also generates less discrete results, which can be a benefit for post processing the results.

In order to evaluate how well the optimization compares to real 3D-printed structures, the results for the Smooth PA MBB-beam benchmark of the two element formulations have been tested experimentally. The experimental results for both element formulations show an underestimation of the strength. This could be due to the added material from the post processing of the optimized geometries.
Another fact that influences the results is the linear elastic assumption of the material properties. The real material will deform plastically at high stresses as determined in Section 3.3. This redistributes the load and thus a linear elastic material assumption will underestimate the strength.
It is though seen from the test that the structure starts to behave non-linear at around 1000 N, which is the predicted load bearing capacity from the optimization. It is thus assessed that the prediction of the failure point is sufficiently accurate.
It should though be noted that the optimization does not include a buckling constraint. This is a problem since topology optimized geometries typically consist of thin bars that are loaded in compression or tension. This is seen during the test since four of the specimens using the bilinear elements buckled. This buckling concern is also the reason why the L-bracket has not been tested. This limitation is thus a major drawback and care has to be taken in order to avoid this problem.

# 9 Conclusion

The conclusion will answer the problem formulation which is:
*How do fiber reinforced FFF 3D-printed materials behave structurally and how can they be used to improve parts in combination with simultaneous strength constrained topology and fiber orientation optimization?*

The two fiber reinforced materials Smooth PA and continuous carbon fibers with CFC PA (CCF) are tested in order to determine the structural material properties. The material properties from Table 3.7 and 3.9 are determined based on tensile tests and different sources. These material properties are used throughout the optimization. This furthermore ensures that the material properties match the material, which is used for the experimental validation.

Different fiber optimization methods are evaluated, and the DMO is implemented. This method combines strength based topology and fiber angle optimization, with a minimum amount of post processing needed, in order to manufacture the optimized part on a FFF 3D-printer. The DMO method has the limitation that it does not use the full design freedom of the 3D-printing process, because of the discrete fiber angles which are introduced.

The DMO method is implemented based on the formulation by Lund (2018). This formulation results in high failure indices between candidate materials, due to the added filtering and excessive penalization of intermediate densities. Two method are thus proposed and implemented to overcome the problem. The first method is to remove the excessive penalization by calculating the failure indices for each material individually and not summing them for each element as proposed by Lund (2018). The second method is to remove the filtering. This although requires the use of quadratic elements in order to avoid checkerboarding.

Both methods are evaluated through multiple numerical tests of different benchmarks problems and materials. The bilinear element formulation without summing the failure indices yields more favorable results because the filtering ensures a minimum length scale. This results in less post processing. The quadratic formulation needs more post processing in order to make the result manufacturable, thus the optimized geometry is altered.

Finally the methods have been validated experimentally based on the results from the numerical tests of the MBB-beam using Smooth PA. The results from the tests showed an underestimation of the strength for both tests, which was expected due the added material from the post processing and the linear material model as discussed in Section 8. The optimization results are thus assessed to be comparable to the results from the experimental testing.

Both methods can thus be used to improve fiber reinforced FFF 3D-printed parts, through simultaneous strength constrained topology and fiber orientation optimization. It should though be noted that the bilinear formulation is recommended due to the minimum length scale ensure by the applied filter.

# 10 Future work

Throughout this chapter different solutions to some of the problems encountered throughout this project will be discussed. This includes problems with the choice of the DMO for optimizing the fiber orientation. Furthermore the extension to 3D is discussed as well as the possibility to include multiple layers in the optimization. In order to get manufacturable results for the CCF it is necessary to include the minimum fiber length as a constraint in the optimization. The material properties for the CCF should also be investigated further in order to improve the properties perpendicular to the fiber orientation.

As mentioned in Section 8 the DMO method does not fully utilize the design freedom of the FFF 3D-printing process. This is due to the limitations of the candidate materials introduced to specify the fiber angles. Neither does it remove the need for post processing for the CCF, since the minimum fiber length is not necessarily satisfied.
Another method that could be implemented to reduce this problem is the contour placement method.This method will not result in the optimal solution, but could give good results when comparing to the DMO. It is observed that the DMO places the fiber orientation roughly in the direction of the contour of the geometry. It is therefore expected that the contour placement method yields a similar result.

In order to fully utilize the design freedom of the FFF 3D-printing method the CFAO method could be implemented. The CFAO method is not limited by discrete angles like the DMO and it is therefore possible to reach a better optimum. The infinite number of possible fiber angles are also possible to manufacture by the use of the FFF 3D-printing process. In order to implement the CFAO method, post processing is necessary in order to convert the individual element fiber directions to continuous fiber paths. Furthermore these have to be imported into the slicing software in order to create the g-code.
The CFAO method also makes it possible to expand from 2D to 3D fiber orientations. This will require that the whole optimization is expanded to three dimensions. 3D topology and fiber orientation optimization is able to fully utilize the capabilities of the 3D-printing process. In order to print these geometries it must be combined with non-planar slicing. Non-planar slicing and 3D fiber orientations could expand the usability of fiber 3D-printing and help to resolve the problem, with FFF 3D-printing being weaker in the direction of the layers. Non-planar slicing is though still in its development and primarily used for smoothing surfaces to avoid staircasing (Ahlers et al. 2019). It is though yet to be implemented commercially.

The DMO method could also be expanded to include more layers in the optimization. This could allow for different fiber paths in each layer, which would help to better transfer multidirectional loads. This is especially important for the CCF, which is highly orthotropic. Multi layer DMO will therefore give better results for orthotropic materials. It might also reduce the problems seen in Figure 6.7b, where the optimization places two materials with intermediate densities in the same elements. It would instead be possible to place these materials in different layers. This method could also be used together with FFF 3D-printing, because different layers can be defined with different fiber orientations in the slicer.

In order to ensure that the results using CCF can be manufactured a constraint should be added to ensure the minimum fiber length. All the results obtained for the CCF are not possible to manufacture due to this constraint not being fulfilled. The problem arises especially when the thin branches do not follow the fiber direction exactly since this would break up the fiber.

As discussed in Section 8 due to the many variables affecting the material properties a more thorough material study is recommended. This is especially the case for the CCF where it is expected that the properties perpendicular to the fiber orientation can be improved significantly by tuning the settings. In order to get more precise material properties for the CCF material the test specimen should be redesign to be easily printable in the 90° direction. By implementing a wider specimen the fibers have a better chance of aligning and the edge effects, where the fibers do not fulfill the minimum fiber bend radius can be cut off. This will result in better alignment of the fibers.
The method used in order to determine the Poisson's ratio also includes a lot of possible errors. The Poisson's ratio for the CCF test specimens are also only defined by one data point. Another way to determine the Poisson's ratio would therefore be beneficial in order to lower the sources of errors. The most optimal way would be to test multiple test specimens with the use of two extensometers, in order to measure the strain in both the longitudinal and transverse direction.

Most structural components are loaded more than one time, it would therefore be beneficial to investigate fatigue as a part of the optimization. Combining fatigue optimization with FFF 3D-printed continuous fiber could make 3D-printing more usefull in for example production equipment, where the optimized parts will go through many load cycles.
Another strength criteria which could be investigated is buckling. This is a very important aspect since many topology optimized structures fail due to buckling as also seen during the tests of the MBB benchmark with the bilinear elements.

# Bibliography


3D-Experten (2022). *Anisoprint prices.* URL: https://3deksperten.dk/3d-printere.html/fdm?manufacturer=5821 (visited on 2022).

Aage, Niels et al. (2017). "Giga-voxel computational morphogenesis for structural design". In: *Nature* 550.7674, pp. 84–86. ISSN: 0028-0836. DOI: 10.1038/nature23911.

Addifab (2022). *Next level product development for unseen injection mold tooling.* URL: https://www.addifab.com/technology (visited on 05/27/2022).

Adumitroaie, Adi et al. (2019). "Novel Continuous Fiber Bi-Matrix Composite 3-D Printing Technology". In: *Materials 2019* 12.3011. DOI: https://doi.org/10.3390/ma12183011.

Ahlers, Daniel et al. (2019). "3D Printing of Nonplanar Layers for Smooth Surface Generation". In: *2019 IEEE 15th International Conference on Automation Science and Engineering (CASE)*, pp. 1737–1743.

Anisoprint (2020a). *CFC PA.* URL: https://www.designconsulting.com.au/Brochures/Technical%5C%20Data%5C%20sheet_CFC%5C%20PA.pdf (visited on 04/04/2022).

— (2020b). *Smooth PA.* URL: https://ballistic-bit.com/smooth-pa-filament (visited on 03/07/2022).

— (2022a). *Anisoprint Reinforcing Materials: Composite Carbon Fiber (CCF) and Composite Besalt Fiber (CBF).* URL: https://ballistic-bit.com/Files/Material-Datasheet_CCF-CBF-PETG.pdf (visited on 05/16/2022).

— (2022b). *Desktop Anisoprinting.* URL: https://anisoprint.com/solutions/desktop/ (visited on 2022).

Azarov, Andrey V. (2021). *Implemented Codes.* URL: https://github.com/anisoprint/MKA-firmware/blob/dev/GCodes.md.

Azarov, Andrey V. et al. (2019). "Composite 3D printing for the small size unmanned aerial vehicle structure". In: *Composites Part B: Engineering* 169, pp. 157–163. ISSN: 1359-8368. DOI: https://doi.org/10.1016/j.compositesb.2019.03.073.

Bellini, Anna and Selçuk Güçeri (2003). "Mechanical characterization of parts fabricated using fused deposition modeling". In: *Rapid Prototyping Journal* 9, pp. 252–264. DOI: https://doi.org/10.1108/13552540310489631.

Bendsøe, Martin P. (1989). “Optimal shape design as a material distribution problem”. In: *Structural Optimization* 1, pp. 193–202. DOI: https://doi.org/10.1007/BF01650949.

Bendsøe, Martin P., J. M. Guedes, et al. (1994). “An analytical model to predict optimal material properties in the context of optimal structural design”. In: *Journal of Applied Mechanics, Transactions ASME* 61. DOI: https://doi.org/10.1115/1.2901581.

Bendsøe, Martin P. and Noboru Kikuchi (1988). “Generating optimal topologies in structural design using a homogenization method”. In: *Computational Methods in Applied Mechanics and Engineering* 71. DOI: https://doi.org/10.1016/0045-7825(88)90086-2.

Bendsøe, Martin P. and Ole Sigmund (1999). “Material interpolation schemes in topology optimization”. In: *Archive of Applied Mechanics* 69. DOI: https://doi.org/10.1007/s004190050248.

Blaber, Justin and Antonia Antoniou (2017). *Ncorr Instruction Manual.* Georgia Institute of Technology. URL: http://www.ncorr.com/index.php/downloads (visited on 2022).

Bourdin, Blaise (2001). “Filters in topology optimization”. In: *International Journal for Numerical Methods in Engineering* 50.9, pp. 2143–2158. DOI: https://doi.org/10.1002/nme.116.

Braibant, Vincent and Claude Fleury (1985). “An approximation-concepts approach to shape optimal design”. In: *Computer methods in applied mechanics and engineering* 53.2. DOI: https://doi.org/10.1016/0045-7825(85)90002-7.

Bruggi, Matteo (2008). “An alternative approach to stress constraints relaxation”. In: *Structural Multidisciplinary Optimization* 36. DOI: https://doi.org/10.1007/s00158-007-0203-6.

Bruns, Tyler E. and Daniel A. Tortorelli (2001). “Topology optimization of non-linear elastic structures and compliant mechanisms”. In: *Computer Methods in Applied Mechanics and Engineering* 190. DOI: https://doi.org/10.1016/S0045-7825(00)00278-4.

Cheng, Gengdong and X. Guo (1997). “$\varepsilon$-relaxed approach in structural topology optimization”. In: *Structural Optimization* 13. DOI: https://doi.org/10.1007/BF01197454.

Clausen, Anders and Erik Andreassen (2017). “On filter boundary conditions in topology optimization”. In: *Structural and Multidisciplinary Optimization* 56. DOI: https://doi.org/10.1007/s00158-017-1709-1.

Cook, Robert D. et al. (2002). *Concepts and applications of finite element analysis.* ISBN: 978-0-471-35605-9.

DesignFusion (2022). *Industrial Composite 3D Printing.* URL: https://www.designfusion.build/markforged/markforged-industrial-composite-3d-printers (visited on 04/25/2022).

Duysinx, Pierre and Martin P. Bendsøe (1998). "Topology Optimization of Continuum Structures with Local Stress Constraints". In: *International Journal for Numerical Methods in Engineering* 43. DOI: https://doi.org/10.1002/(SICI)1097-0207(19981230)43:8<1453::AID-NME480>3.3.CO;2-U.

Fedulov, Boris et al. (2021). "Optimization of parts manufactured using continuous fiber three-dimensional printing technology". In: *Composites Part B: Engineering* 227. ISSN: 1359-8368. DOI: https://doi.org/10.1016/j.compositesb.2021.109406.

Formlabs (2022). *Guide to Stereolithography (SLA) 3D Printing.* URL: https://formlabs.com/blog/ultimate-guide-to-stereolithography-sla-3d-printing/ (visited on 2022).

Gadegaard, Frederik Juel and Jan Thuesen (2021). *Topology optimization of 3D-printed structures.*

GE Aviation (2018). *New manufacturing milestone: 30,000 additive fuel nozzles.* URL: https://www.ge.com/additive/stories/new-manufacturing-milestone-30000-additive-fuel-nozzles?fbclid=IwAR0_bmNNkbLNzhaKIxNofll-XPiiLMQ1-XSu6bS_sdGODtU3zcOrozHVewo (visited on 2022).

Gibiansky, Leonid V. and Ole Sigmund (2000). "Multiphase composites with extremal bulk modulus". In: *Journal of the Mechanics and Physics of Solids* 48.3, pp. 461–498. ISSN: 0022-5096. DOI: https://doi.org/10.1016/S0022-5096(99)00043-5.

Groenwold, Albert A. and Raphael T. Haftka (2006). "Optimization with non-homogeneous failure criteria like Tsai–Wu for composite laminates". In: *Structural and Multidisciplinary Optimization* 32.3, pp. 183–190. DOI: https://doi.org/10.1007/s00158-006-0020-3.

Guest, J. K., J. H. Prévost, and T. Belytschko (2004). "Achieving minimum length scale in topology optimization using nodal design variables and projection functions". In: *International Journal for Numerical Methods in Engineering* 61. DOI: https://doi.org/10.1002/nme.1064.

Hoglund, Robert M. (2016). "An Anisotropic Topology Optimization Method For Carbon Fiber-Reinforced Fused Filament Fabrication". In: *Graduate Faculty of Baylor University.*

Hoglund, Robert M. and Douglas E. Smith (2015). "Non-isotropic material distribution topology optimization for fused deposition modeling production". In: *Department of Mechanical Engineering Baylor University.*

Hvejsel, Christian Frier and Erik Lund (2011). "Material interpolation schemes for unified topology and multi-material optimization". In: *Structural and Multidisciplinary Optimization* 43, pp. 811–825. DOI: https://doi.org/10.1007/s00158-011-0625-z.

Jiang, Delin, Robert M. Hoglund, and Douglas E. Smith (2019). "Continuous Fiber Angle Topology Optimization for Polymer Composite Deposition Additive Manufacturing Applications". In: *Fibers* 7. DOI: https://doi.org/10.3390/fib7020014.

Jones, Robert M. (1999). *Mechanics of composite materials.* 2nd ed.

Kim, C. W. et al. (1994). "On the Failure Indices of Quadratic Failure Criteria for Optimal Stacking Sequence Design of Laminated Plate". In: *Applied Composite Materials* 1, pp. 81–85. DOI: https://doi.org/10.1007/BF00567214.

Le, Chau et al. (2010). "Stress-based topology optimization for continua". In: *Structural Multidisciplinary Optimization* 41. DOI: https://doi.org/10.1007/s00158-009-0440-y.

Lund, Erik (2018). "Discrete Material and Thickness Optimization of laminated composite structures including failure criteria". In: *Structural and Multidisciplinary Optimization* 57, pp. 2357–2375. DOI: https://doi.org/10.1007/s00158-017-1866-2.

Markforged (2022). *Wärtsilä.* URL: https://markforged.com/resources/case-studies/w%5C%C3%5C%A4rtsil%5C%C3%5C%A4-case-study (visited on 2022).

Mirzendehdel, Amir, Behzad Rankouhi, and Krishnan Suresh (2017). "Strength-Based Topology Optimization for Anisotropic Parts". In: *Additive Manufacturing* 19. DOI: 10.1016/j.addma.2017.11.007.

Nomura, Tsuyoshi et al. (2014). "General topology optimization method with continuous and discrete orientation design using isoparametric projection". In: *International journal for numerical methods in engineering* 101, pp. 571–605. DOI: https://doi.org/10.1002/nme.4799.

Oest, Jacob and Erik Lund (2017). "Topology optimization with finit-life fatigue constraints". In: *Structural Multidisciplinary Optimization* 56. DOI: https://doi.org/10.1007/s00158-017-1701-9.

Papapetrou, Vasileios S., Chitrang Patel, and Ali Y. Tamijani (2020). "Stiffness-based optimization framework for the topology and fiber paths of continuous

fiber composites". In: *Composites Part B* 183.
DOI: https://doi.org/10.1016/j.compositesb.2019.107681.

Pedersen, Pauli (1998).
"Some general optimal design results using anisotropic, power law nonlinear elasticity".
In: *Structural Optimization* 15.2, pp. 73–80.

Ringertz, U. T. (1993). "On finding the optimal distribution of material properties".
In: *Structural Optimization* 5, pp. 265–267.
DOI: https://doi.org/10.1007/BF01743590.

Sigmund, Ole (Jan. 1994). "Design of Material Structures Using Topology Optimization".
PhD thesis.

— (2007). "Morphology-based black and white filters for topology optimization".
In: *Structural and Multidisciplinary Optimization* 33.
DOI: https://doi.org/10.1007/s00158-006-0087-x.

Sigmund, Ole and S. Torquato (1997). "Design of materials with extreme thermal expansion using a three-phase topology optimization method".
In: *Journal of the Mechanics and Physics of Solids* 45.6, pp. 1037–1067. ISSN: 0022-5096.
DOI: https://doi.org/10.1016/S0022-5096(96)00114-7.

Silva, Gustavo Assis da, André Teófilo Beck, and Ole Sigmund (2019). "Stress-constrained topology optimization considering uniform manufacturing uncertainties".
In: *Computer Methods in Applied Mechanics and Engineering* 344.
DOI: https://doi.org/10.1016/j.cma.2018.10.020.

Sørensen, Rene and Erik Lund (2015).
"In-plane material filters for the discrete material optimization method".
In: *Structural and multidisciplinary optimization.*
DOI: 10.1007/s00158-015-1257-5.

Sørensen, Søren N., Rene Sørensen, and Erik Lund (2014). "DMTO - a method for discrete material and thickness optimization of laminated composite structures".
In: *Structural and multidisciplinary optimization* 50, pp. 25–47.
DOI: https://doi.org/10.1007/s00158-014-1047-5.

Steffensen, Daniel Woldbye et al. (2019). "Gåmekanisme". In: *Det Ingeniør- og Naturvidenskabelige Fakultet, Maskin og Produktion, Aalborg Universitet.*

Stegmann, Jan and Erik Lund (2005).
"Discrete material optimization of general composite shell structures".
In: *International journal for numerical methods in engineering* 62.14.
DOI: 10.1002/nme.1259.

Stolpe, Mathias and Krister Svanberg (2001).
"An alternative interpolation scheme for minimum compliance topology optimization".

In: *Structural and Multidisciplinary Optimization* 22, pp. 116–124.
DOI: https://doi.org/10.1007/s001580100129.

Svanberg, Krister (1987).
"The method of moving asymptotes - a new method for structural optimization".
In: *International journal for numerical methods in engineering* 24.2.
DOI: https://doi.org/10.1002/nme.1620240207.

— (2007). *MMA and GCMMA - two methods for nonlinear optimization.*
URL: https://people.kth.se/~krille/mmagcmma.pdf (visited on 12/20/2021).

Sved, G. and Z. Ginos (1968). "Structural optimization under multiple loading".
In: *International Journal of Mechanical Sciences* 10.10, pp. 803–805.
DOI: https://doi.org/10.1016/0020-7403(68)90021-0.

Varotsis, Alkaios Bournias (2022). *What is SLS 3D printing?*
URL: https://www.hubs.com/knowledge-base/what-is-sls-3d-printing/
(visited on 2022).

Wang, Fengwen, Boyan Stefanov Lazarov, and Ole Sigmund (2011). "On projection methods, convergence and robust formulations in topology optimization".
In: *Structural and Multidisciplinary Optimization* 43.
DOI: https://doi.org/10.1007/s00158-010-0602-y.

Weldeyesus, Alemseged and Mathias Stolpe (June 2016).
"Free material optimization for laminated plates and shells".
In: *Structural and Multidisciplinary Optimization* 53.
DOI: 10.1007/s00158-016-1416-3.

Weldeyesus, Alemseged Gebrehiwot (2014).
*Models and Methods for Free Material Optimization.* Frederiksborgvej 399 Building 118 4000 Roskilde Denmark: Technical University of Denmark. ISBN: 978-87-92896-89-6.

Xu, S., Yuanwu Cai, and Gengdong Cheng (2010).
"Volume preserving nonlinear density filter based on heaviside functions".
In: *Structural and Multidisciplinary Optimization* 41.
DOI: https://doi.org/10.1007/s00158-009-0452-7.

Xu, S., Jiaqi Huang, et al. (2020). "Topology Optimization for FDM Parts Considering the Hybrid Deposition Path Pattern". In: *Micromachines* 11.
DOI: https://doi.org/10.3390/mi11080709.

Yao, Tianyun et al. (2020). "Tensile failure strength and separation angle of FDM 3D printing PLA material: Experimental and theoretical analyses".
In: *Composites Part B: Engineering* 188, p. 107894. ISSN: 1359-8368.
DOI: https://doi.org/10.1016/j.compositesb.2020.107894.

Zegard, Thomás and Glaucio H. Paulino (2016).
"Bridging topology optimization and additive manufacturing".

In: *Structural multidisciplinary Optimization* 53, pp. 175–192.
DOI: 10.1007/s00158-015-1274-4.

# Appendix

## A DIC parameters

| | SPA0V3-1 | SPA0V3-2 | SPA0V3-3 | SPA0V3-4 | SPA0V3-5 |
|---|---|---|---|---|---|
| Camera | BFS-U3-89S6M-C | BFS-U3-89S6M-C | BFS-U3-89S6M-C | BFS-U3-89S6M-C | BFS-U3-89S6M-C |
| Resolution | 4096x2160 | 4096x2160 | 4096x2160 | 4096x2160 | 4096x2160 |
| DIC Software | Ncorr | Ncorr | Ncorr | Ncorr | Ncorr |
| Cross correlation function | ZNSSD | ZNSSD | ZNSSD | ZNSSD | ZNSSD |
| Subset Size/Subset radius (pixels) | 40 | 40 | 40 | 40 | 40 |
| Subset spacing (pixels) | 3 | 3 | 3 | 3 | 3 |
| **Correlation values** | | | | | |
| Load step 1 (0N): (best;worst) | (0.0002;0.0010) | (0.0005;0.0149) | (0.0005;0.0053) | (0.0005;0.0037) | (0.0005;0.0064) |
| Load step 2 (Fmax): (best;worst) | (0.0005;0.0060) | (0.0011;0.0292) | (0.0013;0.0106) | (0.0016;0.0105) | (0.0014;0.0140) |
| **Displacement resolution [mm]** | | | | | |
| u, mean (std) | 0.1003 (0.0116) | 0.0677 (0.0065) | 0.0150 (0.0122) | 0.0266 (0.0132) | -0.0008 (0.0062) |
| v, mean (std) | -0.1825 (0.0092) | 0.0417 (0.0045) | -0.0167 (0.0042) | -0.0772 (0.0087) | -0.0448 (0.0074) |
| Strainsmoothening (radius) | 10 | 10 | 10 | 10 | 10 |
| **Strain resolution** $[\frac{\mu m}{m}]$ | | | | | |
| $\varepsilon_{xx}$, mean(std) | 14.74 (63.98) | -0.2321 (52.79) | -33.06 (46.58) | -31.83 (48.83) | 16.17 (45.40) |
| $\varepsilon_{yy}$, mean(std) | -28.29 (55.46) | -3.754 (42.63) | -22.33 (48.63) | -48.99 (48.79) | 27.98 (46.14) |
| $\varepsilon_{xy}$, mean(std) | -0.9801 (35.12) | -2.152 (31.24) | -4.389 (28.77) | -16.98 (31.59) | -20.00 (28.00) |
| Time between pictures [s] | 0.5 | 0.5 | 0.5 | 0.5 | 0.5 |

| | SPA90-1 | SPA90-2 | SPA90-3 | SPA90-4 | SPA90-5 |
|---|---|---|---|---|---|
| Camera | BFS-U3-89S6M-C | BFS-U3-89S6M-C | BFS-U3-89S6M-C | BFS-U3-89S6M-C | BFS-U3-89S6M-C |
| Resolution | 4096x2160 | 4096x2160 | 4096x2160 | 4096x2160 | 4096x2160 |
| DIC Software | Ncorr | Ncorr | Ncorr | Ncorr | Ncorr |
| Cross correlation function | ZNSSD | ZNSSD | ZNSSD | ZNSSD | ZNSSD |
| Subset Size/Subset radius (pixels) | 40 | 40 | 40 | 40 | 40 |
| Subset spacing (pixels) | 3 | 3 | 3 | 3 | 3 |
| **Correlation values** | | | | | |
| Load step 1 (0N): (best;worst) | (0.0003;0.0204) | (0.0003;0.0032) | (0.0003;0.0012) | (0.0003;0.0013) | (0.0003;0.0015) |
| Load step 2 (Fmax): (best;worst) | (0.0327;1.0887) | (0.0039;0.0493) | (0.0051;0.0778) | (0.0046;0.0777) | (0.0031;0.0531) |
| **Displacement resolution [mm]** | | | | | |
| u, mean (std) | -0.0483 (0.0118) | 0.0323 (0.0134) | -0.0167 (0.0102) | 0.0188 (0.0037) | -0.0657 (0.0061) |
| v, mean (std) | -0.0154 (0.0050) | 0.0367 (0.0094) | -0.0435 (0.0099) | -0.0317 (0.0028) | -0.0196 (0.0030) |
| Strainsmoothening (radius) | 10 | 10 | 10 | 10 | 10 |
| **Strain resolution** $[\frac{\mu m}{m}]$ | | | | | |
| $\varepsilon_{xx}$, mean(std) | -23.75 (39.99) | 25.70 (54.94) | -29.04 (43.04) | -12.35 (33.63) | -4.232 (53.02) |
| $\varepsilon_{yy}$, mean(std) | 30.54 (34.91) | 19.72 (75.29) | 6.238 (56.80) | 91.23 (47.48) | 8.983 (52.28) |
| $\varepsilon_{xy}$, mean(std) | 11.49 (26.09) | 9.103 (51.63) | -12.30 (28.57) | -0.8087 (28.28) | -10.38 (30.82) |
| Time between pictures [s] | 0.5 | 0.5 | 0.5 | 0.5 | 0.5 |

# B Optimization algorithm

During this Appendix the solver will be discussed. Different methods for solving the optimization problem will be presented and tested. This will result in a test of the different algorithms and the best will be chosen and used for the solving the benchmark problems.

## B.1 Linear programming

A linear programming problem can be formulated as given in Equation B.1.

$$\underset{x}{\text{minimize}} \quad f(\{x\}) = \{c\}^T\{x\} \tag{B.1a}$$

$$\text{s.t.} \quad [A]\{x\} = \{b\}; \{b\} \geq \{0\} \tag{B.1b}$$

$$\{x\} \geq \{0\} \tag{B.1c}$$

Any linear programming problem can be rewritten into this form. Inequality constraints are rewritten into equality constraints by using slack variables and surplus variables. In Equation B.2 it is shown, how a surplus variable ($s_i$) is introduced to rewrite the "≥type" constraint into an equality constraint. In Equation B.3 the same is done for a "≤type" constraint using slack variables. Both the surplus variables and the slack variables are required to be larger than or equal to 0 which adds an additional constraint in addition to the increased dimensionality of the optimization problem due to the added variable.

$$a_{i1}x_1 + a_{i2}x_2 + ... + a_{i,n}x_n \geq b_i, \text{ for } i = 1,2,...,m \tag{B.2a}$$

$$a_{i1}x_1 + a_{i2}x_2 + ... + a_{i,n}x_n - s_i = b_i, \text{ for } i = 1,2,...,m \tag{B.2b}$$

$$a_{i1}x_1 + a_{i2}x_2 + ... + a_{i,n}x_n \leq b_i, \text{ for } i = 1,2,...,k \tag{B.3a}$$

$$a_{i1}x_1 + a_{i2}x_2 + ... + a_{i,n}x_n + s_i = b_i, \text{ for } i = 1,2,...,k \tag{B.3b}$$

The optimization problem which is to be solved though is nonlinear, thus this method cannot be used directly. Therefore the original problem can be linearized by approximating the original problem, with a first order Taylor series. The linearized problem is solved and the solution is then used as the linearization point for a new linear optimization problem. This is continued until the solution converges. Due to the sequential nature this method is called sequential linear programming (SLP).

It is necessary to linearize both the objective function and the constraints to formulate the problem in the standard form. Due to this linearization the subproblem becomes convex and thus if an optimum exists it is a global optimum. It might though not be a minimum of the non-linear function. The Taylor series for linearization in the point (a) is given in

Equation B.4. For the objective function the constant terms are ignored since they do not influence the optimal solution.

$$\tilde{f}_d(x) = f(a) + \sum_{i=1}^{n} \left.\frac{\partial f}{\partial x_i}\right|_a \cdot (x_i - a_i) \tag{B.4}$$

This linear approximation is only valid around the point of linearization thus move limits should be applied. These move limits should be adaptive and tightened, when the optimal solution is reached since it tends to oscillate between different solutions. When the solution does not oscillate the move limits are widened since they are not necessary.

## B.2 Linearization

Instead of linearizing the problem with respect to the design variables it can also be linearized with respect to the reciprocal design variables. This has shown to be beneficial in structural size optimization since the constraints are generally less nonlinear, with respect to the reciprocal design variables. Furthermore the objective function becomes highly nonlinear, with respect to the reciprocal design variables which prohibits large design changes (Braibant and Fleury 1985). This is also true for the stress constrained optimization problem considered here, since the stresses are generally less nonlinear with respect to the reciprocal densities.
The first order Taylor series with respect to the reciprocal variables is given in Equation B.5.

$$\tilde{f}_r(x) = f(a) + \sum_{i=1}^{n} \left.\frac{\partial f}{\partial x_i}\right|_a \frac{a_i}{x_i}(x_i - a_i) \tag{B.5}$$

The problem with linearizing, with respect to the reciprocal design variables, is that it is nonconservative. Therefore when approximating the constraints the feasible solution space might be expanded, thus the solution of the linearized problem might yield unfeasible solutions.
To overcome this problem the direct and reciprocal linearization schemes can be combined. The most conservative linearization scheme for each design variable is used and thus the most conservative linearization is obtained. In order to chose the appropriate linearization scheme for each variable the sign of the gradient is used as given in Equation B.6 and Equation B.7.

Objective function:

$$\text{Direct linearization if} \quad \left.\frac{\partial f}{\partial x_i}\right|_a > 0 \tag{B.6a}$$

$$\text{Reciprocal linearization if} \quad \left.\frac{\partial f}{\partial x_i}\right|_a < 0 \tag{B.6b}$$

Constraint functions:

$$\text{Direct linearization if} \quad \left.\frac{\partial g}{\partial x_i}\right|_a < 0 \tag{B.7a}$$

$$\text{Reciprocal linearization if} \quad \left.\frac{\partial g}{\partial x_i}\right|_a > 0 \tag{B.7b}$$

Due to these definitions the resulting subproblem will be both conservative and convex.(Braibant and Fleury 1985)

## B.3 Method of moving asymptotes

In the method of moving asymptotes the linearization scheme is a generalization of the linearization schemes presented above. The linearization is done with respect to $(x_j - L_j)^{-1}$ or $(U_j - x_j)^{-1}$ depending on the sign of the derivative. The parameters $L_j$ and $U_j$ are referred to as the moving asymptotes, and they are normally changed between each iteration such that $L_j < x_j < U_j$. In the special case that $L_j = 0$ and $U_j = \infty$ the convex linearization is achieved while $L_j = -\infty$ and $U_j = \infty$ results in the direct linearization. (Svanberg 1987)
A first order approximation of the objective function and the constraints is given in Equation B.8 utilizing the definitions in Equation B.9. The objective function is defined by $i = 0$, while the constraint functions are defined by $g_i = f_i \leq 0$ for $i > 0$.

$$f_i(x) = r_i + \sum_{j=1}^{n} \left( \frac{p_{ij}}{U_j - x_j} + \frac{q_{ij}}{x_j - L_j} \right) \tag{B.8}$$

where:

$$p_{ij} = \begin{cases} (U_j - a_j)^2 \left.\dfrac{\partial f_i}{\partial x_j}\right|_a, & \text{if } \left.\dfrac{\partial f_i}{\partial x_j}\right|_a > 0 \\ 0, & \text{if } \left.\dfrac{\partial f_i}{\partial x_j}\right|_a \leq 0 \end{cases} \tag{B.9a}$$

$$q_{ij} = \begin{cases} 0, & \text{if } \left.\dfrac{\partial f_i}{\partial x_j}\right|_a \geq 0 \\ -(a_j - L_j)^2 \left.\dfrac{\partial f_i}{\partial x_j}\right|_a, & \text{if } \left.\dfrac{\partial f_i}{\partial x_j}\right|_a < 0 \end{cases} \tag{B.9b}$$

$$r_i = f_i(a) - \sum_{j=1}^{n} \left( \frac{p_{ij}}{U_j - a_j} + \frac{q_{ij}}{a_j - L_j} \right) \tag{B.9c}$$

As it is seen in Equation B.8 the function has a singularity at $U_j - x_j$ and at $x_j - L_j$. In order to avoid this problem the move limits given in Equation B.10 are applied.

$$L_j < \alpha_j < x_j < \beta_j < U_j \tag{B.10a}$$

$$\alpha_j = L_j + 0.1 \cdot (a_j - L_j) \tag{B.10b}$$

$$\beta_j = U_j - 0.1 \cdot (U_j - a_j) \tag{B.10c}$$

The second derivative of $f_i(x)$ is given in Equation B.11. Since $p_{ij} \geq 0$ and $q_{ij} \geq$, the second derivative will always be positive thus $f_i(x)$ is a convex function. It can also be seen that the second derivative increases when $L_j$ and $U_j$ are chosen closer, this increases the conservativeness of the approximation. When the solution is approached the asymptotes are tightened.

$$\frac{\partial^2 f_i}{\partial x_j^2} = \frac{2p_{ij}}{(U_j - x_j)^3} + \frac{2q_{ij}}{(x_j - L_j)^3} \tag{B.11}$$

The asymptote values are calculated using Equation B.12, where $\gamma$ is given in Equation B.13. This tightens the asymptotic values, when the convergence is not monotonic while it expands the asymptotic values when convergence is monotonic.

$$L_j^{(k)} = x_j^{(k)} - \gamma_j^{(k)}(x_j^{(k-1)} - L_j^{(k-1)}) \tag{B.12a}$$
$$U_j^{(k)} = x_j^{(k)} + \gamma_j^{(k)}(U_j^{(k-1)} - x_j^{(k-1)}) \tag{B.12b}$$

$$\gamma_j^{(k)} = \begin{cases} 0.7, & \text{if } (x_j^{(k)} - x_j^{(k-1)})(x_j^{(k-1)} - x_j^{(k-2)}) < 0 \\ 1.2, & \text{if } (x_j^{(k)} - x_j^{(k-1)})(x_j^{(k-1)} - x_j^{(k-2)}) > 0 \\ 1, & \text{if } (x_j^{(k)} - x_j^{(k-1)})(x_j^{(k-1)} - x_j^{(k-2)}) = 0 \end{cases} \tag{B.13}$$

Since information from the last two iterations is needed to calculate $\gamma$ the first two iterations the asymptotic values are calculated using Equation B.14.

$$L_j^{(k)} = x_j^{(k)} - 0.5(\bar{x}_j - \underline{x}_j) \tag{B.14a}$$
$$U_j^{(k)} = x_j^{(k)} + 0.5(\bar{x}_j - \underline{x}_j) \tag{B.14b}$$

In addition the boundary values given in Equation B.15 are used for the asymptotic values.

$$L_j^{(k)} \leq x_j^{(k)} - 0.01(\bar{x}_j - \underline{x}_j) \tag{B.15a}$$
$$L_j^{(k)} \geq x_j^{(k)} - 10(\bar{x}_j - \underline{x}_j) \tag{B.15b}$$
$$U_j^{(k)} \geq x_j^{(k)} + 0.01(\bar{x}_j - \underline{x}_j) \tag{B.15c}$$
$$U_j^{(k)} \leq x_j^{(k)} + 10(\bar{x}_j - \underline{x}_j) \tag{B.15d}$$

Hereby the original problem which is only defined implicitly through a finite element analysis is approximated by an explicit problem. An appropriate solver has to be chosen for solving the problem.

## B.4 Dual solver

Since the optimization problem has many variables a dual solver is typically used. The basic idea behind the dual solver is to define another optimization problem, with fewer variables which is solved. Based on the solution of the dual problem the solution of the original (primal) problem can be calculated easily. In order to setup the dual problem the primal problem has to be separable and convex which are both satisfied for the linearized problem defined in the method of moving asymptotes in Equation B.8.

For the sake of simplicity the method will be explained here based on an equality constraint, but it can be expanded to include inequality constraints as well. The optimization problem considered is defined in Equation B.16.

$$\underset{x}{\text{minimize}} \quad f(x) \tag{B.16a}$$

$$\text{st.} \quad h_i(x) = 0; \quad i = 1 \text{ to } m \tag{B.16b}$$

The Lagrangian function is setup in Equation B.17.

$$L(x,\lambda) = f(x) + \sum_{i=1}^{m} \lambda_i h_i(x) \tag{B.17}$$

In order to solve minimize the Lagrangian function the Karush-Kuhn-Tucker (KKT) necessary conditions are set up. These conditions are given in Equation B.18.

$$\frac{\partial L}{\partial x} = \frac{\partial f}{\partial x} + \sum_{i=1}^{m} \lambda_i \frac{\partial h_i}{\partial x} = 0 \tag{B.18a}$$

$$\frac{\partial L}{\partial \lambda} = h = 0 \tag{B.18b}$$

Since the problem is separable Equation B.18a can be rewritten in such a way, that all the design variables $x$, are a function of the Lagrange multipliers, $\lambda$. The design variables are thus given as a function of the Lagrange multipliers and these definitions can be inserted in the original Lagrange function. Thereby the number of variables has been reduced to the number of Lagrange multipliers which is equal to the number of constraints. The resulting function is the auxillary function given in Equation B.19.

$$\phi(\lambda) = L(x(\lambda),\lambda) = f(x(\lambda)) + \sum_{i=1}^{m} \lambda_i h_i(x(\lambda)) \tag{B.19}$$

The primal problem is a convex minimization problem and thus the hessian is positive definite. It can thus be proven that the hessian of the dual problem is negative definite and when maximizing the dual problem it will yield the same solution as minimizing the primal function.

The dual problem which is to be solved is thus the unconstrained maximization problem stated in Equation B.20. The solution to the dual problem is identical to the solution of the primal problem, but the dimension of the problem has been reduced to number of constraints. When this maximization problem is solved the Lagrange multipliers can be inserted into the expressions for the original variables derived from Equation B.18a.

$$\underset{\lambda}{\text{maximize}} \quad \phi(\lambda) \tag{B.20}$$

## B.5 Comparison of optimization algorithms

In order to choose the most suitable algorithm they have been tested and compared. The two algorithms that will be compared are the method of moving asymptotes and sequential linear programming. The problem which will be solved is the MBB-beam as described in Section 5.1. The problem will be solved on a server with two 10-core Intel Xeon Gold 5115 processors at 2.4 GHz.

### B.5.1 Implementation of the optimization algorithms

The implementation for the MMA is based on Svanberg (2007) but minor efficiency improvements have been implemented as proposed by Gadegaard and Thuesen (2021). These improvements are in line 84 and 100 of the subsolv function where the MATLAB function spdiags has been replaced by elementwise multiplication. This improvement is mathematically consistent with the original formulation but brings a runtime improvement of approximately 10x for these lines. For the example discussed in Gadegaard and Thuesen (2021) this yields an overall reduction of the iteration time by 5 %.

The implementation of the SLP is the same as described in Section 5.1.1.

Since the MMA is known to be inefficient for problems containing many constraints the density constraints for each element given in Equation 5.1c are reformulated into a single constraint. This is done by approximating the maximum element density with a P-norm aggregate function using adaptive constraint scaling. This is done using Equation B.21.

$$g_1(\{x\}) = c_{dens} \left( \sum_{e=1}^{n_{elem}} \left( \sum_{c=1}^{n_{mat}} x_{ec} \right)^P \right)^{\frac{1}{P}} \tag{B.21}$$

### B.5.2 Results

The algorithms that will be investigated are the MMA and SLP using both a constraint on the density of each element and using a P-norm with constraint scaling to estimate the maximum total density. The method of moving asymptotes is very inefficient when a large number of constraints are added and the iteration time if the density constraints are added for each element is approximately 600 s per iteration during the first 10 iterations. Therefore this configuration will not be investigated further.

The final material distribution for the different optimization algorithms can be seen in Figure B.1. The different colors denote the different fiber angles while the transparency represents the density. The material distributions look similar which is expected.

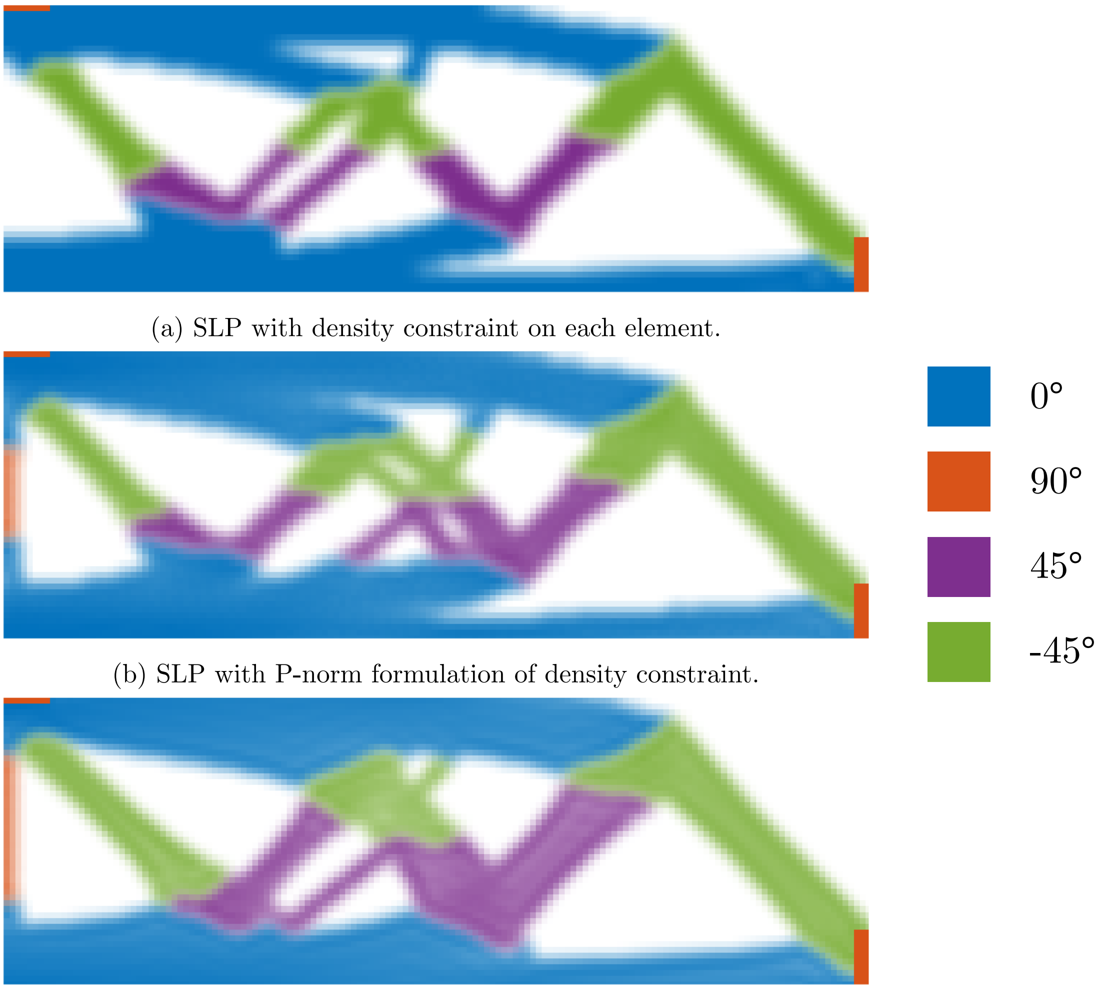


(a) SLP with density constraint on each element.

(b) SLP with P-norm formulation of density constraint.

(c) MMA with P-norm formulation of density constraint.

Figure B.1: Final material distribution from the different algorithms.

When the results in Figure B.2 are compared it is seen that the MMA and SLP with the P-norm formulation of the density constraint have a similar convergence history with the SLP being a bit better in all measures. It has a slightly lower compliance and measure of non-discreteness and the iteration time is also lower except for the first few iterations.
When the convergence are compared it is seen that the best solution is obtained by the SLP algorithm with the element wise formulation of the density constraint since it achieves the lowest compliance. This is also the solution with the lowest measure of non-discreteness, but it comes at the cost of notably higher iteration times. This although is not a big problem since it converges in fewer iterations as seen in both Figure B.2a and B.2c.

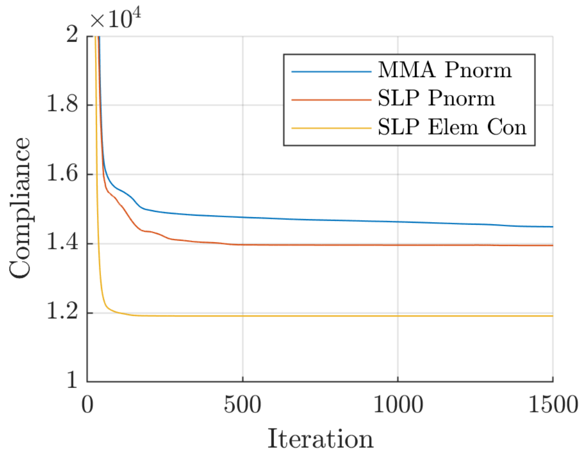


(a) Objective function.

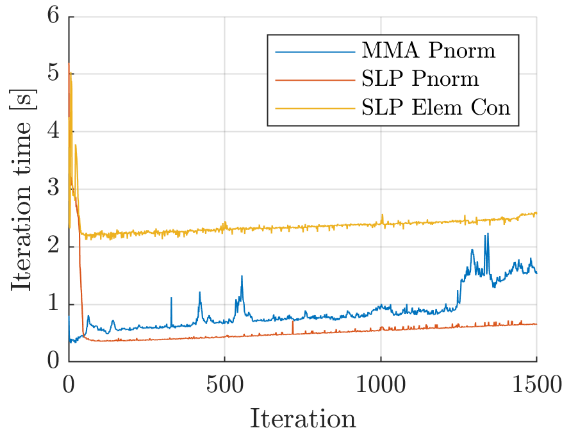


(b) Iteration time.

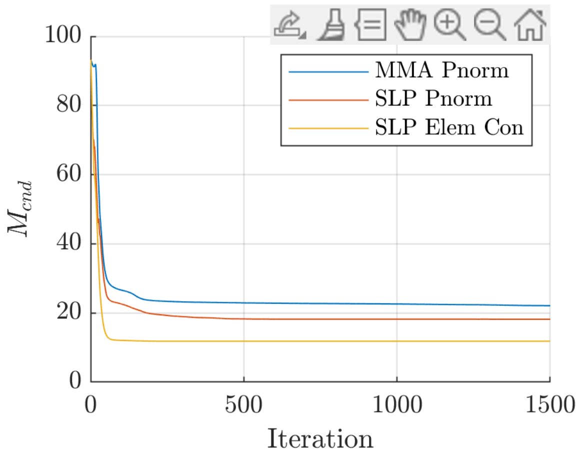


(c) Measure of candidate non-discreteness.

Figure B.2: Evolution of different properties during the optimization.

In addition to the above results it is worth noting that the MMA had a CPU utilization of around 60-65 % while the SLP had a CPU utilization of around 5-10 %. This is not a problem unless others are using the server simultaneous and it is furthermore assumed that the SLP can be speed up by using a personal PC which has a CPU with a faster single core performance.

Therefore it is decided to use the SLP algorithm since it is faster and gives better results. The density constraints will be formulated as a constraint for each element since this both gives a lower objective function and measure of non-discreteness. The time it takes to run the optimization might be higher due to the higher iteration time but a better solution is weighted higher than the runtime of the algorithm.

# C Continuation approach

In order to solve the problems stated in Section 5.1.3 it has been tried to use a continuation approach. This has been used to avoid reaching a poor local minima and is applied to the failure index relaxation and stiffness penalization factors $q$ and $p$ respectively.

Two different continuation approaches are applied to the benchmark problem in order to get a more discrete result. The first is a continuation approach on the stiffness penalisation factor $p$ where $p = 1.5 \rightarrow 4$ over 1000 iterations. A constant offset is applied to the failure index relaxation factor $q$, so $p - q = 0.5$. The result for this continuation approach can be seen in Figure C.1. The optimization converges to a volume fraction of 60.3% which is better then the benchmark without the continuation approach. The final measures of non-discreteness after 1500 iterations are $M_{cnd} = 30.56\%$ and $M_{dnd} = 56.69\%$, which is higher than the benchmark without continuation. The lower volume fraction will result in space for more intermediate densities, which will increase the measures of non-discreteness.

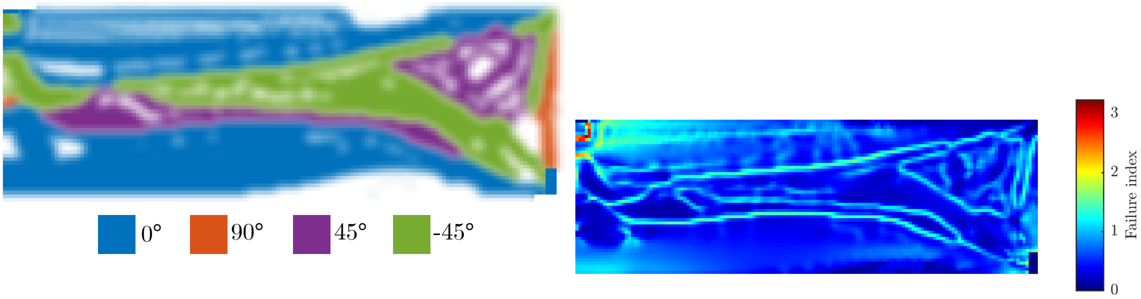


(a) Material distribution of the four fiber angles. (b) The failure index for the geometry.

Figure C.1: Benchmark problem with continuation approach with constant offset on $q$ and $p$.

The second continuation approach is applied on both the stiffness penalization $p$ and failure index relaxation $q$. The stiffness penalization is varied so $p = 1.5 \rightarrow 4$ and the failure index relaxation is varied so $q = 0.5 \rightarrow 3.75$ over the first 1000 iterations of the optimization. This will penalize the intermediate densities even more.
The results for the double continuation approach can be seen in Figure C.2. This has decreased the volume fraction to 53.2%, but increased the measure of non-discreteness. The measures of non-discreteness is $M_{cnd} = 35.24\%$ and $M_{dnd} = 65.28\%$ after 1500 iterations. The double continuation approach has therefore not yielded a better result regarding the discreteness. The failure index has also increased even more.

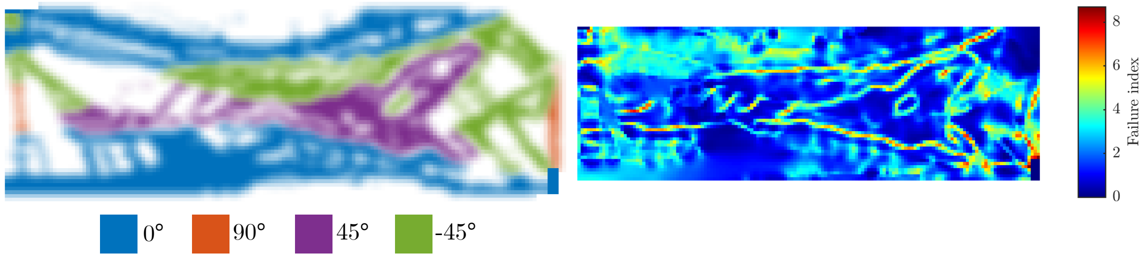


(a) Material distribution of the four fiber angles.

(b) The failure index for the geometry.

Figure C.2: Benchmark problem with continuation approach on both $q$ and $p$.

The general problem of the optimization not converging to a feasible and discrete result can not be solved by penalising the intermediate densities more. The effect of the increased penalization is even opposite as increased penalization also increases the maximum failure index and the measures of non discreteness. Other reasons for the infeasible non-discrete results therefore needs to be examined.

# D Element definition of quadratic Q9 element

During this appendix the definition of the strain displacement matrix and the shape functions will be introduced for the quadratic 9 node element.

## D.1 Shape functions

The shape functions for the quadratic Q9 element are given in Equation D.1.

$$N_9 = (1-\xi^2)(1-\eta^2) \tag{D.1a}$$

$$N_8 = \frac{1}{2}(1-\xi)(1-\eta^2) - \frac{1}{2}N_9 \tag{D.1b}$$

$$N_7 = \frac{1}{2}(1-\xi^2)(1+\eta) - \frac{1}{2}N_9 \tag{D.1c}$$

$$N_6 = \frac{1}{2}(1+\xi)(1-\eta^2) - \frac{1}{2}N_9 \tag{D.1d}$$

$$N_5 = \frac{1}{2}(1-\xi^2)(1-\eta) - \frac{1}{2}N_9 \tag{D.1e}$$

$$N_4 = \frac{1}{4}(1-\xi)(1+\eta) - \frac{1}{2}N_7 - \frac{1}{2}N_8 - \frac{1}{4}N_9 \tag{D.1f}$$

$$N_3 = \frac{1}{4}(1+\xi)(1+\eta) - \frac{1}{2}N_6 - \frac{1}{2}N_7 - \frac{1}{4}N_9 \tag{D.1g}$$

$$N_2 = \frac{1}{4}(1+\xi)(1-\eta) - \frac{1}{2}N_5 - \frac{1}{2}N_6 - \frac{1}{4}N_9 \tag{D.1h}$$

$$N_1 = \frac{1}{4}(1-\xi)(1-\eta) - \frac{1}{2}N_5 - \frac{1}{2}N_8 - \frac{1}{4}N_9 \tag{D.1i}$$

## D.2 Strain displacement matrix

The strain displacement matrix is calculated based on the derivatives of the shape functions given in Equation D.2.

$$\frac{\partial N_9}{\partial \eta} = -2\eta(-\xi^2 + 1) \tag{D.2a}$$

$$\frac{\partial N_9}{\partial \xi} = -2\xi(-\eta^2 + 1) \tag{D.2b}$$

$$\frac{\partial N_8}{\partial \eta} = -\eta(-\xi + 1) - \frac{1}{2}\frac{\partial N_9}{\partial \eta} \tag{D.2c}$$

$$\frac{\partial N_8}{\partial \xi} = -\frac{1}{2}(-\eta^2 + 1) - \frac{1}{2}\frac{\partial N_9}{\partial \xi} \tag{D.2d}$$

$$\frac{\partial N_7}{\partial \eta} = \frac{1}{2}(-\xi^2 + 1) - \frac{1}{2}\frac{\partial N_9}{\partial \eta} \tag{D.2e}$$

$$\frac{\partial N_7}{\partial \xi} = -\xi(\eta + 1) - \frac{1}{2}\frac{\partial N_9}{\partial \xi} \tag{D.2f}$$

$$\frac{\partial N_6}{\partial \eta} = -\eta(\xi + 1) - \frac{1}{2}\frac{\partial N_9}{\partial \eta} \tag{D.2g}$$

$$\frac{\partial N_6}{\partial \xi} = \frac{1}{2}(-\eta^2 + 1) - \frac{1}{2}\frac{\partial N_9}{\partial \xi} \tag{D.2h}$$

$$\frac{\partial N_5}{\partial \eta} = -\frac{1}{2}(-\xi^2 + 1) - \frac{1}{2}\frac{\partial N_9}{\partial \eta} \tag{D.2i}$$

$$\frac{\partial N_5}{\partial \xi} = -\xi(-\eta + 1) - \frac{1}{2}\frac{\partial N_9}{\partial \xi} \tag{D.2j}$$

$$\frac{\partial N_4}{\partial \eta} = -\frac{1}{4}(-\xi + 1) - \frac{1}{2}\frac{\partial N_7}{\partial \eta} - \frac{1}{2}\frac{\partial N_8}{\partial \eta} - \frac{1}{4}\frac{\partial N_9}{\partial \eta} \tag{D.2k}$$

$$\frac{\partial N_4}{\partial \xi} = -\frac{1}{4}(\eta + 1) - \frac{1}{2}\frac{\partial N_7}{\partial \xi} - \frac{1}{2}\frac{\partial N_8}{\partial \xi} - \frac{1}{2}\frac{\partial N_9}{\partial \xi} \tag{D.2l}$$

$$\frac{\partial N_3}{\partial \eta} = \frac{1}{4}(\xi + 1) - \frac{1}{2}\frac{\partial N_6}{\partial \eta} - \frac{1}{2}\frac{\partial N_7}{\partial \eta} - \frac{1}{4}\frac{\partial N_9}{\partial \eta} \tag{D.2m}$$

$$\frac{\partial N_3}{\partial \xi} = \frac{1}{4}(\eta + 1) - \frac{1}{2}\frac{\partial N_6}{\partial \xi} - \frac{1}{2}\frac{\partial N_7}{\partial \xi} - \frac{1}{2}\frac{\partial N_9}{\partial \xi} \tag{D.2n}$$

$$\frac{\partial N_2}{\partial \eta} = -\frac{1}{4}(\xi + 1) - \frac{1}{2}\frac{\partial N_5}{\partial \eta} - \frac{1}{2}\frac{\partial N_6}{\partial \eta} - \frac{1}{4}\frac{\partial N_9}{\partial \eta} \tag{D.2o}$$

$$\frac{\partial N_2}{\partial \xi} = \frac{1}{4}(-\eta + 1) - \frac{1}{2}\frac{\partial N_5}{\partial \xi} - \frac{1}{2}\frac{\partial N_6}{\partial \xi} - \frac{1}{2}\frac{\partial N_9}{\partial \xi} \tag{D.2p}$$

$$\frac{\partial N_1}{\partial \eta} = -\frac{1}{4}(-\xi + 1) - \frac{1}{2}\frac{\partial N_5}{\partial \eta} - \frac{1}{2}\frac{\partial N_8}{\partial \eta} - \frac{1}{4}\frac{\partial N_9}{\partial \eta} \tag{D.2q}$$

$$\frac{\partial N_1}{\partial \xi} = -\frac{1}{4}(-\eta + 1) - \frac{1}{2}\frac{\partial N_5}{\partial \xi} - \frac{1}{2}\frac{\partial N_8}{\partial \xi} - \frac{1}{2}\frac{\partial N_9}{\partial \xi} \tag{D.2r}$$

In order to determine the strain displacement matrix $[B]$ the derivatives of the shape functions with respect to $x$ and $y$ are needed. This can be determined using the chain rule as given in Equation D.3.

$$\begin{Bmatrix} \dfrac{\partial N_i}{\partial \xi} \\ \dfrac{\partial N_i}{\partial \eta} \end{Bmatrix} = \begin{bmatrix} \dfrac{\partial x}{\partial \xi} & \dfrac{\partial y}{\partial \xi} \\ \dfrac{\partial x}{\partial \eta} & \dfrac{\partial y}{\partial \eta} \end{bmatrix} \begin{Bmatrix} \dfrac{\partial N_i}{\partial x} \\ \dfrac{\partial N_i}{\partial y} \end{Bmatrix} \tag{D.3a}$$

$$\begin{Bmatrix} \dfrac{\partial N_i}{\partial x} \\ \dfrac{\partial N_i}{\partial y} \end{Bmatrix} = [J]^{-1} \begin{Bmatrix} \dfrac{\partial N_i}{\partial \xi} \\ \dfrac{\partial N_i}{\partial \eta} \end{Bmatrix} \tag{D.3b}$$

The jacobian $[J]$ can be determined by differentiating the relation between the local and global coordinates. This relation is given in Equation D.4 where $X_i$ and $Y_i$ are the global coordinates of node $i$ while $x$ and $y$ are the resulting coordinates corresponding to $\xi$ and $\eta$.

$$x = \sum_{i=1}^{9} N_i(\xi,\eta) X_i \tag{D.4a}$$

$$y = \sum_{i=1}^{9} N_i(\xi,\eta) Y_i \tag{D.4b}$$

The derivative of this relation is the jacobian $[J]$ and it can be calculated using Equation D.5.

$$\frac{\partial x}{\partial \xi} = \sum_{i=1}^{9} \frac{\partial N_i(\xi,\eta)}{\partial \xi} X_i \tag{D.5a}$$

$$\frac{\partial x}{\partial \eta} = \sum_{i=1}^{9} \frac{\partial N_i(\xi,\eta)}{\partial \eta} X_i \tag{D.5b}$$

$$\frac{\partial y}{\partial \xi} = \sum_{i=1}^{9} \frac{\partial N_i(\xi,\eta)}{\partial \xi} Y_i \tag{D.5c}$$

$$\frac{\partial y}{\partial \eta} = \sum_{i=1}^{9} \frac{\partial N_i(\xi,\eta)}{\partial \eta} Y_i \tag{D.5d}$$

The derivatives of the shape functions with respect to $x$ and $y$ can then be calculated using Equation D.3. The strain displacement matrix can thus be setup using Equation D.6.

$$[B] = \begin{bmatrix} \frac{\partial N_1}{\partial x} & 0 & \frac{\partial N_2}{\partial x} & 0 & ... & \frac{\partial N_9}{\partial x} & 0 \\ 0 & \frac{\partial N_1}{\partial y} & 0 & \frac{\partial N_2}{\partial y} & ... & 0 & \frac{\partial N_9}{\partial y} \\ \frac{\partial N_1}{\partial y} & \frac{\partial N_1}{\partial x} & \frac{\partial N_2}{\partial y} & \frac{\partial N_2}{\partial x} & ... & \frac{\partial N_9}{\partial y} & \frac{\partial N_9}{\partial x} \end{bmatrix} \tag{D.6}$$

# E Additional results from benchmark tests

## E.1 MBB SPA Q4

The failure indices in the individual materials are given in Figure E.1.

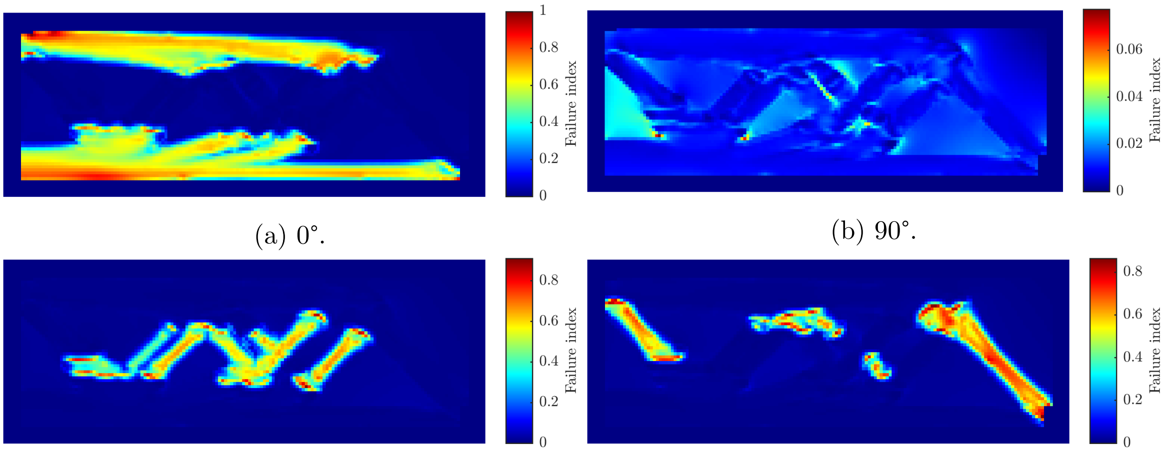


(a) 0°. (b) 90°.

(c) 45°. (d) −45°.

Figure E.1: Failure index in different materials.

The full convergence history is given in Figure E.2.

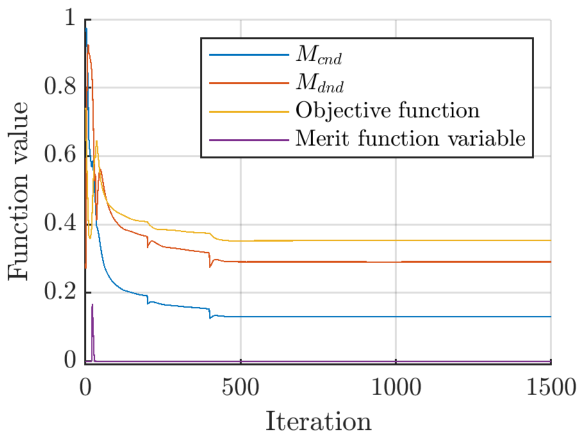


Figure E.2: Full convergence history.

## E.2 L-bracket SPA Q4

The failure indices in the individual materials are given in Figure E.3.

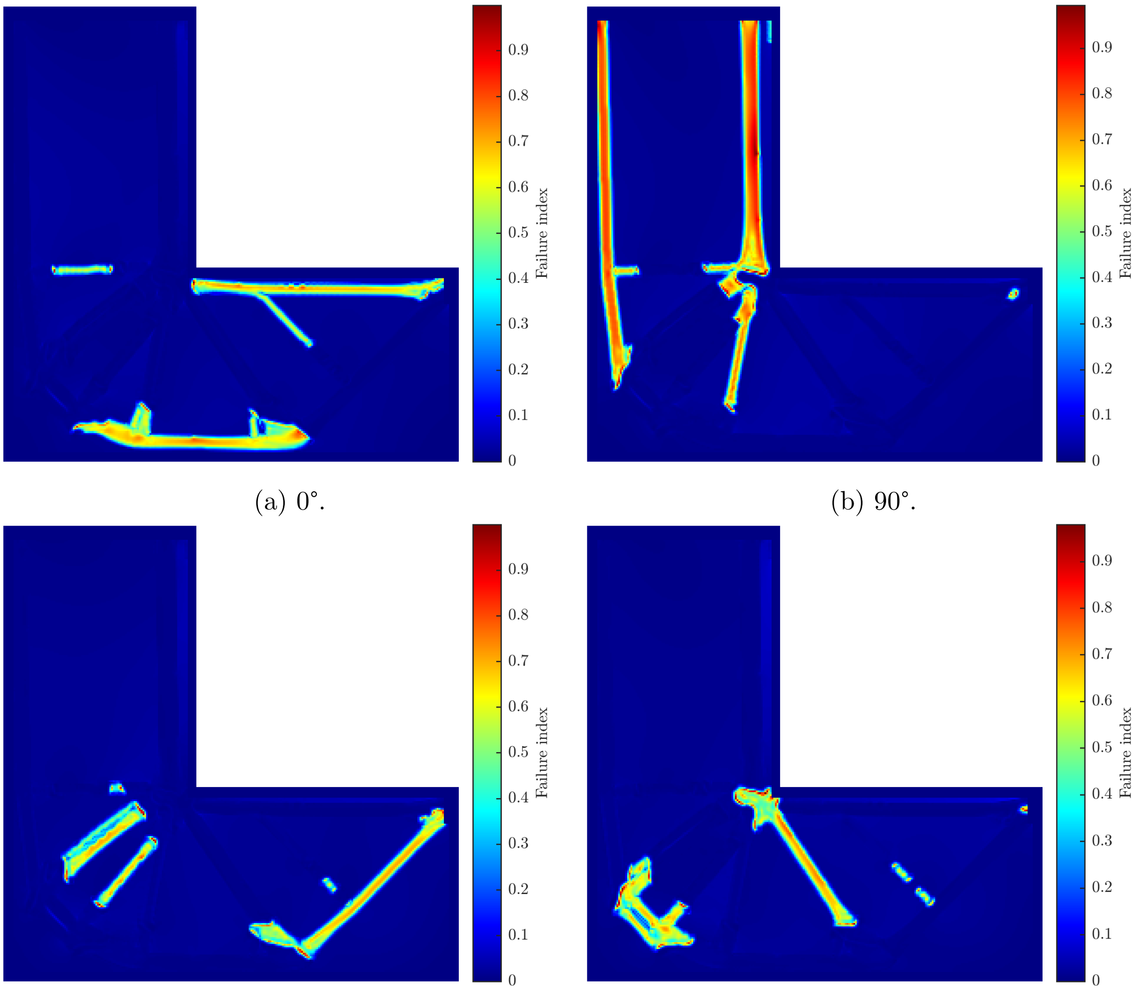


(a) 0°. (b) 90°.

(c) 45°. (d) −45°.

Figure E.3: Failure index in different materials.

The full convergence history is given in Figure E.4.

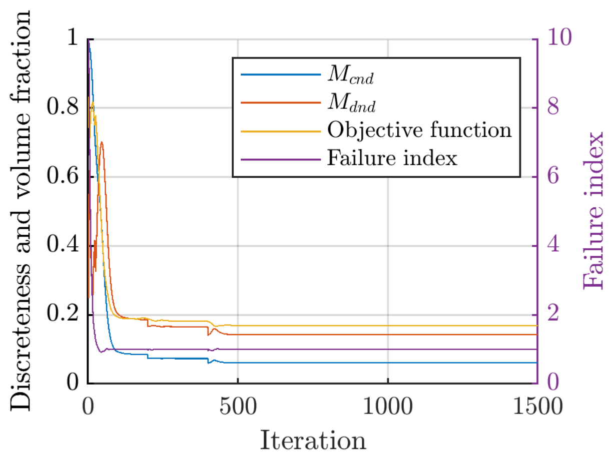


Figure E.4: Full convergence history.

## E.3 Q4 CCF L-bracket

The failure indices in the individual materials are given in Figure E.5.

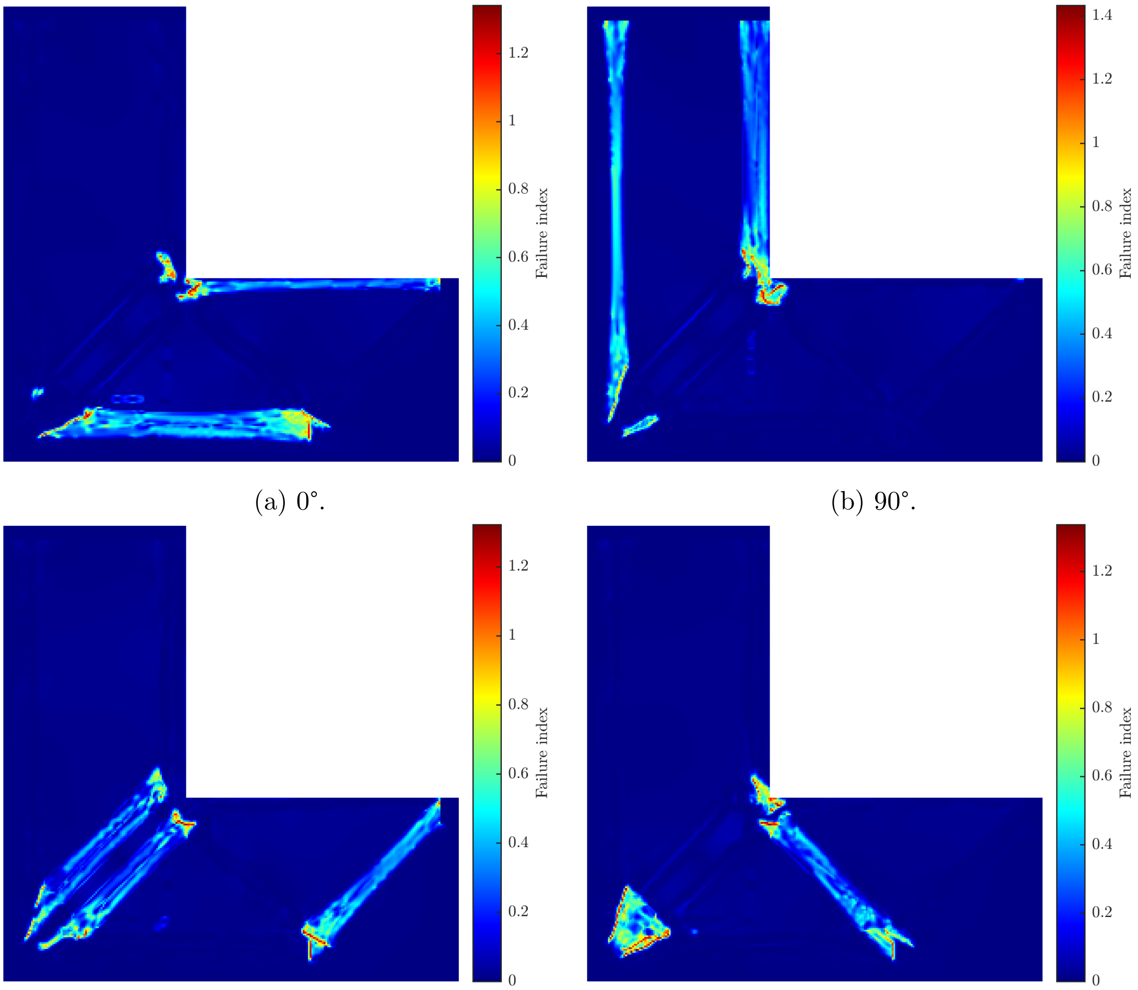


(a) 0°. (b) 90°.

(c) 45°. (d) −45°.

Figure E.5: Failure index in different materials.

The full convergence history is given in Figure E.6.

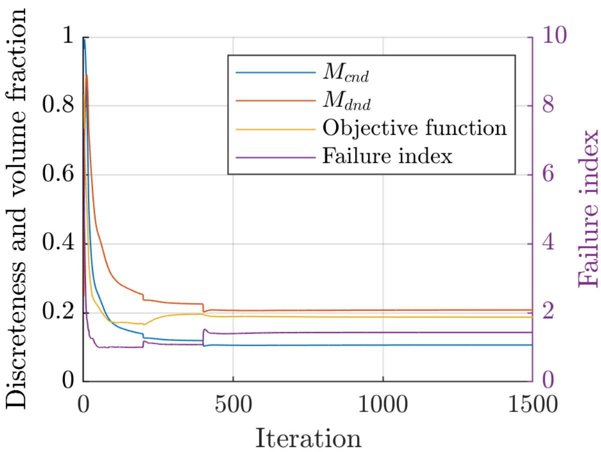


Figure E.6: Full convergence history.